



저작자표시-비영리-변경금지 2.0 대한민국

이용자는 아래의 조건을 따르는 경우에 한하여 자유롭게

- 이 저작물을 복제, 배포, 전송, 전시, 공연 및 방송할 수 있습니다.

다음과 같은 조건을 따라야 합니다:



저작자표시. 귀하는 원저작자를 표시하여야 합니다.



비영리. 귀하는 이 저작물을 영리 목적으로 이용할 수 없습니다.



변경금지. 귀하는 이 저작물을 개작, 변형 또는 가공할 수 없습니다.

- 귀하는, 이 저작물의 재이용이나 배포의 경우, 이 저작물에 적용된 이용허락조건을 명확하게 나타내어야 합니다.
- 저작권자로부터 별도의 허가를 받으면 이러한 조건들은 적용되지 않습니다.

저작권법에 따른 이용자의 권리는 위의 내용에 의하여 영향을 받지 않습니다.

이것은 [이용허락규약\(Legal Code\)](#)을 이해하기 쉽게 요약한 것입니다.

[Disclaimer](#)

Doctoral Thesis

Growth of Single-Crystalline and Layer-Controllable
Hexagonal Boron Nitride

Kyung Yeol Ma

School of Energy and Chemical Engineering
(Energy Engineering)

Ulsan National Institute of Science and Technology

2021

Growth of Single-Crystalline and Layer-Controllable Hexagonal Boron Nitride

Kyung Yeol Ma

School of Energy and Chemical Engineering
(Energy Engineering)

Ulsan National Institute of Science and Technology

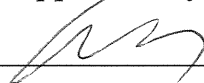
Growth of Single-Crystalline and Layer-Controllable Hexagonal Boron Nitride

A thesis/dissertation submitted to
Ulsan National Institute of Science and Technology
in partial fulfillment of the
requirements for the degree of
Doctor of Philosophy

Kyung Yeol Ma

12/17/2020

Approved by



Advisor


Hyeon Suk Shin

Growth of Single-Crystalline and Layer-Controllable Hexagonal Boron Nitride

Kyung Yeol Ma

This certifies that the thesis/dissertation of Kyung Yeol Ma is approved.

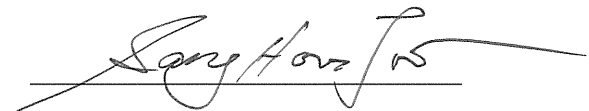
12/17/2020



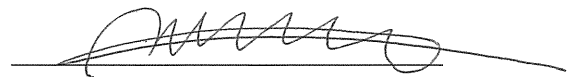
Advisor: Hyeon Suk Shin



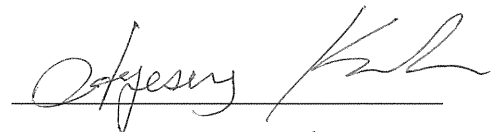
Ji-Hyun Jang



Sang Hoon Joo



Hu Young Jeong



Hyesung Park

Abstract

Two-dimensional (2D) materials provide great potential for their applications in electronics and photonics because they can offer opportunity for extending Moore's law in beyond-CMOS (complementary metal-oxide-semiconductor) devices. Among 2D materials, hexagonal boron nitride (hBN) is a representative 2D insulating material with bandgap (~6 eV). Owing to atomically flat surface without dangling bonds yet with excellent thermal and chemical stabilities, hBN has been introduced as a promising material for an excellent dielectric layer to efficiently reduce charge scattering and a screening layer from surroundings. A key technological challenge is the scalable manufacture of single-crystal 2D hBN film to avoid a lack of durability and a poor performance influenced by inhomogeneities and grain boundaries. In addition, the controllability of the number of layers is also highly required due to the electron tunneling properties depending on the thickness of hBN. Even though several approaches to achieve large-scale single-crystal hBN and control the number of layers have been demonstrated, a growth method for few-layer single-crystalline hBN and precise control of the number of layers is still unknown. In this thesis, I demonstrate an approach to grow large-scale single-crystal hBN by chemical vapor deposition (CVD) method. First, I show the epitaxial growth of single-crystal trilayer hBN on Ni (111) foil of 2 x 5 cm at 100 °C higher temperature than normal growth temperature for Ni substrate. The trilayer hBN grains show unidirectional alignment and seamless stitching to form single-crystal film on Ni₂₃B₆/Ni (111) where a Ni₂₃B₆ layer is formed between hBN and Ni (111) during cooling. Microscopic investigations reveal epitaxial relationship between hBN, Ni₂₃B₆, and Ni (111) and enable to understand the hBN growth mechanism, the surface-mediated growth. Furthermore, single-crystal trilayer hBN on Ni₂₃B₆/Ni (111) plays a role of a catalytic-transparent protection layer for enhanced long-term stability of hydrogen evolution reaction catalyst and a dielectric layer to prevent electron doping from SiO₂ substrate in MoS₂ transistors. Our results suggest that few-layer single-crystal hBN allows wide applications for 2D devices and catalytic-transparent protection layer of (electro)catalysts. Next, I demonstrate a method for controlling the number of layers of 2-inch wafer-scale single-crystal hBN film on sapphire substrate by remote inductively coupled plasma CVD, which is a temperature-dependent growth method for mono-, bi-, and trilayer hBN. The x-ray photoelectron spectroscopic and transmission electron microscopic investigations show the formation of a Al-N buffer layer between sapphire substrate and the first layer and the reduction of the interlayer spacing of hBN by the Al-N bond. However, the transferred hBN onto SiO₂/Si substrate shows a typical interlayer spacing of hBN. This work takes a step towards the layer-controlled growth of wafer-scale uniform hBN films.

Contents

Abstract

Contents

List of Figures

List of Tables

Chapter 1: Research Background for the Two-Dimensional (2D) Hexagonal Boron Nitride (hBN)	1
.....	1
1.1 Overview	1
1.2 Top-down approaches for the preparation	3
1.3 Bottom-up approaches using the chemical vapor deposition (CVD)	6
1.3.1 Growth mechanism of hBN: surface diffusion, precipitation, and epitaxy	8
1.3.2 Toward single-crystal growth of monolayer hBN on metal catalysts	8
1.3.3 Control of the number of hBN layers	15
1.3.4 Direct growth of hBN on dielectrics	17
1.4 Properties and applications of hBN	19
1.4.1 Growth platform for graphene and transition metal dichalcogenides	19
1.4.2 Dielectrics for the 2D integrated electronics	22
1.4.3 Protection layer of 2D materials from surrounding	24
1.4.4 Sieving membrane for proton and molecules	24
1.5 Outlook of hBN	28
1.6 Reference	29
Chapter 2: Epitaxial Growth of Single-Crystal Few-Layer Hexagonal Boron Nitride on Ni (111)	35
.....	35
2.1 Abstract	35

2.2 Introduction	35
2.3 Experimental section	37
2.3.1 Preparation of single-crystal Ni (111) foil.....	37
2.3.2 Growth of single-crystal trilayer hBN on Ni (111).....	37
2.3.3 Transfer of hBN film onto arbitrary substrates.....	37
2.3.4 Characterizations	40
2.3.5 H ₂ plasma etching	40
2.3.6 Electrochemical measurements	40
2.3.7 DFT calculation	41
2.4 Results and discussion	41
2.4.1 Growth procedure and mechanism of trilayer hBN on Ni (111)	41
2.4.2 Structure characterizations of hBN/Ni ₂₃ B ₆ /Ni (111)	55
2.4.3 DFT calculation for the binding energies of hBN with Ni (111).....	61
2.4.4 Applications of CVD-grown single-crystal trilayer hBN	63
2.5 Conclusion	70
2.6 Reference	71
Chapter 3: Layer-Controlled Single-Crystal Hexagonal Boron Nitride Film with AA'-Stacking Order by Buffer Layer Formation	75
3.1 Abstract	75
3.2 Introduction	75
3.3 Experimental section	76
3.3.1 Layer-controllable growth of hBN on 2-inch sapphire.....	76
3.3.2 Transfer of hBN films onto other substrate	77
3.3.3 Porous support casting for gas transport measurements	77
3.3.4 Characterizations	77
3.4 Results and discussion	80

3.4.1 Layer-controllable multilayer hBN on sapphire	80
3.4.2 Temperature-dependend growth mechanism.....	91
3.4.3 Membrane application for molecular transport	104
3.5 Conclusion	109
3.6 Reference	110

List of Figures

[Chapter 1]

Figure 1. Atomic structure and properties of hexagonal boron nitride.

Figure 2. (a) Optical (left) and AFM (right) images of mechanically exfoliated hBN nanosheets on SiO₂/Si substrate. The dashed line indicates the height profile (inset) of exfoliated flake. (b) Low magnification TEM image of (a). (c) High-magnified images at red arrow in (b), showing the number of layers. The thinnest area is shown in inset of (c)¹⁶. (d-f) Wavelength dependency of optical contrast for monolayer and bilayer hBN on SiO₂ (90 nm)/Si substrate¹⁷.

Figure 3. Schematic illustrations of the liquid exfoliation method of (a) ion intercalation, (b) ion exchange, and (c) sonication -assisted exfoliation. In the ion intercalation method, intercalated ions (yellow circles) separate the hBN layers. The ion exchange method uses substitution process of originally contained ion to larger ions. The sonication-assisted method should utilize the stable solvents to avoid reaggregation and sedimentation¹⁹. (d) Photographs of dispersed BN solution in various EtOH/H₂O ratio of mixture. (e) The absorbance of BN solutions at different EtOH/H₂O mixtures²².

Figure 4. Schematics of representative CVD method for hBN growth. (a) typical thermal CVD¹¹, (b) plasma-enhanced CVD²⁹.

Figure 5. (a) Schematic illustration of surface-diffusion mediated mechanism of hBN growth on Cu surface³⁰. (b) Schematic demonstration of epitaxial relationship of hBN with Al₂O₃³¹. (c) Schematically described growth mechanism of hBN on the Fe catalyst with H₂ atmosphere³². (d) Schematic illustration of the CVD growth step of multilayer hBN on Ni-Fe alloy catalyst³³.

Figure 6. (a) Schematic illustration of hBN growth method using LPCVD setup. (b) Thermal decomposition of ammonia borane, solid precursor, to H₂, borazine, and aminoborane at 60~180 °C. SEM images resulting from (c) 60 and (d) 90 °C of heating belt temperature, T1 in (a). (e) Schematic diagram of atomic termination of hBN flake. (f) Continuous hBN film transferred on SiO₂/Si substrate³⁴. (g) Schematic description of electrochemical H₂ bubbling transfer method. (h) Raman spectrum of monolayer hBN on SiO₂/Si. (i) High-resolution TEM image of freestanding monolayer hBN on quantifoil. The inset indicates the electron diffraction pattern of hexagonal structure of hBN²⁷.

Figure 7. (a) Schematic procedure of the hBN growth on a Cu-Ni alloy. SEM images of hBN grains grown on a pure Cu (b) and Cu-Ni alloy with (c) 10 %, (d) 20 %, and (e) 30 % Ni concentrations³⁵. (f)

Scheme of a Fe/SiO₂/Si catalyst system³⁶. (g) SEM image of the largest hBN flake grown on a Fe/SiO₂ (300 nm)/Si substrate. A corresponding low-magnification SEM image was displayed in inset in (g). (h) Continuous hBN on a Fe surface. Black arrows in inset of (h) shows grain boundaries. (i) Schematic illustration of the proposed growth mechanism. (1) The Si atoms diffuse into the upper Fe by thermal annealing. (2) The dehydrogenation and dissociation of borazine occur when borazine precursor reach to the Fe surface. (3) B and N atoms dissolve in Fe surface. (4) After saturation, nucleation and growth are observed on the Fe surface. (5) Escape of some N species occur from the Fe surface into the N₂ phase.

Figure 8. (a) Schematic procedure of the large-scale single-crystal hBN growth from self-collimated circular hBN grains with rotation induced by the attractive Coulomb interactions of B and N edges between grains (i-vi). (b) Photograph of 3 x 3 cm² single-crystal hBN film on SiO₂/Si wafer. (c) SEM images of time-dependent hBN growth from nuclei to uniform film. (d) Photograph of a 10 x 10 cm² single-crystal Cu (110) fabricated by thermal annealing. (e) SEM image of unidirectional alignment of hBN grains on the Cu (110) surface. (f) LEED pattern of hBN grain. Based on triple symmetry, three dots marked by orange circle show stronger intensity than the other three dots marked by green circle. (g) SEM image of single-crystal hBN after H₂ etching process at 1000 °C. (h) Schematics of the configuration between the hBN lattice and the atomic step of Cu (110). (i) First-principles DFT calculations for the formation energies of hBN edges bonded with Cu <211> step edge. (j) Optical image of a Cu (111) thin film. (k) single orientation of hBN grains on Cu (111). (l) DFT calculation of the lowest-energy structure of the N₁B_{II}-Cu (111).

Figure 9. (a) Optical and (b) SEM images of large-area hBN film. Inset in (b) shows HRTEM image of the film edge showing bilayer hBN²⁸. (c) TEM images for hBN growth as a function of different growth time (1, 5, 15, and 30 min). (d) B 1s XPS spectrum of sequential growth with diborane first. (e) Sequential growth with ammonia first²⁴. (f) schematics of the CVD method for multilayer hBN growth on Fe foil using borazine. Right panels are showing photographs of as-grown hBN/Fe foil and as-transferred hBN/SiO₂/Si. (g) SEM image of a hBN film on Fe foil. (h) Average thickness of slow and fast cooling. (i) cross-sectional TEM and (j) High-angle annular dark-field scanning transmission electron microscopy (HAADF STEM) image of multilayer hBN film²⁶.

Figure 10. (a) Raman spectrum of hBN grown on Al₂O₃, indicating E_{2g} phonon mode of hBN. (b) Cross-section TEM image of hBN on Al₂O₃⁴⁵. (c) Proposed growth mechanism of the oxygen-assisted, transfer-free CVD growth of hBN. (d) XPS spectra for B 1s and N 1s. The B-O peak in B 1s spectrum shows the presence of B-terminated edges bonded with SiO₂/Si⁴⁶. (e) A photograph of 2-inch wafer-

scale hBN grown on Al_2O_3 . The inset shows highly smooth surface. (f) The histogram of distribution for surface roughness. (g) Cross-section TEM image of epitaxially grown multilayer hBN parallel to Al_2O_3 (11-20). (h) LEED pattern is indicating that the superstructure of single-orientation hBN film on Al_2O_3 with small strain effect of 2.6%³¹. (i) Schematic illustrations of multilayer hBN grown on Al_2O_3 by using $\text{Fe}_{82}\text{B}_{18}$ alloy and N_2 gas for B and N precursors, respectively. (j-m) Optical images of hBN grown on Al_2O_3 with (j) 60, (k) 120, (l) 180, and (m) 240 min at 1250 °C. Insets show corresponding AFM height profiles at the edge of film. (n) The thickness of multilayer hBN grown at various growth temperatures and times. (o) Raman spectra of as-prepared multilayer hBN films⁴⁷.

Figure 11. (a) Schematics of the temperature-triggered switching method for in-plane and vertical graphene/hBN heterostructures. (b, d) SEM and AFM images of in-plane graphene/hBN heterostructure and (c, e) vertical graphene/hBN heterostructure, respectively. (f-g) Continuous graphene/hBN heterostructure film and its optical image on SiO_2/Si after transferring process⁴⁸. (h) Schematic demonstration of CVD-derived patterned graphene/hBN stack on Cu foil. A pre-deposited PMMA seeds lead to form vertical graphene/hBN heterostructure grain and continuous film. (i) SEM images of PMMA-seed arrays on Cu surface by electron beam lithography, patterned graphene grain from PMMA, continuous graphene/hBN heterostructure film, and arranged graphene/hBN heterostructure⁴⁹.

Figure 12. (a) Schematic description of preparation of TMDs/hBN vertical heterostructure. Continuous hBN film is obtained on Ni-Ga alloy in CVD system. MoS_2 growth on hBN is conducted by introducing H_2S gas on hBN. (b) SEM image of the directly grown MoS_2 flakes on hBN. (c) TEM image of MoS_2/hBN vertical heterostructure. SAED pattern shows (110) plane of MoS_2 and (101-0) plane of hBN in the inset. (d) Raman spectra measured on $\text{MoS}_2/\text{SiO}_2$, transferred MoS_2 , and MoS_2/hBN . (e) XPS spectra of Mo 3d and S 2p of as-grown MoS_2 ⁵⁰. (f) Scheme of epitaxial graphene growth on single-crystal hBN film. (g) SEM image of as-grown graphene grains showing single-grain orientation and (h) continuous single-crystal graphene film. (i) Raman spectra of graphene/hBN heterostructure. (j) SAED pattern stacked by eight SAED patterns measured on different area of graphene/hBN heterostructure. (k) Experimental and (l) simulated moire pattern between graphene and hBN single crystal. (m) SEM image of triangle WS_2 grains and (inset) continuous film on single-crystal hBN film. LEED pattern indicates (11-20) and (10-10) planes of monolayer WS_2 ¹⁵.

Figure 13. (a) SEM image of the graphene/hBN vertical heterostructure. (b) Optical image of graphene back-gate FET device fabricated on 300 nm SiO_2/Si . (c) Device performance showing the drain current (I_{ds})-gate voltage (V_{G}) and resistance (R)- V_{G} curves⁴⁸. (d) Schematic illustration of graphene FET device on multilayer hBN. The inset displays optical image of a as-fabricated device. (e) Conductance

(σ) of graphene as a function of back gate voltage (V_{BG}). The blue and red curves indicate measurements on SiO_2 and hBN/SiO_2 , respectively. (f) Hole mobility (μ_p) plots vs n_{dirac} at different dielectrics of SiO_2 and hBN ²⁶.

Figure 14. (a) SEM image of locally covered single-crystal hBN layer on Cu foil. Inset shows the corresponding photograph. (b) Optical image and corresponding XPS mapping of Cu foil covered with hBN and without hBN. (d) XPS Cu 2p spectrum after oxidizing Cu foil measured on hBN covered area in (c)¹⁵. (e) Schematic illustration for the WVTR measuring system. (f) Measured WVTR results of polycrystal and single-crystal monolayer hBN compare to bare PET. (h) Schematic illustration of laser irradiation process on monolayer TMDs passivated by trilayer hBN film. (i) Changes in areal intensity of PL peak for WSe_2 , monolayer hBN/WSe_2 , and trilayer hBN/WSe_2 in the presence of a water droplet¹³.

Figure 15. (a) Schematic illustration of PEMFC system consisted by AA'-stacked trilayer hBN for proton exchange membranes. Right figures illustrate behaviors of proton and hydrogen gas through monolayer, turbostratic trilayer, and AA'-stacked trilayer hBN. (b) Polarization curves of various fuel cells using hBN layers (1L, AA'-3L, and turbostratic-3L) and Nafion 211. (c) OCV over time in fuel cells using AA'-stacked trilayer, monolayer hBN, and Nafion 211 under harsh working conditions. (d) Cell power densities of fuel cells initial and after 100 hours operating under harsh conditions.

[Chapter 2]

Figure 1. Electron backscatter diffraction (EBSD) IPF mapping of Ni (111) surface.

Figure 2. (a) Schematic diagrams of high-temperature and low-pressure CVD for the growth of hBN. (b) Photograph of a centimeter-sized as-grown single-crystal trilayer hBN film on Ni (111).

Figure 3. Schematic illustration of procedure of hBN growth on Ni(111).

Figure 4. Growth of single-crystal trilayer hBN on Ni (111). (a) SEM images showing the time evolution of trilayer hBN on a Ni (111) at 1220 °C. (Inset of step ii) The high-magnification SEM image of a hBN grain, showing that one edge of the hBN grain is parallel to the surface steps. (b) OM and (c) AFM images of an edge hBN film transferred on the SiO_2/Si . The inset of (c) shows the corresponding AFM height profile of a trilayer hBN film. (d) Raman spectrum of a trilayer hBN film on SiO_2/Si , showing the characteristic hBN signal at 1370 cm^{-1} . (e) UV-Vis absorption spectrum of trilayer hBN transferred to quartz substrate. The inset is optical bandgap analysis of (e).

Figure 5. Large-area SEM images of as-grown unidirectionally aligned hBN grains on Ni (111) substrate after growth for 30 min.

Figure 6. AFM images at the growth time for (a) 30 and (b) 45 min. The insets in (a) and (b) show height measurements taken at the position of the white lines.

Figure 7 (a-d) XPS spectra measured from an as-grown trilayer hBN film on Ni (111). The binding energies of the B 1s orbital at 190.2 eV and 189.9 eV confirm the formations of hBN (with N 1s at 379.9 eV) and Ni-B.

Figure 8. Schematic illustration of the growth procedure for hBN growth on Ni (111).

Figure 9. AFM images of cooling rates of (a) -30 and (b) -5 °C /min from 1220 to 620 °C hBN cooling rates of, respectively.

Figure 10. Energy filtered TEM (EF-TEM) mapping of hBN/Ni₂₃B₆/Ni. (a) Cross-sectional HR-TEM image (left upper) and EF-TEM maps of boron (red), nitrogen (green), and nickel (blue). (b) An image of overlaid EF-TEM maps for all elements.

Figure 11. The effect of cooling rate. Cross-sectional TEM images of as-formed Ni₂₃B₆ alloy for the cooling rates of (a) -60, (b) -30, and (c) -5 °C/min from 1220 to 620 °C, respectively. (d) Proposed mechanism for escape of B atoms during cooling.

Figure 12. Initial stage of hBN/Ni₂₃B₆ on Ni(111). (a-c) schematic diagrams (upper panels) and cross-sectional TEM images (lower panels) at the different growth time for (a) 30, (b) 45, and (c) 60 min at 1220 °C. (d) Cross-section TEM image of Ni surface after growth for 30 min. (e-f) AFM images at the growth time for (e) 30 and (f) 45 min. The insets in (e and f) show height measurements taken at the position of the white lines.

Figure 13. SEM images of hBN grown on Ni (111) for 30 min at (a) 1020 °C, (b) 1120°C, (c) 1170 °C, (d) 1220 °C, (e) 1270, and (f) 1320 °C. The inset of (a) reveals SAED pattern of hBN film grown at 1020 °C.

Figure 14. Epitaxial growth of hBN/Ni₂₃B₆ on Ni(111). (a-b) TEM images of Ni₂₃B₆/Ni interfaces and (c) STEM image of Ni₂₃B₆ at [110] zone axis. (d) simulated atomic structure of Ni₂₃B₆. (e) SAED pattern of Ni₂₃B₆ and Ni. (f) Low- and (g) High-magnification TEM image of trilayer hBN on Ni₂₃B₆. The corresponding FFT patterns of (h) hBN and (i) Ni₂₃B₆ from yellow squares in (g).

Figure 15. SEM image of trilayer hBN film on 5-nm-thick amorphous SiN windows.

Figure 16. SAED pattern images from nine regions (i—ix) in Figure 15. The relative orientation angle (θ) of six-symmetrical hexagonal dots is $36.52^\circ \pm 0.24^\circ$, indicating that all the hexagonal lattices are aligned along one specific direction.

Figure 17. Schematic of LC (5CB) alignment on hBN and POM images of LC-coated hBN film as a function of the polarized light angles: 0, 30, 60, 90, and 180°.

Figure 18. POM images of LC-coated polycrystal hBN film as a function of the polarized light angles: 0, 30, 60, 90, and 180°.

Figure 19. DFT calculations of the formation energies. (a) Schematic diagrams of the configuration of the hBN lattice and the surface of Ni (111) at top and side views, obtained from the TEM results in Figure 14g-i. (b) Binding energy calculation at various rotation angles between zigzag direction of N-terminated hBN and the Ni $\langle 110 \rangle$ direction. Black-, red-, and blue curves indicate mono-, bi-, and trilayer hBN.

Figure 20. Comparison for HER catalytic performances between $\text{Ni}_{23}\text{B}_6/\text{Ni}$ and $\text{hBN}/\text{Ni}_{23}\text{B}_6/\text{Ni}$ electrodes (a) Schematic illustration of HER on $\text{hBN}/\text{Ni}_{23}\text{B}_6$ electrode. (b) Polarization curves and (c) Tafel slopes for $\text{hBN}/\text{Ni}_{23}\text{B}_6$, Ni_{23}B_6 , Ni and Pt foil measured in 0.5 M H_2SO_4 with a scan rate of 5 mV s^{-1} . (d) The electrochemical stability test of Ni_{23}B_6 with and without hBN. Polarization curves of (e) $\text{hBN}/\text{Ni}_{23}\text{B}_6$ (f) Ni_{23}B_6 before (black curve) and after (red) 2,000 cycles, respectively. .

Figure 21. (a) Cross-sectional TEM image and XPS spectra of Ni_{23}B_6 without hBN protecting layer, after exposure to 50 W of H_2 plasma treatment for 5 min. (b) B 1s, (c) N 1s, and (d) Ni 2p spectra. The broad peak at 191.1 eV is estimated to be residual BN in B 1s spectrum.

Figure 22. FET built with hBN as a dielectric. (a) AFM and KPFM results of MoS_2 on SiO_2 and hBN/SiO_2 . The lower work function of MoS_2 on SiO_2 is due to strong electron doping from substrate (fermi level more close to conduction band). The fermi level position of MoS_2 on hBN/SiO_2 is close to the middle of the bandgap of MoS_2 , indicates hBN preserves the intrinsic electrical property of MoS_2 . (b) Energy band diagram of intrinsic MoS_2 , $\text{MoS}_2/\text{SiO}_2$, and $\text{MoS}_2/\text{hBN}/\text{SiO}_2$. (c) Drain current versus gate voltage curve of typical MoS_2 FET on SiO_2 and hBN/SiO_2 . The extracted mobility at room temperature is 56 cm^2/Vs for SiO_2 and 90 cm^2/Vs for hBN/SiO_2 , respectively. The threshold voltage right shifted with hBN covering the SiO_2 , preventing strong electron doping from the substrates. The inset shows FET device structure with hBN.

[Chapter 3]

Figure 1. (a) Schematic illustrations of remote ICP-CVD with liquid borazine precursor.

Figure 2. Annealing protocol for the growth of hBN. The growth temperatures employed to obtain mono-, bi-, and trilayer hBN were 1020, 1120, and 1220 °C, respectively.

Figure 3. Wafer-scale growth of mono-, bi-, trilayer hBN films using remote ICP-CVD. (a) Schematic description of temperature-depended layer-controlled growth. AFM images of (b) mono-, (c) bi-, (d) trilayer hBN are indicating the uniform continuous film at the edge of film. The yellow solid lines show the (inset) height profile of each films. (e) Relationship between growth temperature and the number of hBN layers. (f) A representative photograph of as-grown uniform 2-inch trilayer hBN film on sapphire. (g) As transferred trilayer hBN onto SiO₂/Si substrate.

Figure 4. AFM images of as-transferred (a) mono-, (b) bi-, and (c) trilayer hBN films on SiO₂/Si.

Figure 5. AFM images of as-grown hBN on sapphire. (a) A surface of sapphire wafer shows highly smooth with extremely low RMS value of 0.112 nm. Surfaces of (b) mono-, (c) bi-, and (d) trilayer hBN on sapphire are showing comparable surface roughness to bare sapphire.

Figure 6. (a) UV absorption spectrum and corresponding (b) AFM image on sapphire after hBN growth at 1320 °C. Note that the considerable increase of RMS value is observed by comparison with a bare sapphire.

Figure 7. (a) UV absorption spectra of as-grown mono-, bi-, tri-layer hBN films on sapphire. (b) Corresponding Raman spectra of hBN films with different number of layers measured on (b) sapphire and (c) SiO₂/Si substrates.

Figure 8. (a, b) UV absorption spectra of hBN/sapphire after growth for 90 and 120 min at 1220 °C, respectively. (c, d) Corresponding AFM images of (a) and (b).

Figure 9. (a) High-resolution TEM image of trilayer hBN film on quantifoil TEM grid. The inset shows fast Fourier transform of the whole image. The d-spacing of (1 $\bar{1}$ 00) plane of hBN is 0.217 nm. (b) SEM image of trilayer hBN film transferred onto non-porous 5 nm-SiN thin film grid divided into nine regions. (c) SAED pattern images of seven segments from regions i to vii in (b). The relative rotation angle of hBN (1 $\bar{1}$ 00) plane to the horizontal direction is $86.33 \pm 0.27^\circ$ for region i to vii.

Figure 10. (a) Schematic illustration of liquid crystal (5CB) alignment on two types of hBN film transferred into SiO₂/Si. (b) Optical microscopic (OM) and (c-f) polarized optical microscopic (POM) images as a function of the polarized light angles: 0, 30, 60° of liquid crystal-coated trilayer hBN film.

Figure 11. (a) UV absorption spectra of hBN/sapphire as a function of plasma power in the optimized growth condition for 30 min at 1220 °C. The corresponding AFM images of (b) 10, (c) 30, (d) 50, (e) 80, and (f) 100 W display the change of hBN surface with increasing plasma power.

Figure 12. (a-c) AFM images of the surface on sapphire of hBN of sapphire at 1020, 1120, and 1220°C. (d) Corresponding UV absorption spectra.

Figure 13. (a) UV absorption and (b) Raman spectra of multilayer hBN grown at 1320 °C without plasma generation. (c) Corresponding XPS spectra of multilayer hBN on sapphire. AFM images display surface of (d) before and (e and f) after transfer multilayer hBN film. Inset of (f) presents height profile of yellow line near the edge of multilayer hBN film.

Figure 14. TEM analysis of multilayer hBN grown at 1320 °C without plasma generation. (a) low-magnified cross-section view for EELS line profile near the surface region of sapphire. (b and c) Corresponding EELS spectra of (a). (d) A STEM image of multilayer hBN/AlN buffer layer on sapphire. (e) A FFT pattern of multilayer hBN on AlN buffer layer, indicating epitaxial relationship. (f) Atomic-resolution TEM image of multilayer hBN and AlN buffer layer on sapphire. Intensity profile of the interlayer *d*-spacing of (g) hBN and (h) AlN along red and blue arrows in (f).

Figure 15. (a) Optical microscopic (OM) and (b-d) polarized optical microscopic (POM) images as a function of the polarized light angles: 0, 30, 60° of liquid crystal-coated multilayer hBN film grown at 1320 °C without plasma generation.

Figure 16. TEM analysis of tri- and bilayer hBN grown at 1220 and 1120 °C with plasma generation on sapphire, respectively. Atomic-resolution cross-sectional TEM images of (a) trilayer and (b) bilayer hBN display zigzag edge of hBN (inset of a) parallel to sapphire ($11\bar{2}0$). Left bottom panels in (a and b) show zoom-in images at the interface between hBN layers and sapphire. Right bottom panels in (a and b) are intensity profiles of red arrows in left bottom panels.

Figure 17. GI-WAXD result of trilayer hBN on sapphire substrate.

Figure 18. XPS spectra of (a) B 1s, (b) N 1s, and (c) Al 2p on tri-, bi-, and monolayer hBN, respectively. All samples are grown by plasma-assist CVD method.

Figure 19. Schematic illustration of trilayer hBN on sapphire. Al-N bonds are formed between the bottom hBN and Al on the top of sapphire

Figure 20. (a) Schematic illustration of separation of monolayer hBN from sapphire by wet-etching transfer method. (b) B 1s, N 1s, and Si 2p XPS spectra of as-transferred monolayer hBN on SiO₂/Si. (c) B 1s, N 1s, and Al 2p XPS spectra of sapphire after delamination of hBN.

Figure 21. (a) TEM analysis of as-transferred trilayer hBN on SiO₂/Si. Left bottom panels in (a) show zoom-in images at the interface between hBN layers and SiO₂/Si. Right bottom panels in (a) are intensity profiles of red arrows in left bottom panels. (b) GI-WAXD result of trilayer hBN on SiO₂/Si substrate.

Figure 22. (a) A photograph for the WVTR measurement. (b) WVTR results of PET, 1.2-nm-thick single-crystalline hBN, and 2.1-nm-thick polycrystal hBN films.

Figure 23. (a) Schematically drawn polymer casting method on hBN film grown on sapphire. (b) SEM image of hBN film on porous PES support. Inset of (a) is a photograph of as fabricated large-scale gas transport membrane. (c) Cross-section SEM image of PES support indicates a hierarchical pore structure with ~500 nm pores located underneath hBN film. The thickness of entire membrane is ~ 30 μm.

Figure 24. Gas permeation and separation performance through hBN/PES supporting membrane at room temperature. (a) Permeances of six molecules through a trilayer hBN film. (b and c) Ideal selectivity for H₂/CO₂ and H₂/N₂ gas pairs from three membranes. (d) The gas mixture (H₂/CO₂) separation performance of trilayer hBN film/PES support.

List of Tables

[Chapter 2]

Table 1 | Comparison of HER activity of hBN/Ni₂₃B₆ catalysts.

Table 2 | Comparison of HER activity of nickel boride catalysts in acidic electrolytes.

[Chapter 3]

Table 1 | Concentrations of Al-N bonding in mono-, bi-, and trilayer hBN films.

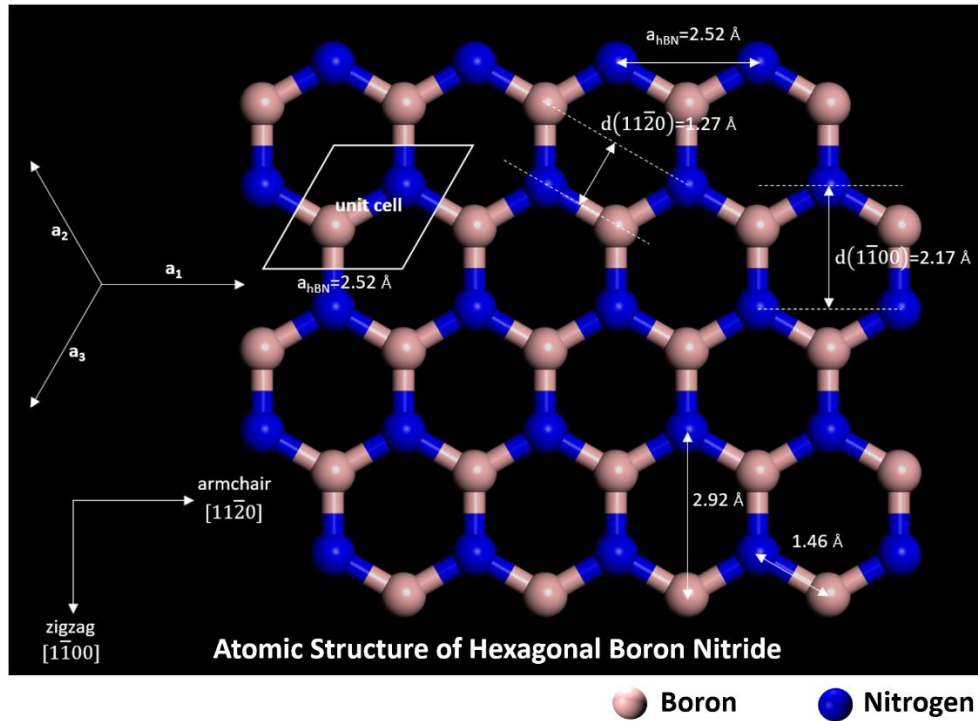
Table 2 | Ideal selectivity of trilayer hBN/PES support membrane compare to Knudsen selectivity and monolayer graphene.

Chapter 1: Research Background for the Two-Dimensional Hexagonal Boron Nitride: Preparation and Property

1.1 Overview

Since the discovery of graphene, two dimensional (2D) materials are attracting attention in various promising future electronics and photonics due to their potential for extending Moore's law of the number of transistors in an integrated circuits¹. Hexagonal boron nitride (hBN) is a perfect 2D insulator due to the wide bandgap of ~ 6 eV²⁻⁴, posing great potential in electronics. Given the atomic structure, hBN dielectric can prevent the charge scattering, leading to intrinsic performance of channel materials (Figure 1). For this reason, hBN has been considered as a promising substrate to construct high-performance 2D electronic device⁵⁻⁸. To achieve practical applications, the preparation of large-size and high-quality of uniform hBN film is the most important issue. For the past few years, the preparation methods of hBN have been vigorously developed by top-down and bottom-up approaches^{9, 10}. In particular, bottom-up synthesis method has been paid attention to the most promising way to achieve a scale up of hBN crystal using chemical vapor deposition (CVD) on transition metal catalysts and dielectric substrates¹¹. Furthermore, unique chemical and physical properties of hBN films have been contributed to the growth platform of 2D materials, dielectrics, protecting layer, and sieving membrane applications^{5, 6, 12-15}.

In this chapter, I review summary of recent trends in the growth method and application with novel property of hBN. Two types of sub-chapters will be demonstrated: 1) preparation and 2) properties and applications of hBN.



Structure	Bandgap	Thermal stability	Thermal conductivity
Hexagonal	~ 6 eV	~ 1,000 °C	~ 800 W m ⁻¹ K ⁻¹

Figure 1. Atomic structure and properties of hexagonal boron nitride.

1.2 Top-down approaches for the preparation

The first isolation of thin sheets of hBN was reported by Zettl's group in 2008 (Figure 2a-c)¹⁶. For delaminating hBN sheets from bulk hBN crystal, they utilized the Scotch tape technique demonstrated by Novoselov *et al.* Optical images of hBN sheets also revealed obvious difference of contrast depending on the number of layers (Figure 2d-f)¹⁷. The Scotch tape technique, called a mechanical exfoliation, can provide several micron-scale high-quality hBN sheets. This mechanically exfoliated hBN sheet has been used for designing and fabrication proof-of-concept electronics. By using the mechanical exfoliation technique, mono- and few-layer hBN were successively achieved for characterizing their hexagonal structure, chemical states, and defect dynamics. However, this method is extremely difficult to control their morphologies and the number of layers in such films. Furthermore, one can only obtain micron-scale 2D crystals and the yield for a target layer count, such as monolayer hBN, is too low.

Liquid exfoliation is an efficient method for the preparation of mono- and few-layer hBN flakes in large quantities¹⁸⁻²³. The ion intercalation and sonication-assisted exfoliation were representatively utilized (Figure 3a-c)¹⁸. For the ion intercalation method, various ions, such as lithium, potassium, and sodium ions, were used to break up van der Waals forces between hBN layers^{20, 21}. Regarding sonication-assisted hBN exfoliation, urea, isopropyl alcohol, N,N-dimethylformamide, ethanol/water mixture, and water have been used for appropriate solvents (Figure 3d-e)^{18, 19, 22, 23}. Although the liquid exfoliation method gains control over thickness of nanosheets, it inevitably suffers from a fairly wide range of thickness distribution. The size of hBN sheets are limited to several-hundred-micron scale, as well as extrinsic contaminations, introduced from mixing solvents, cause the degradation of quality and properties of exfoliated hBN flakes.

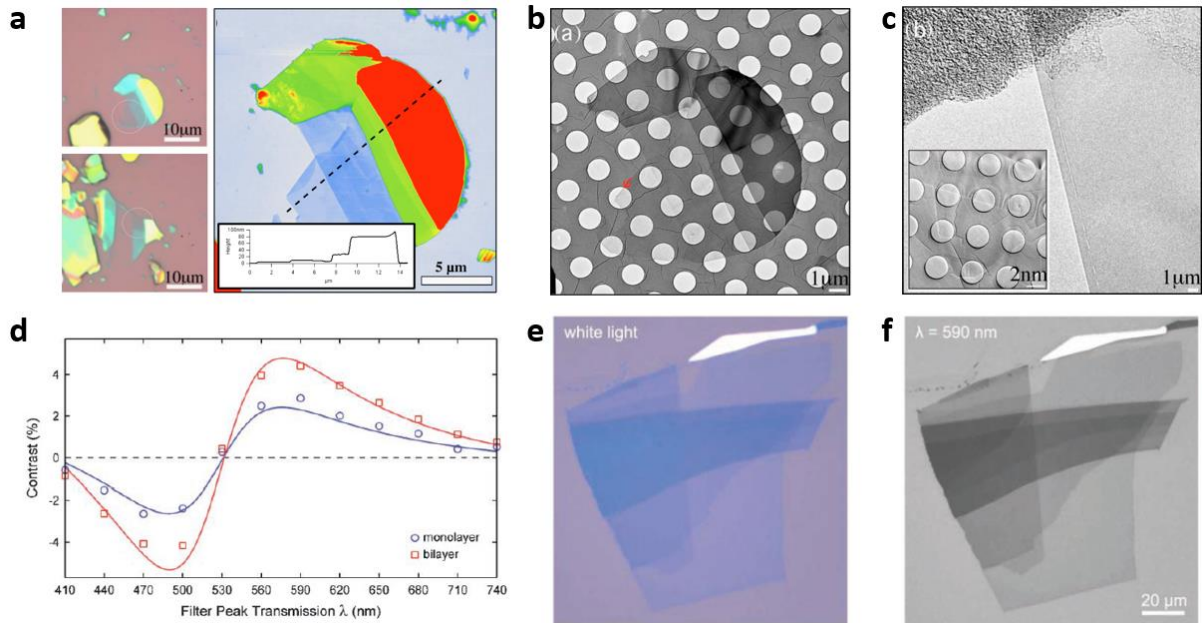


Figure 2. (a) Optical (left) and AFM (right) images of mechanically exfoliated hBN nanosheets on SiO₂/Si substrate. The dashed line indicates the height profile (inset) of exfoliated flake. (b) Low magnification TEM image of (a). (c) High-magnified images at red arrow in (b), showing the number of layers. The thinnest area is shown in inset of (c)¹⁶. (d-f) Wavelength dependency of optical contrast for monolayer and bilayer hBN on SiO₂ (90 nm)/Si substrate¹⁷.

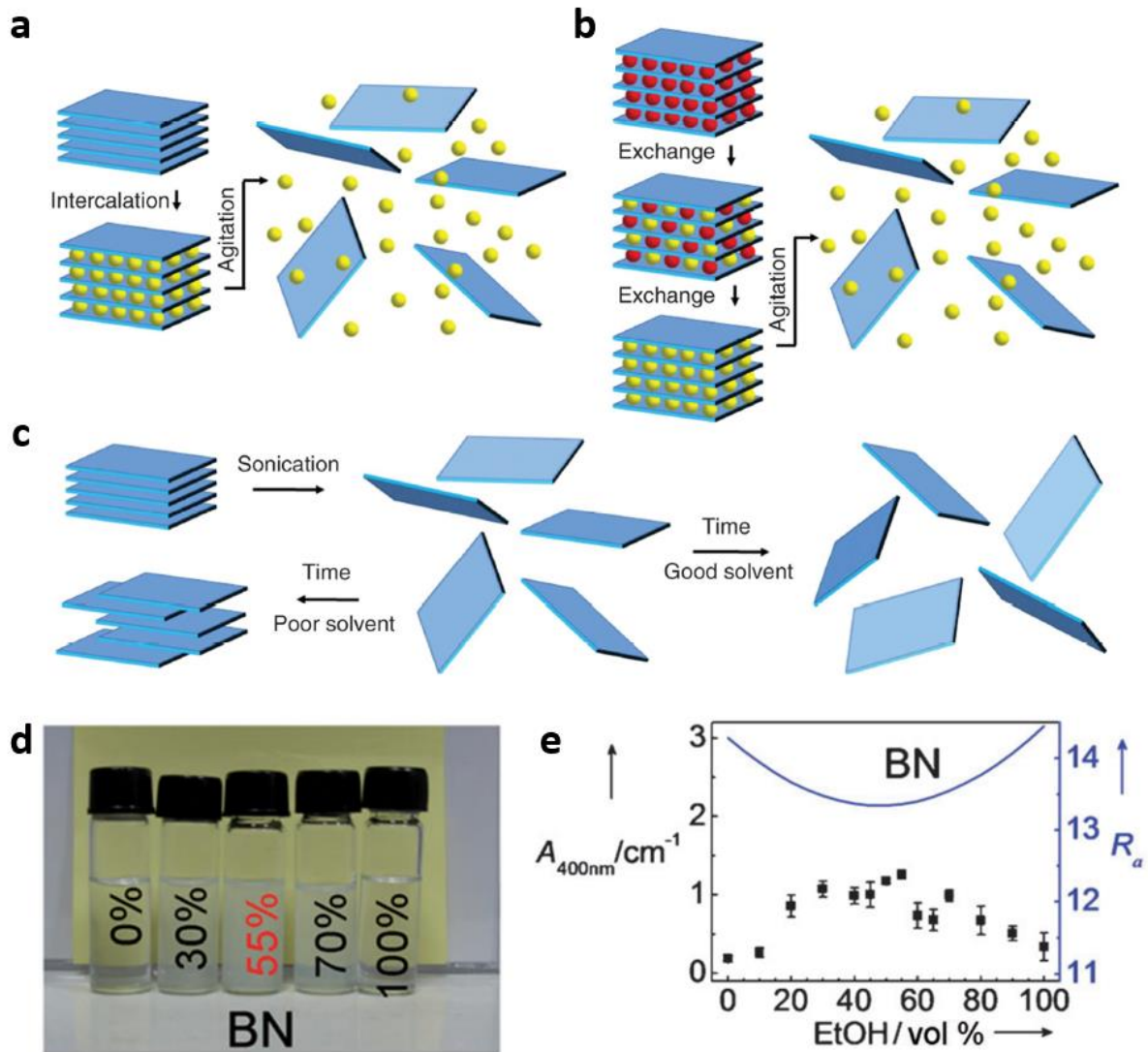


Figure 3. Schematic illustrations of the liquid exfoliation method of (a) ion intercalation, (b) ion exchange, and (c) sonication -assisted exfoliation. In the ion intercalation method, intercalated ions (yellow circles) separate the hBN layers. The ion exchange method uses substitution process of originally contained ion to larger ions. The sonication-assisted method should utilize the stable solvents to avoid reaggregation and sedimentation¹⁹. (d) Photographs of dispersed BN solution in various EtOH/H₂O ratio of mixture. (e) The absorbance of BN solutions at different EtOH/H₂O mixtures²².

1.3 Bottom-up approaches using the chemical vapor deposition

The development of high-quality, uniformity in large-area, and layer-controllable 2D materials is required for usable applications in electronic and optical devices. The CVD method has been widely considered to achieve ultimate pursuit of 2D crystals preparation. The similar approaches for graphene growth are adopted as production method for hBN growth in the CVD method. As grown mono- and multilayer hBN films proved their ability for insulating and protecting properties compare with conventional SiO₂ in nanoelectronics^{5, 6}. In particular, thermal CVD and plasma-enhanced (PE) CVD have been employed as promising two main technologies. The thermal CVD entails the chemical reaction between thermally activated precursors and growth substrate, which leads to the nucleation of hBN grains and growth into a continuous film. Entire procedure is determined by heat energy. The [Figure 4a](#) shows illustration of typical thermal CVD system composed of the growth substrate in heating zone and supplier of BN precursors, such as gas phase (diborane, B₂H₆ and ammonia, NH₃)²⁴, liquid phase (borazine, (BHNH)₃)^{25, 26}, and solid phase (ammonia borane, BH₃NH₃)^{27, 28}. During the growth, operating pressure lead to decide the reaction ways. The low-pressure (LP) and atmospheric-pressure (AP) CVD methods are widely used up to now. While LPCVD focuses the control of surface reaction rate, APCVD focuses the control of mass transport. Another promising approach is PECVD, which aid the dissociation and activation of the BN precursor ([Figure 4b](#))²⁹. The generation of plasma is utilized by microwave discharge or radio frequency technique. The lowering growth temperature and high growth rate of hBN are employed by highly active chemical environment compare with conventional thermal CVD. Therefore, PECVD system has been received considerable attention for low-temperature growth of hBN. For examples, few-layer continuous hBN films on Cu were obtained at 800 °C by employing a radio frequency plasma to dissociate borazine.

Here, I summarize the recent CVD approaches for the growth of mono- and multilayer hBN on various substrates in four sections: 1) growth mechanism, 2) growth of monolayer hBN, 3) control of the number of layers, and 4) direct growth of hBN on dielectrics.

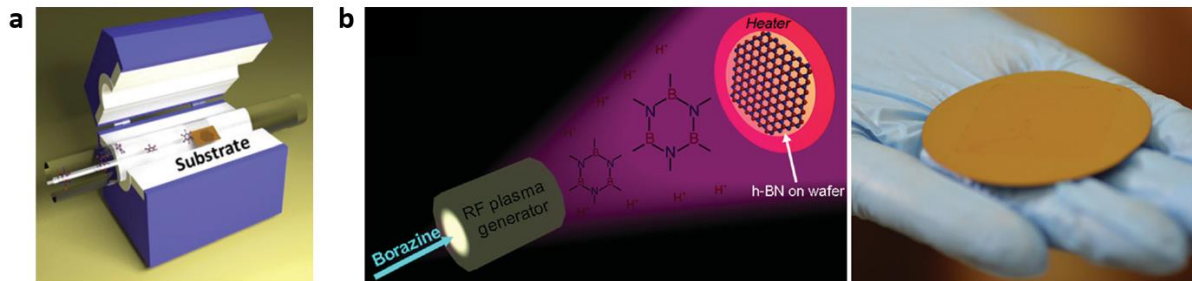


Figure 4. Schematics of representative CVD method for hBN growth. (a) typical thermal CVD¹¹, (b) plasma-enhanced CVD²⁹.

1.3.1 Growth mechanism of hBN: surface diffusion, precipitation, and epitaxy

The CVD-derived growth of hBN on various substrates can be categorized into surface-diffusion mediation and precipitation of B and N species in the whole process. Similar with graphene study, when precursors are exposed to substrate at a typical growth temperature, a capability of precursors plays a function as a boundary for two possible mechanisms. For examples, the Cu substrate leads to the surface-diffusion mediated growth of monolayer hBN due to the extremely low solubility of B and N atoms (Figure 5a)³⁰. In addition, single-crystalline substrate including single-crystal metal and sapphire wafer give an opportunity of epitaxial growth of single-crystal hBN (Figure 5b)³¹. On the other hand, the Fe substrate leads to the precipitation of B and N atoms during cooling process. The precipitation mechanism typically promotes a low uniformity of hBN films due to the solubility differences between B and N atoms (Figure 5c)³². Recently, metal alloys were developed for uniform precipitation of multilayer hBN films (Figure 5d). The concentration of alloy was systematically controlled by deposition thickness of each metal film³³.

1.3.2 Toward single-crystal growth of monolayer hBN on metal catalysts

In recent years, lots of efforts have been paid to grow high-quality hBN on transition metal catalysts such as Cu, Pt, Ni, Fe, and metal alloys using CVD method. Large-scale monolayer hBN was successfully grown on Cu foil utilizing low-pressure (LP) CVD by Kong's group in 2012³⁴. An ammonia borane was used as a solid precursor due to its stability under ambient conditions and accessibility compare to borazine, which is air sensitive and easily hydrolyzed to form boric acid, ammonia, and hydrogen. For the growth of hBN monolayer on Cu surface, the growth temperature of 1000 °C was used with ammonia borane heated up from 60 to 90 °C (Figure 6a). The ammonia borane decomposed into hydrogen, monomeric aminoborane (BH₂NH₂), and borazine (B₃NH₃)₃ species (Figure 6b). They observed triangular and asymmetric diamond shapes at the precursor heating temperature of 60 and 90 °C, respectively (Figure 6c-d). According to previous simulation, triangular shape terminated by N atoms at edge is energetically favorable. However, B-terminated edge is experimentally observed in high flow rate of gas precursor (Figure 6e). They also proposed prefer growth mechanism on Cu by observing merged hBN grains over the grain boundaries of Cu. As grown continuous hBN was transferred onto a SiO₂/Si substrate and visualized in optical microscopic image (Figure 6f). The highly crystalline large-scale monolayer hBN film was demonstrated on Pt foil using LPCVD method²⁷. Herein, for cost-efficiency, an electrochemical bubbling method was adopted to transfer hBN film from the Pt foil to SiO₂/Si substrate (Figure 6g). X-ray photoemission spectroscopy revealed the chemical bond and

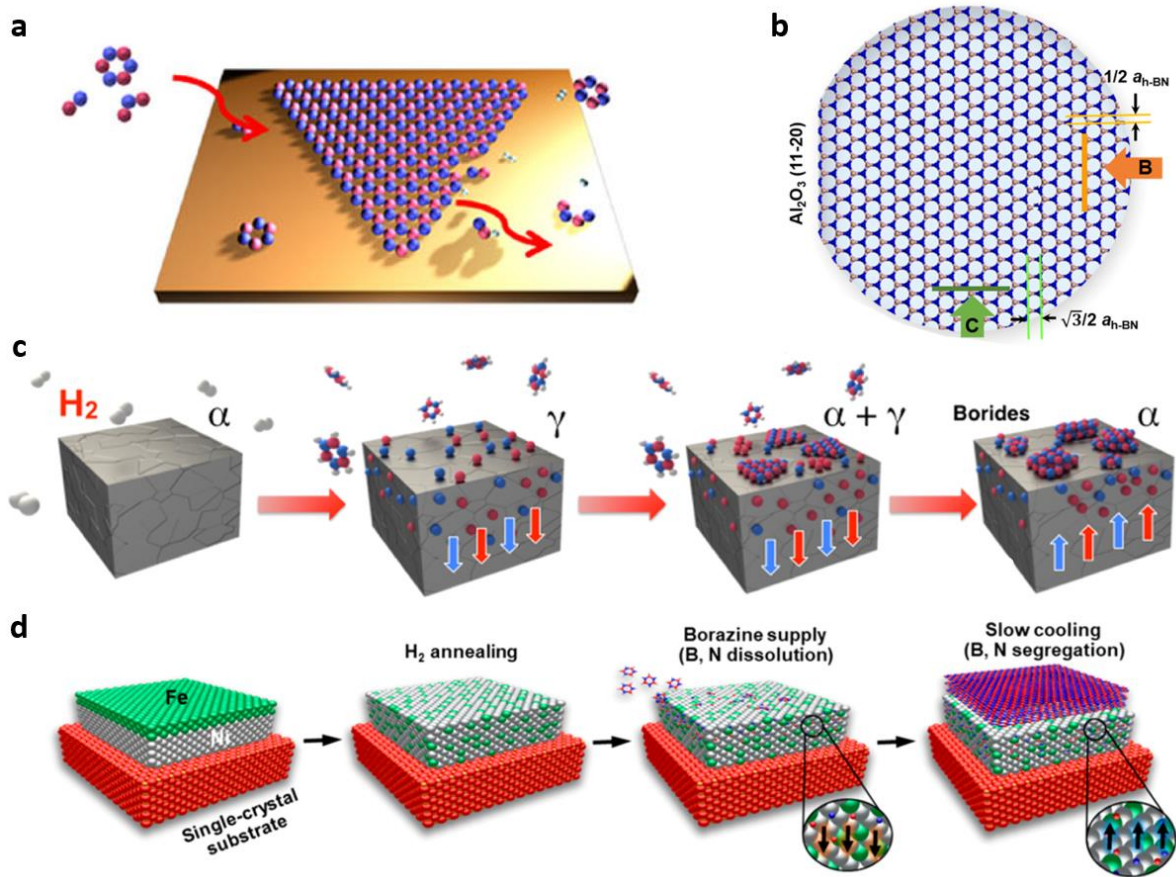


Figure 5. (a) Schematic illustration of surface-diffusion mediated mechanism of hBN growth on Cu surface³⁰. (b) Schematic demonstration of epitaxial relationship of hBN with Al₂O₃³¹. (c) Schematically described growth mechanism of hBN on the Fe catalyst with H₂ atmosphere³². (d) Schematic illustration of the CVD growth step of multilayer hBN on Ni-Fe alloy catalyst³³.

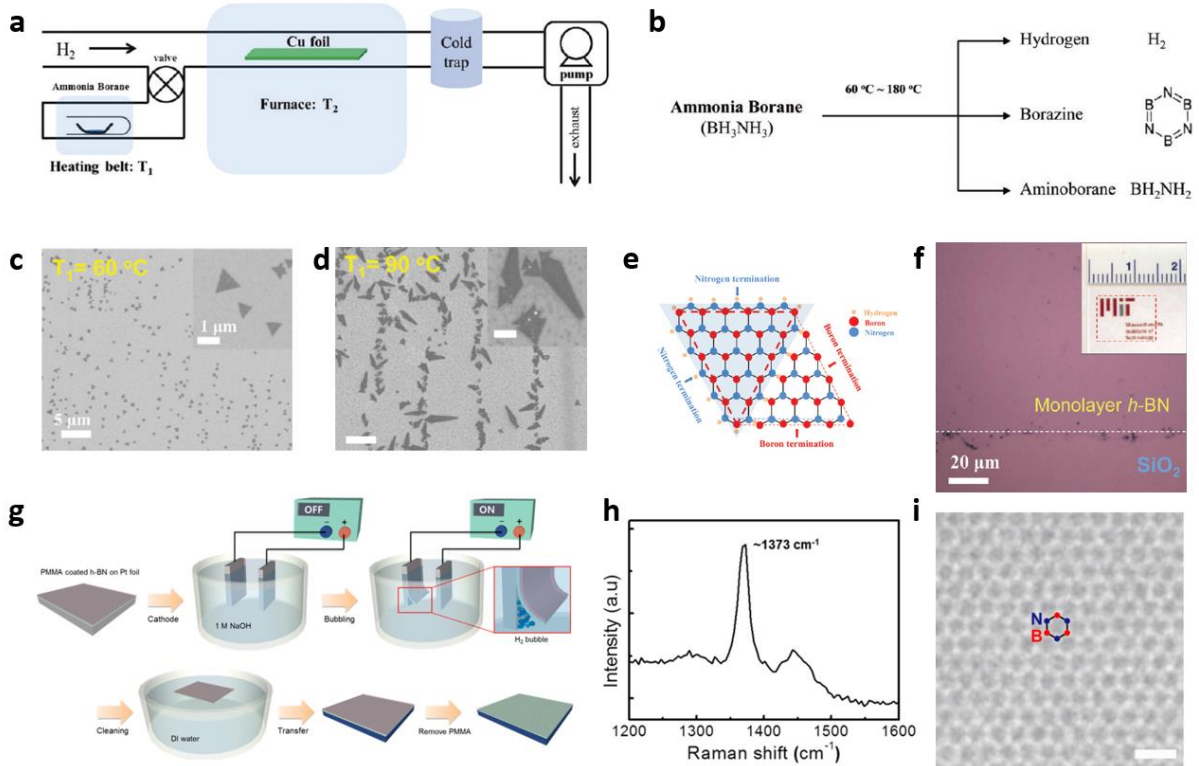


Figure 6. (a) Schematic illustration of hBN growth method using LPCVD setup. (b) Thermal decomposition of ammonia borane, solid precursor, to H_2 , borazine, and aminoborane at 60~180 °C. SEM images resulting from (c) 60 and (d) 90 °C of heating belt temperature, T_1 in (a). (e) Schematic diagram of atomic termination of hBN flake. (f) Continuous hBN film transferred on SiO_2/Si substrate³⁴. (g) Schematic description of electrochemical H_2 bubbling transfer method. (h) Raman spectrum of monolayer hBN on SiO_2/Si . (i) High-resolution TEM image of freestanding monolayer hBN on quantifoil. The inset indicates the electron diffraction pattern of hexagonal structure of hBN²⁷.

atomic ratio of B and N atoms of 1:1. A sharp E_{2g} phonon mode at 1370 cm^{-1} was clearly shown in Raman spectrum (Figure 6h). The hexagonal structure of hBN monolayer was directly observed by high-resolution transmission electron microscopy (HRTEM) (Figure 6h). Furthermore, the selective area electron diffraction (SAED) also indicates a set of hexagonal diffraction spots that are clearly matched with the (10-10) index of hBN monolayer (Inset in Figure 6i).

In the early studies, the grain sizes of CVD-grown hBN were typically on the micron scale. This small grain inevitably leads to high concentration of grain boundaries in the continuous hBN film. The grain boundaries are mostly regarded as a structure defect, resulting in charge impurities. To avoid degradation of performance of hBN dielectric, reducing the density of grain boundaries is highly required with single-crystal hBN. Up to now, several methods are demonstrated for achieving large single-crystal hBN grain to reduce grain boundaries. Electropolishing lowers the surface energy of Cu foil, resulting in a decrease in Gibbs free energy barriers. On a polished Cu surface, approximately $35\text{ }\mu\text{m}^2$ monolayer hBN grains were obtained with reduced nucleation density. The growth method for reducing density of grain boundaries with large hBN grains was demonstrated through the thermal annealed Cu-Ni alloy substrate (Figure 7a)³⁵. The largest size of hBN grains with side lengths up to $130\text{ }\mu\text{m}$ were obtained (Figure 7b-e) by time-dependent growth on alloy concentration of $\sim 15\text{ }\%$ Ni. By further investigating the effect of Ni concentration, the enhanced decomposition of poly-aminoborane (BH_2NH_2) precursor was observed at high Ni concentration. To obtain a large-single crystal monolayer hBN grain, nucleation control was performed on a Si-doped Fe substrate by Hofmann's group (Figure 7f)³⁶. The bulk Fe substrate, one of strong catalysts for hBN growth, has been used for the multilayer hBN growth via a precipitation process due to the high solubility of B ($\sim 0.1\text{ at } \%$) and N ($\sim 8.0\text{ at } \%$)^{37, 38}. They prepared thin Fe film by the metal deposition method to use for monolayer hBN growth. The Si dopants facilitated the reducing nucleation density of hBN grain with reduced solubility of B and N species in Fe. Under optimized growth condition, the grain size of triangular hBN flakes show with lateral dimensions of $\sim 0.3\text{ }\mu\text{m}$ and that of continuous film shows above $25\text{ }\mu\text{m}$ (Figure 7g-h). Subsequently, they designed pre-filling of NH_3 in bulk Fe before the growth stage³². This approach leads to grow the uniform monolayer hBN by limits the uptake and restrain the precipitation of B and N species (Figure 7i). Despite efforts to grow large-scale hBN with reducing grain boundaries, the growth of single-crystal hBN film from one single-crystal grain has not been achieved yet.

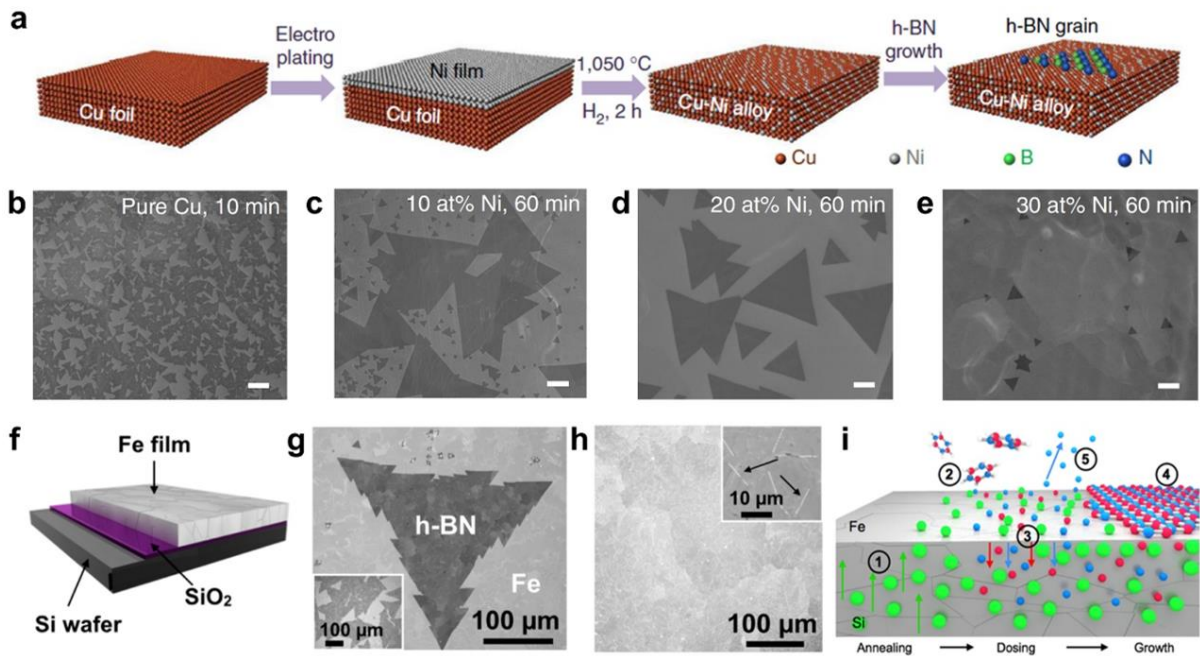


Figure 7. (a) Schematic procedure of the hBN growth on a Cu-Ni alloy. SEM images of hBN grains grown on a pure Cu (b) and Cu-Ni alloy with (c) 10 %, (d) 20 %, and (e) 30 % Ni concentrations³⁵. (f) Schematic illustration of a Fe/SiO₂/Si catalyst system³⁶. (g) SEM image of the largest hBN flake grown on a Fe/SiO₂ (300 nm)/Si substrate. The inset shows a corresponding low-magnification SEM image. (h) Continuous hBN film on a Fe surface. Black arrows in the inset image indicate grain boundaries. (i) Schematic illustration of the proposed growth mechanism. (1) The lower Si diffuses into the upper Fe via thermal annealing. (2) The dehydrogenation and dissociation of borazine occur when borazine precursor reach to the Fe surface. (3) B and N atoms dissolve in Fe surface. (4) After saturation, nucleation, and growth of the hBN are observed on the Fe surface. (5) Some loss of N from the Fe surface into the N₂ phase occurs.

Recently, several reports have been demonstrated to grow large-scale single-crystal monolayer hBN film. The pioneering work by *Lee et al.* presented single-crystal monolayer hBN film via self-collimated grain formation¹⁵. The growth procedure is illustrated in [Figure 8a](#). Liquid Au on a W substrate was prepared by heating the substrate to 1100 °C. The key of growth method is maintaining a flat liquid surface with high surface tension to achieve strong adhesion to borazine ([Figure 8a, Step i](#)). The hBN nuclei were observed at the early stage ([Figure 8a, Step ii](#)). While the solubility of B is ~0.5 at %, that of N is ~0 at % in liquid Au at 1100 °C^{39, 40}. This ensure prevalent surface diffusion-mediated growth rather than precipitation. The density of circular hBN grain increases under continuous supply of borazine ([Figure 8a, Step iv](#)). The mechanism for the alignment of hBN grain was demonstrated by rotation (less than 60°) of individual grains with respect to each other based on attractive Coulomb interactions between B (Lewis acid) and N (Lewis base) ([Figure 8a, Step iii](#)). This grain rotation based on electrostatic interactions leads to seamless stitching via self-collimation. The authors proposed that the cohesive energy between B and N is much stronger than that of B-B or N-N. A continuous single-crystal monolayer hBN film was grown and proved by further borazine supply ([Figure 8a, Step iv-v and Figure 8b-c](#)). However, the use of liquid Au is unsuitable for applying industry, which requires low cost, cross-contamination, and process controllability. Therefore, single-crystal Cu was prepared to develop the improving growth method for single-crystal hBN. Liu's group presented the growth of a 100 cm² single-crystal monolayer hBN for the first time using a low-symmetry Cu (110) vicinal surface fabricated by preannealing method ([Figure 8d](#))⁴¹. The unidirectional alignment of hBN grains was directly observed and characterized at early growth stage on Cu (110) ([Figure 8e-f](#)). The single-crystalline film was elucidated by TEM study and H₂ etching ([Figure 8g](#)), which is approach for visualizing a grain boundary. However, the any grain boundary was not observed in single-crystal monolayer hBN film. Furthermore, edge coupling of hBN with that of Cu (110) were demonstrated by a combination of structure characterizations and theoretical simulations ([Figure 8h-i](#)). The edge of hBN grain was tightly attached to the upward side of Cu step edge, <211> direction. This phenomenon shows the lowest formation energy of hBN long the <211> direction of Cu (110) at $\gamma = 0^\circ$, where γ is the angle between the zig-zag direction of h-BN and the Cu <211> direction based on *ab initio* calculations. Sequentially, similar approach for single-crystal monolayer hBN was performed on Cu (111). The high symmetry surface plane of Cu (111) leads to the emergences of two-preferred opposite orientation, which cause grain boundaries^{41, 42}. However, Li's group broken this knowledge by presenting successful epitaxial growth of single-crystal monolayer hBN on Cu (111) film/c-plane sapphire (Al₂O₃) wafer ([Figure 8j-k](#))⁴³. They suggest that single-orientation hBN grains were grown by lateral docking of hBN to Cu (111) steps, ensuring the unidirectionally alignment. The simulation results proposed that the step edges on Cu (111) cause large energy barrier to grow mono-oriented hBN grains ([Figure 8l](#)).

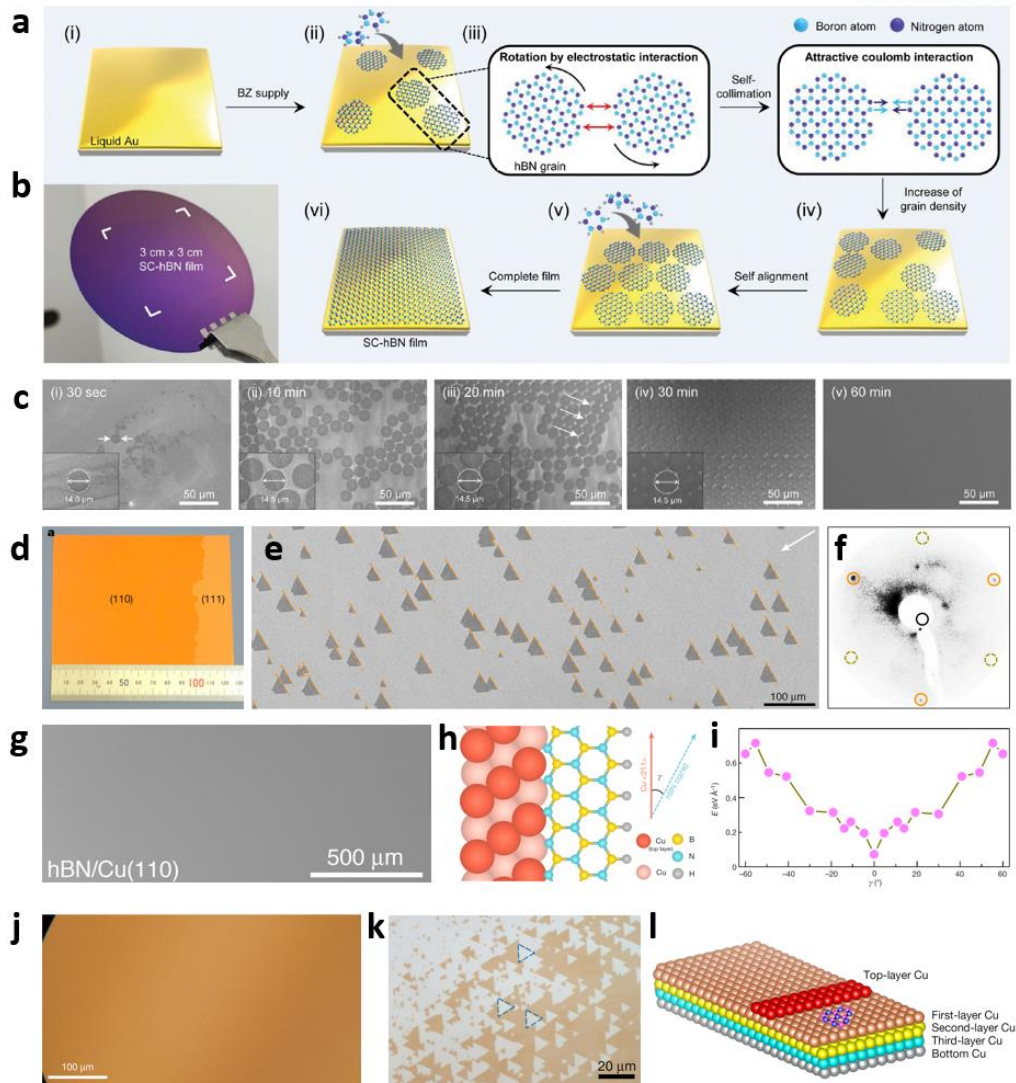


Figure 8. (a) Schematic illustrations of the growth of single-crystal hBN films from self-collimated circular hBN grains with rotation induced by the attractive Coulomb interactions of B and N edges between grains (i-vi). (b) Photograph of 3 x 3 cm² single-crystal hBN film on SiO₂/Si wafer. (c) SEM images of time-dependent hBN growth from nuclei to uniform film. (d) Photograph of a 10 x 10 cm² single-crystal Cu (110) fabricated by thermal annealing. (e) SEM image of unidirectionally aligned hBN grains on the Cu (110) surface. (f) Low-energy electron diffraction (LEED) pattern of hBN grain. Based on triple symmetry, three dots marked by orange circle show stronger intensity than the other three dots marked by green circle. (g) SEM image of single-crystal hBN after H₂ etching process at 1000 °C. (h) Schematics of the configuration between the hBN lattice and the atomic step of Cu (110). (i) First-principles DFT calculations of the formation energies of hBN edges bonded with Cu <211> step edge. (j) Optical image of a Cu (111) thin film. (k) single orientation of hBN grains on Cu (111). (l) DFT calculation of the lowest-energy structure of the NiB_{II}-Cu (111).

1.3.3 Control of the number of layers

Controlling the number of hBN layers with uniformity over the growth substrate is highly desirable as a promising dielectric substrate for 2D-material integrated electronics. Numerous attempts to develop layer-controllable growth method for hBN. As pioneering works in 2010, Ajayan's group reported large-scale growth of hBN film on Cu using APCVD with ammonia borane²⁸. They observed the hBN film mainly consist of bilayer and local tri-to-pentalayer using HRTEM (Figure 9a-b). However, thickness control was not achieved on Cu in this system. Kong's group reported that the thickness of hBN film on Ni upon continuous exposure time and flow rate of borazine²⁵. As a result, they achieved hBN films with thickness of 5 and 50 nm at 1 sccm (30 min) and 10 sccm (1 h), respectively. The layer control of hBN also demonstrated by Ruoff's group²⁴. They obtained various thickness of hBN ranging from a few-layer to a hundred-layer on Ni foil under different growth time (Figure 9c). They investigated growth mechanism by comparing sequential growth method using separated B and N precursors (diborane and ammonia). The sequential growth proved that while B atoms show high dissolution rate and alloying reaction of B atoms in bulk Ni, N atoms do not react with Ni (Figure 9d-e). In conclusion, they suggest that B reacts with the Ni to form a nickel boride which then further reacts with ammonia, leading to the growth of hBN. According to the growth of hBN on polycrystal Ni foil, thickness of hBN grains strongly depends on the crystal orientation of underlying Ni. Li's group demonstrated the growth rate was promoted on Ni (100) but not detectable on Ni (111), suggesting that growth kinetic should be taken into consideration during CVD growth of hBN⁴⁴.

As described in **Section 1.3.2**, Fe, possessing high solubility for B and N atoms, has been used for preparing multilayer hBN film. Kim *et al.* obtained large-area multilayer hBN film on Fe foil by using the borazine at 1100 °C (Figure 9f-g)²⁶. The hBN thickness was controlled by the cooling rate (Figure 9h). A relatively thin hBN film of 11.9 nm was obtained at a fast cooling rate of 30 °C/min whereas a thicker film of 17.8 nm was achieved at a slow cooling rate of 5 °C/min. This result indicates hBN growth on Fe is mainly generated by segregation and precipitation of B and N atoms from bulk Fe. The crystallinity of as-grown hBN film was comparable with mechanically exfoliated hBN multilayer (Figure 9i-j).

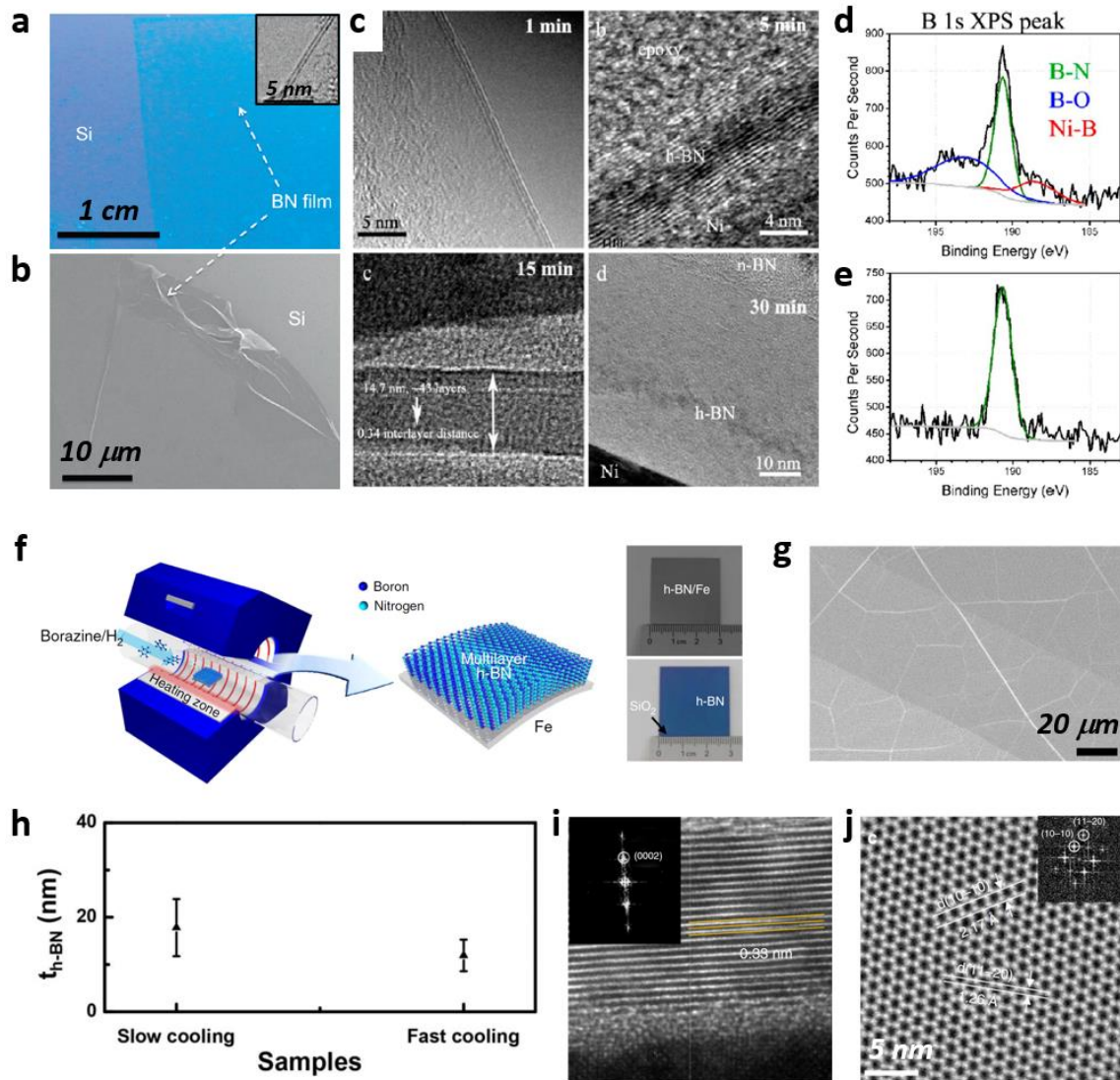


Figure 9. (a) Optical and (b) SEM images of large-area hBN film. Inset in (b) shows HRTEM image of the film edge showing bilayer hBN²⁸. (c) TEM images for hBN growth as a function of different growth time (1, 5, 15, and 30 min). (d) B1s XPS spectrum of sequential growth with diborane first. (e) Sequential growth with ammonia first²⁴. (f) schematics of the CVD method for multilayer hBN growth on Fe foil using borazine. Right panels are showing photographs of as-grown hBN/Fe foil and as-transferred hBN/SiO₂/Si. (g) SEM image of a hBN film on Fe foil. (h) Average thickness of show and fast cooling. (i) cross-sectional TEM and (j) High-angle annular dark-field scanning transmission electron microscopy image of multilayer hBN film²⁶.

1.3.4 Direct growth of hBN on dielectrics

The growth of hBN without transition metal catalysts is desired due to contamination issue from transfer process and direct fabrication of device applications. As pioneering works in 2011, Kim *et al.* presented direct deposition of hBN on Si (001) and Al₂O₃ (0001) wafer using conventional thermal CVD method⁴⁵. They obtained few-layer hBN film on Al₂O₃ (0001) at 1000 °C (Figure 10a-b). However, hBN was not shown on Si (001). The successful direct growth of uniform hBN on SiO₂ was presented by boron-oxygen chemistry route for oxygen-assisted hBN nucleation in LPCVD (Figure 10c)⁴⁶. The authors elucidated importance of oxygen by comparing with the hBN growth on Si substrates, displayed no growth of hBN. They proposed that the hBN nucleation is initialized from bounded B radicals at O dangling bond of SiO₂ by existence of B-O chemical bond in X-ray photoemission spectra (Figure 10d).

Recent studies are showing the epitaxial growth of multilayer hBN over a Al₂O₃ wafer. The high-temperature and low-pressure CVD system was adopted for AA'-stacking single-orientation multilayer (2-6 layer) hBN film without wrinkle structure, leading to highly smooth surface (RMS: 0.169 nm) over 2-inch Al₂O₃ wafer (Figure 10e-f)³¹. As grown multilayer hBN on Al₂O₃ (0001) indicates the epitaxial relationship of hBN [0002] || Al₂O₃ [0002] and hBN [1 $\bar{1}$ 00] || Al₂O₃ [11 $\bar{2}$ 0], investigated by LEED, TEM, and DFT calculations (Figure 10g-h). The achievement of thicker hBN with controlling thickness from 10 to 70 nm was demonstrated by a vapor-liquid-solid growth (VLSG) method (Figure 10i)⁴⁷. The authors suggest liquid-phase Fe₈₂B₁₈ alloy catalyst, having low melting point (~1180 °C), aid efficiency of decomposition of N₂, bonding between B-N, and growth rate of the multilayer hBN. The hBN thickness *via* VLSG method was simply controlled by temperature and growth time as shown in Figure 10j-n. The quality of hBN films was characterized by Raman spectroscopy, showing the clear E_{2g} phonon mode at 1366-1368 cm⁻¹ (Figure 10o).

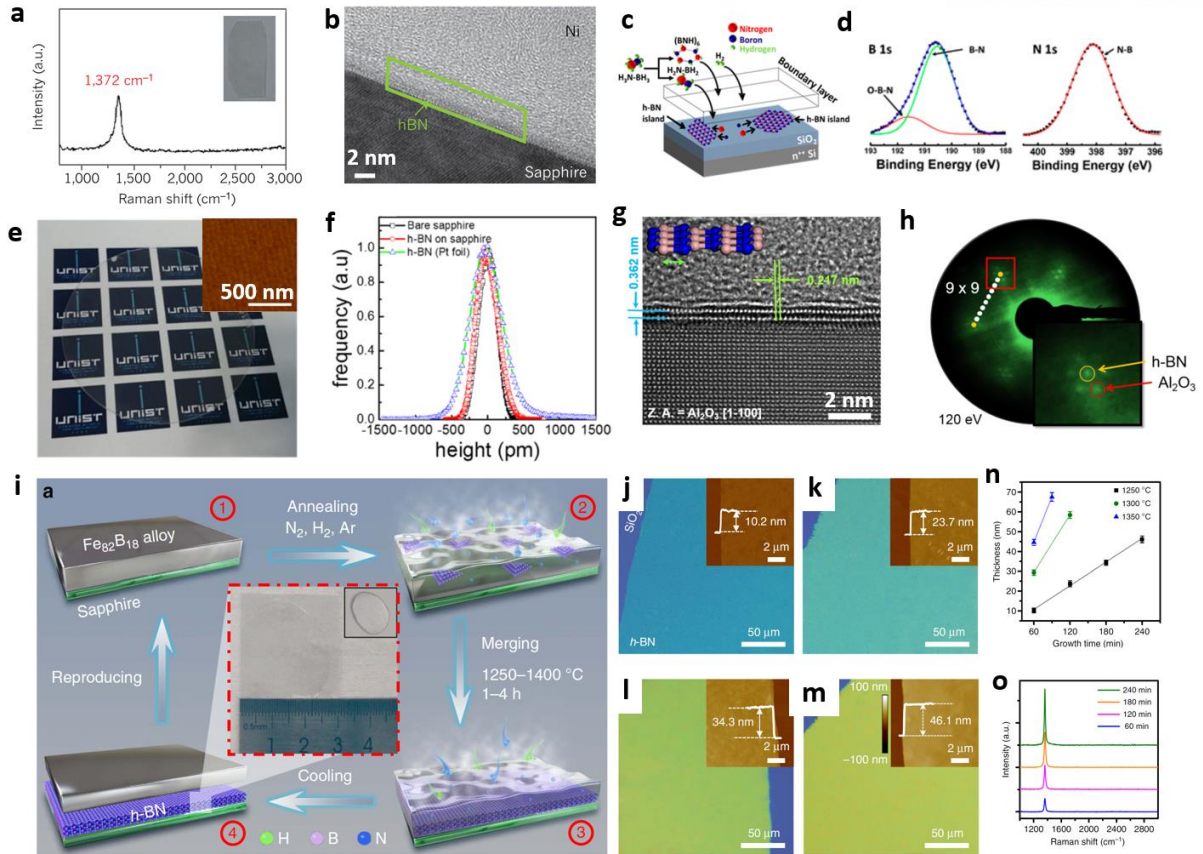


Figure 10. (a) Raman spectrum of hBN grown on Al_2O_3 , indicating E_{2g} phonon mode of hBN. (b) Cross-section TEM image of hBN on Al_2O_3 ⁴⁵. (c) Proposed growth mechanism of the oxygen-assisted, transfer-free CVD growth of hBN. (d) XPS spectra for B 1s and N 1s. The B-O peak in B1s spectrum shows the presence of B-terminated edges bonded with SiO_2/Si ⁴⁶. (e) A photograph of 2-inch wafer-scale hBN grown on Al_2O_3 . The inset shows highly smooth surface. (f) The histogram of distribution for surface roughness. (g) Cross-section TEM image of epitaxially grown multilayer hBN parallel to Al_2O_3 (11-20). (h) LEED pattern is indicating that the superstructure of single-orientation hBN film on Al_2O_3 with small strain effect of 2.6%³¹. (i) Schematic illustrations of multilayer hBN grown on Al_2O_3 by using $\text{Fe}_{82}\text{B}_{18}$ alloy and N_2 gas for B and N precursors, respectively. (j-m) Optical images of hBN grown on Al_2O_3 with (j) 60, (k) 120, (l) 180, and (m) 240 min at 1250 °C. Insets show corresponding AFM height profiles at the edge of film. (n) The summary of relationship between growth time and thickness. (o) Raman spectra of as-prepared multilayer hBN films⁴⁷.

1.4 Properties and applications of hBN

hBN has been considered as a useful platform as growth template, dielectrics, protection-layer for 2D material-based electronics and photonics due to the atomically-flat inert surface and outstanding chemical and thermal stability of hBN. In this section, I introduce recent advances in not only direct growth of graphene and transition metal dichalcogenides (TMDs) on CVD-grown hBN but promising applications using hBN film.

1.4.1 Growth platform for graphene and transition metal dichalcogenides

The direct growth of 2D materials including graphene, transition metal dichalcogenides (TMDs) on hBN has stimulated interest in 2D heterostructure study. The in-situ growth method of graphene/hBN stacking structure using CVD was introduced by Liu's group⁴⁸. They demonstrated a temperature-triggered chemical switching derived LPCVD method on Cu foil. At the growth temperature below 900 °C, growing graphene on hBN was achieved by exposing benzoic acid on hBN substrate. The benzoic acid carbon source is decomposed into CO₂ and hydrocarbon molecules on pyrolysis above 500 °C. During the process, while CO₂ promotes the etching reaction of hBN above 900 °C leading to in-plane G/hBN heterostructure, etching reaction of hBN with CO₂ was not conducted below 900 °C (Figure 11a-e). The continuous graphene/hBN film was obtained by controlling growth time and precursor flow rate (Figure 11f-g). They improve the controllability of method by depositing the well-defined poly(methyl methacrylate) seeds before growing the hBN film on Cu. Controlling the seed deposition, they enabled to reduce the nucleation density of graphene (Figure 11h)⁴⁹. This method gave a chance to obtain high-quality (single-crystal nature of ~85.7%) graphene on hBN as well as construct various graphene patterns on hBN substrate (Figure 11i).

With developing the fabrication methods of graphene/hBN vertical heterostructure, a great deal of efforts has been dedicated to evolve the TMDs and hBN van der Waals heterostructures. As a representative work, direct growth of MoS₂ was achieved on hBN by Fu's group⁵⁰. They utilized the sulfide-resistant Ni-Ga alloy on Mo foil for Mo source for MoS₂ (Figure 12a). The large size and high quality of MoS₂ single-crystal grain up to 200 μm² were presented by microscopic and spectroscopic characterizations (Figure 12b-e).

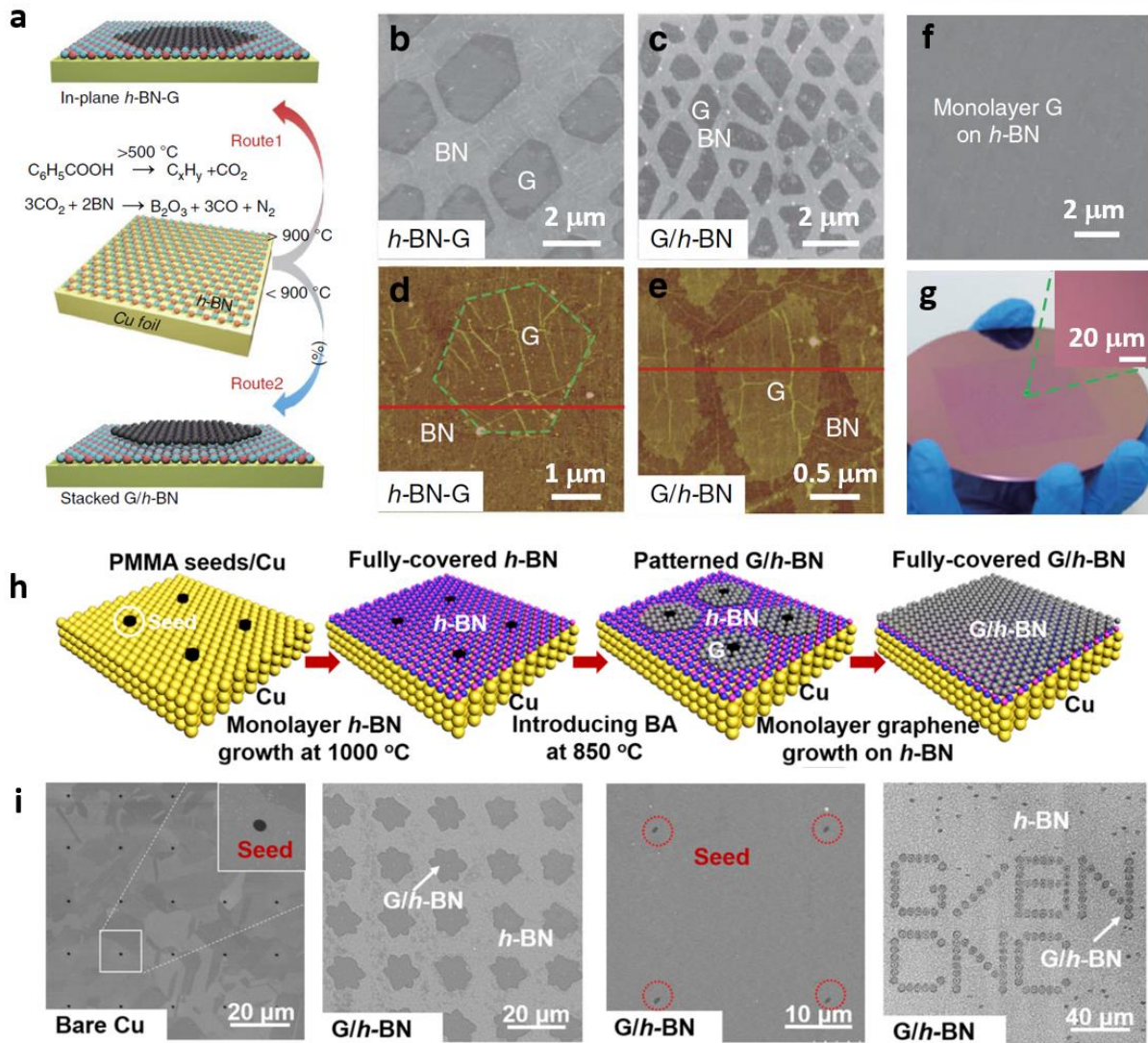


Figure 11. (a) Schematics of the temperature-triggered switching method for in-plane and vertical graphene/ h BN heterostructures. (b, d) SEM and AFM images of in-plane graphene/ h BN heterostructure and (c, e) vertical graphene/ h BN heterostructure, respectively. (f-g) Continuous graphene/ h BN heterostructure film and its optical image on SiO_2/Si after transferring process⁴⁸. (h) Schematic demonstration of CVD-derived patterned graphene/ h BN stack on Cu foil. A pre-deposited PMMA seeds lead to form vertical graphene/ h BN heterostructure grain and continuous film. (i) SEM images of PMMA-seed arrays on Cu surface by electron beam lithography, patterned graphene grain from PMMA, continuous graphene/ h BN heterostructure film, and arranged graphene/ h BN heterostructure⁴⁹.

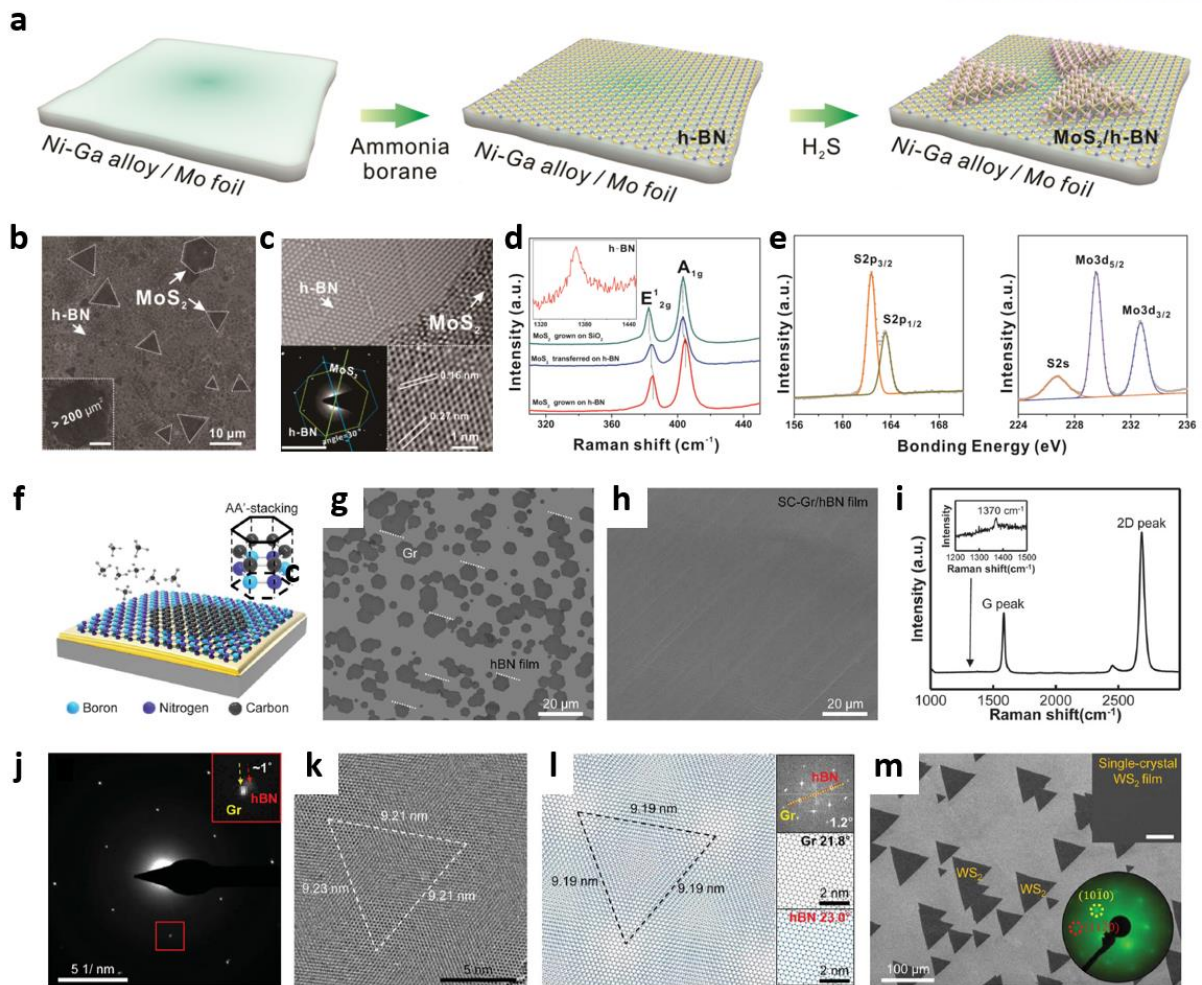


Figure 12. (a) Schematic description of preparation of TMDs/hBN vertical heterostructure. Continuous hBN film is obtained on Ni-Ga alloy in CVD system. MoS₂ growth on hBN is conducted by introducing H₂S gas on hBN. (b) SEM image of the directly grown MoS₂ flakes on hBN. (c) TEM image of MoS₂/hBN vertical heterostructure. SAED pattern shows (110) plane of MoS₂ and (101-0) plane of hBN in the inset. (d) Raman spectra measured on MoS₂/SiO₂, transferred MoS₂, and MoS₂/hBN. (e) XPS spectra of Mo 3d and S 2p of as-grown MoS₂⁵⁰. (f) Scheme of epitaxial graphene growth on single-crystal hBN film. (g) SEM image of as-grown graphene grains showing single-grain orientation and (h) continuous single-crystal graphene film. (i) Raman spectra of graphene/hBN heterostructure. (j) SAED pattern stacked by eight SAED patterns measured on different area of graphene/hBN heterostructure. (k) Experimental and (l) simulated moire pattern between graphene and hBN single crystal. (m) SEM image of triangle WS₂ grains and (inset) continuous film on single-crystal hBN film. LEED pattern indicates (11-20) and (10-10) planes of monolayer WS₂¹⁵.

Recently, single-crystal vertical graphene/hBN heterostructure and single-crystal WS₂ were obtained by using single-crystal monolayer hBN film as a growth platform by *Lee et al*¹⁵. The epitaxial growth of graphene was performed under CH₄ flow (Figure 12f). The alignments of hexagonal graphene grains are clearly visible on single-crystal hBN (Figure 12g). The continuous film was obtained at a prolonged growth time with preserving single-crystal hBN film (Figure 11h). The high crystallinity was confirmed by Raman spectrum (Figure 12i) and TEM characterizations (Figure 12j-l). In particular, the graphene/hBN film shows a clear set of six hexagonal dots in selected area electron diffraction pattern, which proves that the AA'-stacking order with the (10 $\bar{1}$ 0) planes of graphene and hBN. Furthermore, the growth single-crystal WS₂ film was achieved by ex situ growth. To grow single-crystal WS₂ film, W precursor (sodium tungstate dihydrate dissolved in acetylacetone) is coated on single-crystal hBN, and thermal annealing is carried out at 900 °C under ammonium sulfide atmosphere. The triangular WS₂ grains and continuous film were clearly shown in Figure 12m.

1.4.2 Dielectrics for the 2D integrated electronics

The hBN film has been regarded as a promising dielectric substrate for 2D electronics. Recently, monolayer hBN dielectric layer was adopted in graphene-based field effect transistors (FET)⁴⁸. By using temperature-triggered chemical switching growth method, monolayer graphene flakes were prepared on monolayer hBN film (Figure 13a-b). This graphene flake/hBN film was directly fabricated into FET device by transferring onto SiO₂/Si substrate. The measured carrier mobility is 15,000 cm² V⁻¹ s⁻¹, which value showing clear improvement comparing with graphene device without hBN dielectric (Figure 13c). The multilayer hBN is considered to be more appropriate dielectric²⁶. The thicker hBN film assures an excellent dielectric property meaning a low leakage current, reduced charge scattering effect. The multilayer hBN film (5-15 nm) grown on Fe foil leads enhanced mobility of graphene-based FET up to 24,000 cm² V⁻¹ s⁻¹, which outperforms SiO₂ dielectric even fabricated by transfer method (Figure 13d-f).

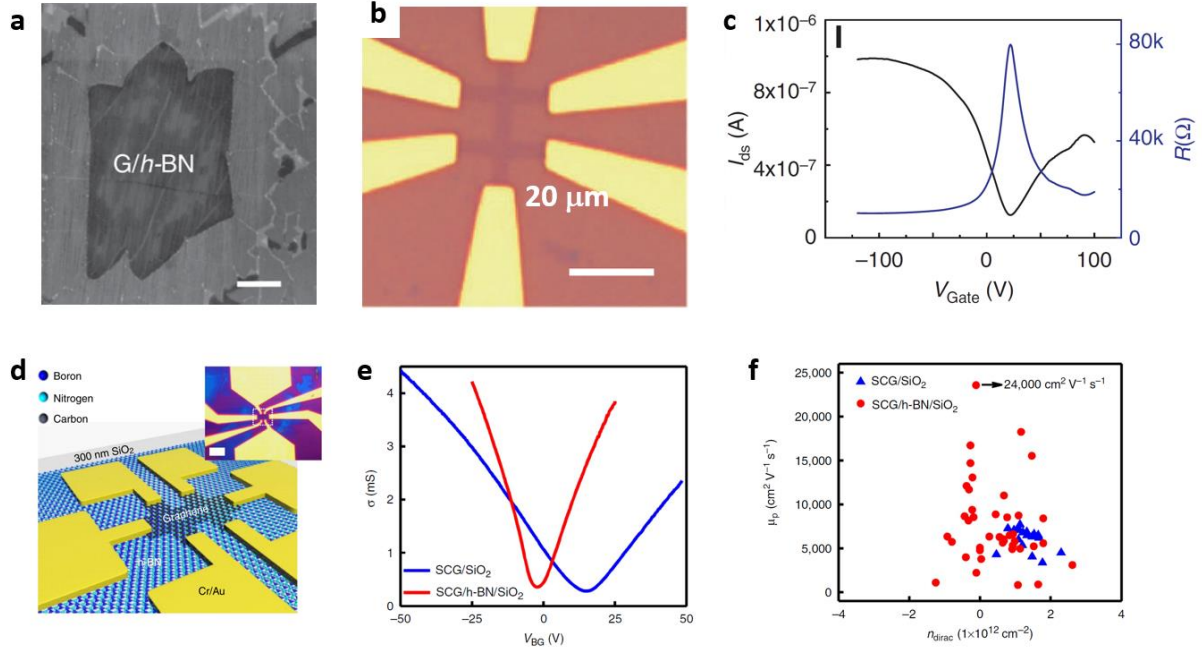


Figure 13. (a) SEM image of the graphene/hBN vertical heterostructure. (b) Optical image of graphene back-gate FET device fabricated on 300 nm SiO₂/Si. (c) Device performance showing the drain current (I_{ds})-gate voltage (V_G) and resistance (R)- V_G curves⁴⁸. (d) Schematic illustration of graphene FET device on multilayer hBN. The inset displays optical image of a as-fabricated device. (e) Conductance (σ) of graphene channel as a function of back gate (V_{BG}). The blue and red curves indicate measurements on SiO₂ and hBN/SiO₂, respectively. (f) Hole mobility (μ_p) plots vs n_{dirac} at different dielectrics of SiO₂ and hBN²⁶.

1.4.3 Protection layer of 2D materials from surrounding

Due to the strong barrier property from chemical inertness and high thermal stability, the hBN film also widely used for an oxidation barrier on pure metals and sensitive 2D TMDs. The oxidation-barrier test was conducted on Cu foil covered with hBN/without hBN at 300 °C exposure in air (Figure 14a)¹⁵. After oxidation test, Cu 2p XPS spectrum clearly presented barrier effect of hBN (Figure 14b-d). While a low signal of CuO was shown on Cu surface with hBN protected region, prominent CuO peaks were presented on Cu surface. The abilities as an oxidation barrier was also demonstrated by water vapor transmission rate (WVTR) measurement (Figure 13e). The WVTR value of single-crystal monolayer hBN shows the lowest permeability (0.6 g/m² day) compare with bare PET (1.44 g/m² day) and polycrystal monolayer hBN (1.01 g/m² day) (Figure 13f). It definitely implies that the necessity of high-quality hBN film without grain boundaries. TMDs including MoSe₂ and WSe₂ use to be degraded in air, UV, and ozone exposure⁵¹⁻⁵³. Therefore, protection of TMD-based photodevice has been required. Shin's group reported that the trilayer hBN effectively protect MoSe₂ and WSe₂ in a harsh environment¹³. They presented prevention of photodegradation by encapsulating hBN films (Figure 13h). The change of photoluminescence (PL) efficiency was systematically investigated at different incident laser powers. (Figure 13i) It was clearly presented that while monolayer hBN is not enough to protect WSe₂, trilayer hBN enable to maintain PL efficiency when irradiation of laser.

1.4.4 Sieving membrane for proton and molecules

Based on theoretical expectations, the potential of utilizing hBN for proton exchange membrane has been attended. An application of hBN film to proton exchange membrane fuel cell (PEMFC) was demonstrated by Yoon *et al.* in 2018¹². They fabricated AA'-stacked trilayer hBN, turbostratic trilayer hBN, polycrystal monolayer hBN, and commercial Nafion 211 membranes for cell tests (Figure 15a). It was shown that the AA'-stacked trilayer hBN presents better performance than polycrystal monolayer hBN for PEMFCs (Figure 15b). The polycrystal monolayer hBN shows high H₂ gas crossover (open circuit voltage (OCV) = 0.886 V, H₂ permeation current density at 0.4 V = 9.60 mA cm⁻²) and a good maximum power density of 0.675 W cm⁻². They prepared turbostratic trilayer hBN to reduce H₂ gas crossover by transfer method. While turbostratic trilayer hBN exhibited enhanced performance (OCV = 0.919 V, H₂ permeation current density at 0.4 V = 6.32 mA cm⁻²), the maximum power density was reduced to 0.63 W cm⁻². This problem was solved by utilizing AA'-stacked trilayer hBN. As fabricated fuel cell using AA'-trilayer hBN exhibited enhanced H₂ gas crossover performance (OCV = 0.957 V, H₂ permeation current density at 0.4 V = 2.35 mA cm⁻²) with maintain a high maximum power density

of 0.657 W cm^{-2} . In addition, the fuel cell fabricated with AA'-stacked trilayer hBN also showed enhanced stability compare to commercial Nafion membrane under harsh conditions ([Figure 15c-d](#)).

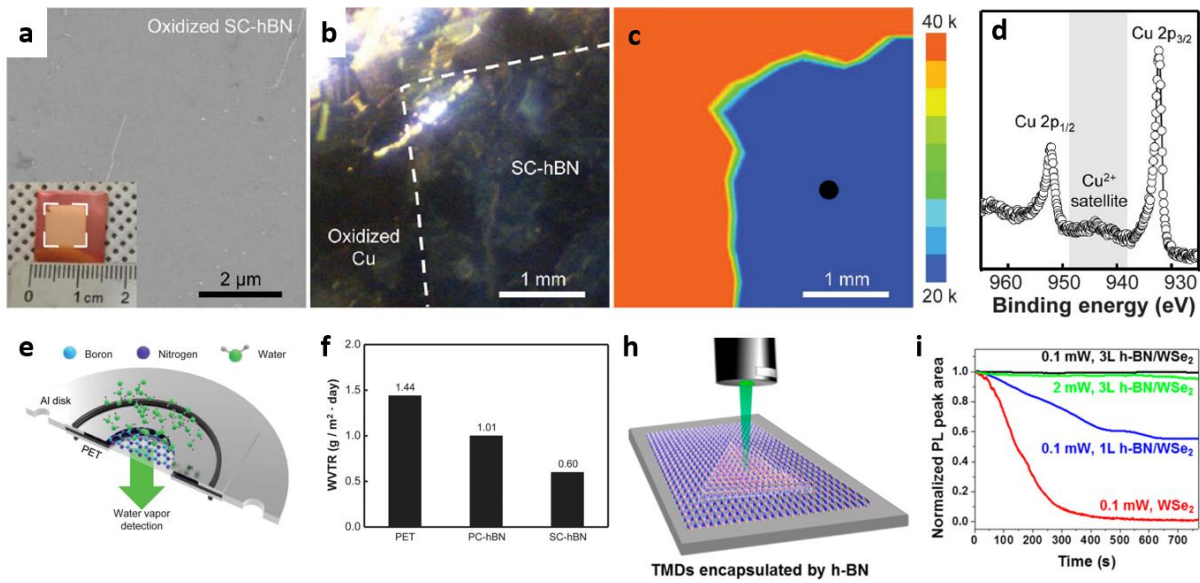


Figure 14. (a) SEM image of locally covered single-crystal hBN layer on Cu foil. Inset shows the corresponding photograph. (b) Optical image and corresponding XPS mapping of Cu foil covered with hBN and without hBN. (d) XPS Cu 2p spectrum after oxidizing Cu foil measured on hBN covered area in (c)¹⁵. (e) Schematic illustration for the WVTR measuring system. (f) Measured WVTR results of polycrystal and single-crystal monolayer hBN compare to bare PET. (h) Schematic illustration of laser irradiation process on monolayer TMDs passivated by trilayer hBN film. (i) Changes in areal intensity of PL peak for WSe₂, monolayer hBN/WSe₂, and trilayer hBN/WSe₂ in the presence of a water droplet¹³.

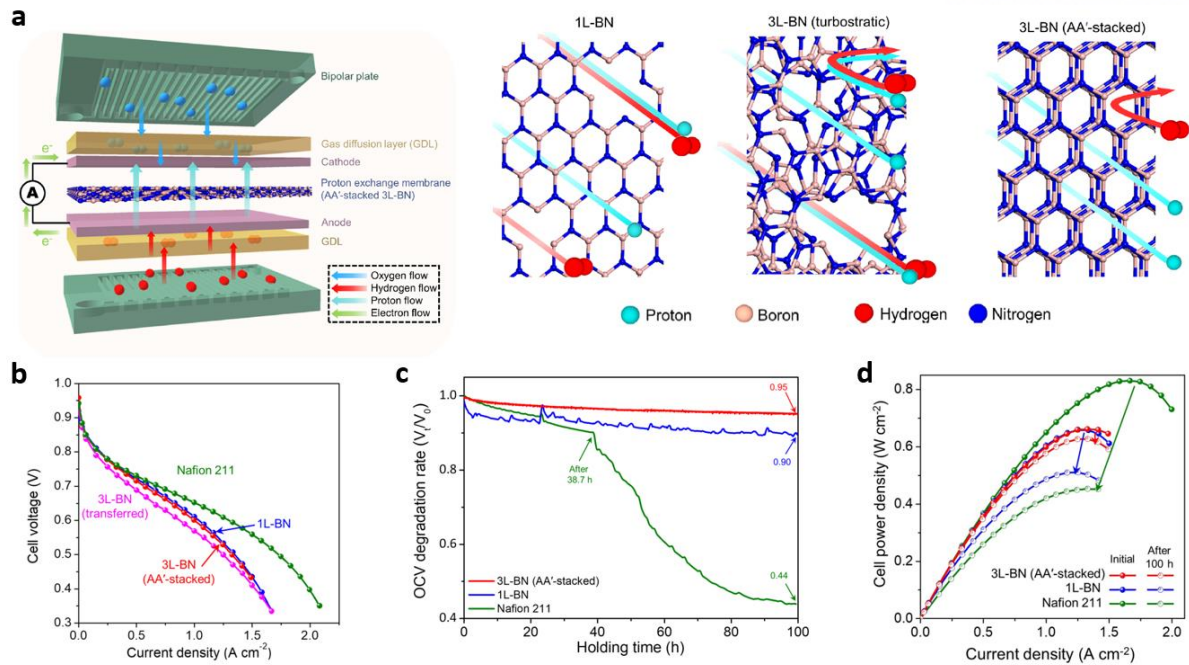


Figure 15. (a) Schematic illustration of PEMFC system consisted by AA'-stacked trilayer hBN for proton exchange membranes. Right figures illustrate behaviors of proton and hydrogen gas through monolayer, turbostratic trilayer, and AA'-stacked trilayer hBN. (b) Comparison of polarization curves of fuel cells with various type of hBN and Nafion 211. (c) Evolution of OCV over time in fuel cells utilizing AA'-stacked trilayer, monolayer hBN, and commercial Nafion 211 under harsh operating conditions. (d) Comparison of the power densities of fuel cells before and after operating under harsh conditions.

1.5 Outlook of hBN

The realization of future hBN-based practical applications may depend on the controllability and reproducibility in CVD systems. In terms of quality, single-crystal hBN film is highly required from mono- to multilayer thickness with scalable preparation. The layer-controllability of single-crystal hBN has remained critical issue. Recently, new approaches using multi-component alloys as a catalyst are developed to overcome limited controllability in single-component catalyst. The direct fabrication of high-quality 2D materials including a hBN film is also highly demanded. This approach can allow the direct fabrication of integrated device without additional process such as a transfer step. The development of PECVD method is one of the promising route for growth of high-quality hBN without using transition metal catalysts at relatively low temperature. While PECVD methods has been widely used for low-temperature growth of graphene, adopting growth of hBN and other 2D materials is still exploring. The final issue is the fabrications of all-CVD-derived 2D van der Waals heterostructures including graphene, hBN, and TMDs. To avoid contaminants and physical damage during handling, a one-step growth route should be developed. As a result, these developments will give a change to extending Moore's law of the number of transistors in a practical electronic device.

1.6 Reference

1. Li, M. Y.; Su, S. K.; Wong, H. S. P.; Li, L. J., How 2D semiconductors could extend Moore's law. *Nature* **2019**, *567* (7747), 169-170.
2. Watanabe, K.; Taniguchi, T.; Kanda, H., Direct-bandgap properties and evidence for ultraviolet lasing of hexagonal boron nitride single crystal. *Nat. Mater.* **2004**, *3* (6), 404-409.
3. Cassabois, G.; Valvin, P.; Gil, B., Hexagonal boron nitride is an indirect bandgap semiconductor. *Nat. Photonics* **2016**, *10* (4), 262-266.
4. Elias, C.; Valvin, P.; Pelini, T.; Summerfield, A.; Mellor, C. J.; Cheng, T. S.; Eaves, L.; Foxon, C. T.; Beton, P. H.; Novikov, S. V.; Gil, B.; Cassabois, G., Direct band-gap crossover in epitaxial monolayer boron nitride. *Nat. Commun.* **2019**, *10*, 2639.
5. Chen, J. H.; Jang, C.; Xiao, S. D.; Ishigami, M.; Fuhrer, M. S., Intrinsic and extrinsic performance limits of graphene devices on SiO₂. *Nat. Nanotechnol.* **2008**, *3* (4), 206-209.
6. Dean, C. R.; Young, A. F.; Meric, I.; Lee, C.; Wang, L.; Sorgenfrei, S.; Watanabe, K.; Taniguchi, T.; Kim, P.; Shepard, K. L.; Hone, J., Boron nitride substrates for high-quality graphene electronics. *Nat. Nanotechnol.* **2010**, *5* (10), 722-726.
7. Novoselov, K. S.; Mishchenko, A.; Carvalho, A.; Neto, A. H. C., 2D materials and van der Waals heterostructures. *Science* **2016**, *353* (6298), aac9439.
8. Geim, A. K.; Grigorieva, I. V., Van der Waals heterostructures. *Nature* **2013**, *499* (7459), 419-425.
9. Ferrari, A. C.; Bonaccorso, F.; Fal'ko, V.; Novoselov, K. S.; Roche, S.; Boggild, P.; Borini, S.; Koppens, F. H. L.; Palermo, V.; Pugno, N.; Garrido, J. A.; Sordan, R.; Bianco, A.; Ballerini, L.; Prato, M.; Lidorikis, E.; Kivioja, J.; Marinelli, C.; Ryhanen, T.; Morpurgo, A.; Coleman, J. N.; Nicolosi, V.; Colombo, L.; Fert, A.; Garcia-Hernandez, M.; Bachtold, A.; Schneider, G. F.; Guinea, F.; Dekker, C.; Barbone, M.; Sun, Z. P.; Galiotis, C.; Grigorenko, A. N.; Konstantatos, G.; Kis, A.; Katsnelson, M.; Vandersypen, L.; Loiseau, A.; Morandi, V.; Neumaier, D.; Treossi, E.; Pellegrini, V.; Polini, M.; Tredicucci, A.; Williams, G. M.; Hong, B. H.; Ahn, J. H.; Kim, J. M.; Zirath, H.; van Wees, B. J.; van der Zant, H.; Occhipinti, L.; Di Matteo, A.; Kinloch, I. A.; Seyller, T.; Quesnel, E.; Feng, X. L.; Teo, K.; Rupesinghe, N.; Hakonen, P.; Neil, S. R. T.; Tannock, Q.; Lofwander, T.; Kinaret, J.,

Science and technology roadmap for graphene, related two-dimensional crystals, and hybrid systems. *Nanoscale* **2015**, 7 (11), 4598-4810.

10. Tan, C. L.; Cao, X. H.; Wu, X. J.; He, Q. Y.; Yang, J.; Zhang, X.; Chen, J. Z.; Zhao, W.; Han, S. K.; Nam, G. H.; Sindoro, M.; Zhang, H., Recent Advances in Ultrathin Two-Dimensional Nanomaterials. *Chem. Rev.* **2017**, 117 (9), 6225-6331.

11. Sun, J. Y.; Lu, C.; Song, Y. Z.; Ji, Q. Q.; Song, X. J.; Li, Q. C.; Zhang, Y. F.; Zhang, L.; Kong, J.; Liu, Z. F., Recent progress in the tailored growth of two-dimensional hexagonal boron nitride via chemical vapour deposition. *Chem. Soc. Rev.* **2018**, 47 (12), 4242-4257.

12. Yoon, S. I.; Seo, D. J.; Kim, G.; Kim, M.; Jung, C. Y.; Yoon, Y. G.; Joo, S. H.; Kim, T. Y.; Shin, H. S., AA'-Stacked Trilayer Hexagonal Boron Nitride Membrane for Proton Exchange Membrane Fuel Cells. *ACS Nano* **2018**, 12 (11), 10764-10771.

13. Ahn, S.; Kim, G.; Nayak, P. K.; Yoon, S. I.; Lim, H.; Shin, H. J.; Shin, H. S., Prevention of Transition Metal Dichalcogenide Photodegradation by Encapsulation with h-BN Layers. *ACS Nano* **2016**, 10 (9), 8973-8979.

14. Liu, Z.; Gong, Y.; Zhou, W.; Ma, L.; Yu, J.; Idrobo, J. C.; Jung, J.; MacDonald, A. H.; Vajtai, R.; Lou, J.; Ajayan, P. M., Ultrathin high-temperature oxidation-resistant coatings of hexagonal boron nitride. *Nat. Commun.* **2013**, 4, 2541.

15. Lee, J. S.; Choi, S. H.; Yun, S. J.; Kim, Y. I.; Boandoh, S.; Park, J. H.; Shin, B. G.; Ko, H.; Lee, S. H.; Kim, Y. M.; Lee, Y. H.; Kim, K. K.; Kim, S. M., Wafer-scale single-crystal hexagonal boron nitride film via self-collimated grain formation. *Science* **2018**, 362 (6416), 817-821.

16. Pacile, D.; Meyer, J. C.; Girit, C. O.; Zettl, A., The two-dimensional phase of boron nitride: Few-atomic-layer sheets and suspended membranes. *Appl. Phys. Lett.* **2008**, 92 (13), 133107.

17. Gorbachev, R. V.; Riaz, I.; Nair, R. R.; Jalil, R.; Britnell, L.; Belle, B. D.; Hill, E. W.; Novoselov, K. S.; Watanabe, K.; Taniguchi, T.; Geim, A. K.; Blake, P., Hunting for Monolayer Boron Nitride: Optical and Raman Signatures. *Small* **2011**, 7 (4), 465-468.

18. Nicolosi, V.; Chhowalla, M.; Kanatzidis, M. G.; Strano, M. S.; Coleman, J. N., Liquid Exfoliation of Layered Materials. *Science* **2013**, 340 (6139), 1420.

19. Coleman, J. N.; Lotya, M.; O'Neill, A.; Bergin, S. D.; King, P. J.; Khan, U.; Young,

K.; Gaucher, A.; De, S.; Smith, R. J.; Shvets, I. V.; Arora, S. K.; Stanton, G.; Kim, H. Y.; Lee, K.; Kim, G. T.; Duesberg, G. S.; Hallam, T.; Boland, J. J.; Wang, J. J.; Donegan, J. F.; Grunlan, J. C.; Moriarty, G.; Shmeliov, A.; Nicholls, R. J.; Perkins, J. M.; Grieveson, E. M.; Theuwissen, K.; McComb, D. W.; Nellist, P. D.; Nicolosi, V., Two-Dimensional Nanosheets Produced by Liquid Exfoliation of Layered Materials. *Science* **2011**, *331* (6017), 568-571.

20. Zeng, Z. Y.; Sun, T.; Zhu, J. X.; Huang, X.; Yin, Z. Y.; Lu, G.; Fan, Z. X.; Yan, Q. Y.; Hng, H. H.; Zhang, H., An Effective Method for the Fabrication of Few-Layer-Thick Inorganic Nanosheets. *Angew. Chem. Int. Ed.* **2012**, *51* (36), 9052-9056.

21. Li, X. L.; Hao, X. P.; Zhao, M. W.; Wu, Y. Z.; Yang, J. X.; Tian, Y. P.; Qian, G. D., Exfoliation of Hexagonal Boron Nitride by Molten Hydroxides. *Adv. Mater.* **2013**, *25* (15), 2200-2204.

22. Zhou, K. G.; Mao, N. N.; Wang, H. X.; Peng, Y.; Zhang, H. L., A Mixed-Solvent Strategy for Efficient Exfoliation of Inorganic Graphene Analogues. *Angew. Chem. Int. Ed.* **2011**, *50* (46), 10839-10842.

23. Zhi, C. Y.; Bando, Y.; Tang, C. C.; Kuwahara, H.; Golberg, D., Large-Scale Fabrication of Boron Nitride Nanosheets and Their Utilization in Polymeric Composites with Improved Thermal and Mechanical Properties. *Adv. Mater.* **2009**, *21* (28), 2889-2893.

24. Ismach, A.; Chou, H.; Ferrer, D. A.; Wu, Y. P.; McDonnell, S.; Floresca, H. C.; Covacevich, A.; Pope, C.; Piner, R.; Kim, M. J.; Wallace, R. M.; Colombo, L.; Ruoff, R. S., Toward the Controlled Synthesis of Hexagonal Boron Nitride Films. *ACS Nano* **2012**, *6* (7), 6378-6385.

25. Shi, Y. M.; Hamsen, C.; Jia, X. T.; Kim, K. K.; Reina, A.; Hofmann, M.; Hsu, A. L.; Zhang, K.; Li, H. N.; Juang, Z. Y.; Dresselhaus, M. S.; Li, L. J.; Kong, J., Synthesis of Few-Layer Hexagonal Boron Nitride Thin Film by Chemical Vapor Deposition. *Nano Lett.* **2010**, *10* (10), 4134-4139.

26. Kim, S. M.; Hsu, A.; Park, M. H.; Chae, S. H.; Yun, S. J.; Lee, J. S.; Cho, D. H.; Fang, W. J.; Lee, C.; Palacios, T.; Dresselhaus, M.; Kim, K. K.; Lee, Y. H.; Kong, J., Synthesis of large-area multilayer hexagonal boron nitride for high material performance. *Nat. Commun.* **2015**, *6*, 8662.

27. Kim, G.; Jang, A. R.; Jeong, H. Y.; Lee, Z.; Kang, D. J.; Shin, H. S., Growth of High-Crystalline, Single-Layer Hexagonal Boron Nitride on Recyclable Platinum Foil. *Nano Lett.* **2013**, *13*

(4), 1834-1839.

28. Song, L.; Ci, L. J.; Lu, H.; Sorokin, P. B.; Jin, C. H.; Ni, J.; Kvashnin, A. G.; Kvashnin, D. G.; Lou, J.; Yakobson, B. I.; Ajayan, P. M., Large Scale Growth and Characterization of Atomic Hexagonal Boron Nitride Layers. *Nano Lett.* **2010**, *10* (8), 3209-3215.
29. Zhang, K.; Yap, F. L.; Li, K.; Ng, C. T.; Li, L. J.; Loh, K. P., Large Scale Graphene/Hexagonal Boron Nitride Heterostructure for Tunable Plasmonics. *Adv. Funct. Mater.* **2014**, *24* (6), 731-738.
30. Song, X. J.; Gao, J. F.; Nie, Y. F.; Gao, T.; Sun, J. Y.; Ma, D. L.; Li, Q. C.; Chen, Y. B.; Jin, C. H.; Bachmatiuk, A.; Ruemmel, M. H.; Ding, F.; Zhang, Y. F.; Liu, Z. F., Chemical vapor deposition growth of large-scale hexagonal boron nitride with controllable orientation. *Nano Res.* **2015**, *8* (10), 3164-3176.
31. Jang, A. R.; Hong, S.; Hyun, C.; Yoon, S. I.; Kim, G.; Jeong, H. Y.; Shin, T. J.; Park, S. O.; Wong, K.; Kwak, S. K.; Park, N.; Yu, K.; Choi, E.; Mishchenko, A.; Withers, F.; Novoselov, K. S.; Lim, H.; Shin, H. S., Wafer-Scale and Wrinkle-Free Epitaxial Growth of Single-Orientated Multilayer Hexagonal Boron Nitride on Sapphire. *Nano Lett.* **2016**, *16* (5), 3360-3366.
32. Caneva, S.; Weatherup, R. S.; Bayer, B. C.; Blume, R.; Cabrero-Vilatela, A.; Braeuninger-Weirner, P.; Martin, M. B.; Wang, R. Z.; Baetz, C.; Schloegl, R.; Meyer, J. C.; Hofmann, S., Controlling Catalyst Bulk Reservoir Effects for Monolayer Hexagonal Boron Nitride CVD. *Nano Lett.* **2016**, *16* (2), 1250-1261.
33. Uchida, Y.; Nakandakari, S.; Kawahara, K.; Yamasaki, S.; Mitsuhara, M.; Ago, H., Controlled Growth of Large-Area Uniform Multilayer Hexagonal Boron Nitride as an Effective 2D Substrate. *Acs Nano* **2018**, *12* (6), 6236-6244.
34. Kim, K. K.; Hsu, A.; Jia, X. T.; Kim, S. M.; Shi, Y. S.; Hofmann, M.; Nezich, D.; Rodriguez-Nieva, J. F.; Dresselhaus, M.; Palacios, T.; Kong, J., Synthesis of Monolayer Hexagonal Boron Nitride on Cu Foil Using Chemical Vapor Deposition. *Nano Lett.* **2012**, *12* (1), 161-166.
35. Lu, G. Y.; Wu, T. R.; Yuan, Q. H.; Wang, H. S.; Wang, H. M.; Ding, F.; Xie, X. M.; Jiang, M. H., Synthesis of large single-crystal hexagonal boron nitride grains on Cu-Ni alloy. *Nat. Commun.* **2015**, *6*, 6160.

36. Caneva, S.; Weatherup, R. S.; Bayer, B. C.; Brennan, B.; Spencer, S. J.; Mingard, K.; Cabrero-Vilatela, A.; Baehtz, C.; Pollard, A. J.; Hofmann, S., Nucleation Control for Large, Single Crystalline Domains of Mono layer Hexagonal Boron Nitride via Si-Doped Fe Catalysts. *Nano Lett.* **2015**, *15* (3), 1867-1875.
37. Okamoto, H.; ASM International., *Phase diagrams of binary iron alloys*. ASM International: Materials Park, OH, 1993; p 472 p.
38. Dudrova, E.; Selecka, M.; Bures, R.; Kabatova, M., Effect of boron addition on microstructure and properties of sintered Fe-1.5Mo powder materials. *Isij. Int.* **1997**, *37* (1), 59-64.
39. Cahn, R. W., ASM Handbook: Binary Alloy Phase Diagrams—Second edition (ASM International, 1990). **1990**.
40. H. Okamoto, T. B. M., “Au-B (Gold-Boron)” in Binary Alloy Phase Diagrams (ASM International, ed. 2, 1990), pp. 340–342. **1990**.
41. Wang, L.; Xu, X. Z.; Zhang, L. N.; Qiao, R. X.; Wu, M. H.; Wang, Z. C.; Zhang, S.; Liang, J.; Zhang, Z. H.; Zhang, Z. B.; Chen, W.; Xie, X. D.; Zong, J. Y.; Shan, Y. W.; Guo, Y.; Willinger, M.; Wu, H.; Li, Q. Y.; Wang, W. L.; Gao, P.; Wu, S. W.; Zhang, Y.; Jiang, Y.; Yu, D. P.; Wang, E. G.; Bai, X. D.; Wang, Z. J.; Ding, F.; Liu, K. H., Epitaxial growth of a 100-square-centimetre single-crystal hexagonal boron nitride monolayer on copper. *Nature* **2019**, *570* (7759), 91-95.
42. Li, J. D.; Li, Y.; Yin, J.; Ren, X. B.; Liu, X. F.; Jin, C. H.; Guo, W. L., Growth of Polar Hexagonal Boron Nitride Monolayer on Nonpolar Copper with Unique Orientation. *Small* **2016**, *12* (27), 3645-3650.
43. Chen, T. A.; Chuu, C. P.; Tseng, C. C.; Wen, C. K.; Wong, H. S. P.; Pan, S. Y.; Li, R. T.; Chao, T. A.; Chueh, W. C.; Zhang, Y. F.; Fu, Q.; Yakobson, B. I.; Chang, W. H.; Li, L. J., Wafer-scale single-crystal hexagonal boron nitride monolayers on Cu (111). *Nature* **2020**, *579* (7798), 219-223.
44. Lee, Y. H.; Liu, K. K.; Lu, A. Y.; Wu, C. Y.; Lin, C. T.; Zhang, W. J.; Su, C. Y.; Hsu, C. L.; Lin, T. W.; Wei, K. H.; Shi, Y. M.; Li, L. J., Growth selectivity of hexagonal-boron nitride layers on Ni with various crystal orientations. *RSC Adv.* **2012**, *2* (1), 111-115.
45. Kim, K.; Choi, J. Y.; Kim, T.; Cho, S. H.; Chung, H. J., A role for graphene in silicon-

based semiconductor devices. *Nature* **2011**, 479 (7373), 338-344.

46. Behura, S.; Nguyen, P.; Che, S. W.; Debbarma, R.; Berry, V., Large-Area, Transfer-Free, Oxide-Assisted Synthesis of Hexagonal Boron Nitride Films and Their Heterostructures with MoS₂ and WS₂. *J. Am. Chem. Soc.* **2015**, 137 (40), 13060-13065.

47. Shi, Z. Y.; Wang, X. J.; Li, Q. T.; Yang, P.; Lu, G. Y.; Jiang, R.; Wang, H. S.; Zhang, C.; Cong, C. X.; Liu, Z.; Wu, T. R.; Wang, H. M.; Yu, Q. K.; Xie, X. M., Vapor-liquid-solid growth of large-area multilayer hexagonal boron nitride on dielectric substrates. *Nat. Commun.* **2020**, 11, 849.

48. Gao, T.; Song, X. J.; Du, H. W.; Nie, Y. F.; Chen, Y. B.; Ji, Q. Q.; Sun, J. Y.; Yang, Y. L.; Zhang, Y. F.; Liu, Z. F., Temperature-triggered chemical switching growth of in-plane and vertically stacked graphene-boron nitride heterostructures. *Nat. Commun.* **2015**, 6, 6835.

49. Song, X. J.; Gan, T.; Nie, Y. F.; Zhuang, J. N.; Sun, J. Y.; Ma, D. L.; Shi, J. P.; Lin, Y. W.; Ding, F.; Zhang, Y. F.; Liu, Z. F., Seed-Assisted Growth of Single-Crystalline Patterned Graphene Domains on Hexagonal Boron Nitride by Chemical Vapor Deposition. *Nano Lett.* **2016**, 16 (10), 6109-6116.

50. Fu, L.; Sun, Y. Y.; Wu, N.; Mendes, R. G.; Chen, L. F.; Xu, Z.; Zhang, T.; Rummeli, M. H.; Rellinghaus, B.; Pohl, D.; Zhuang, L.; Fu, L., Direct Growth of MoS₂/h-BN Heterostructures via a Sulfide-Resistant Alloy. *ACS Nano* **2016**, 10 (2), 2063-2070.

51. Parzinger, E.; Miller, B.; Blaschke, B.; Garrido, J. A.; Ager, J. W.; Holleitner, A.; Wurstbauer, U., Photocatalytic Stability of Single- and Few-Layer MoS₂. *ACS Nano* **2015**, 9 (11), 11302-11309.

52. Ly, T. H.; Chiu, M. H.; Li, M. Y.; Zhao, J.; Perello, D. J.; Cichocka, M. O.; Oh, H. M.; Chae, S. H.; Jeong, H. Y.; Yao, F.; Li, L. J.; Lee, Y. H., Observing Grain Boundaries in CVD-Grown Mono layer Transition Metal Dichalcogenides. *ACS Nano* **2014**, 8 (11), 11401-11408.

53. Gao, J.; Li, B. C.; Tan, J. W.; Chow, P.; Lu, T. M.; Koratkar, N., Aging of Transition Metal Dichalcogenide Monolayers. *ACS Nano* **2016**, 10 (2), 2628-2635.

Chapter 2: Epitaxial Growth of Single-Crystal Few-Layer Hexagonal Boron Nitride on Ni (111)

2.1 Abstract

Atomically flat hexagonal boron nitride (hBN) as an insulator and dielectric is necessary for two-dimensional (2D) devices offering great potential for further increasing the density of transistors in an integrated circuit¹. In particular, single-crystal hBN is required because defects and grain boundaries can be charge trap or charge scattering sites². While large-area single-crystal hBN monolayers on metal substrates have been recently demonstrated³⁻⁵, few- or multi-layer single-crystal hBN which is more desirable for 2D devices is so far unknown. Here we report the epitaxial growth of single-crystal tri-layer hBN on Ni (111) foil of 2 cm × 5 cm at 100 °C higher temperature than normal growth temperature for Ni substrate. The tri-layer hBN grains show unidirectional alignment and seamless stitching to form single-crystal film on Ni₂₃B₆/Ni (111) where a Ni₂₃B₆ layer is formed between hBN and Ni (111) during cooling. Microscopic investigations reveal epitaxial relationship between hBN, Ni₂₃B₆, and Ni (111) and enable to understand the hBN growth mechanism through the surface-mediated growth. Furthermore, single-crystal tri-layer hBN on Ni₂₃B₆/Ni (111) plays roles of a catalytic-transparent protection layer for enhanced long-term stability of hydrogen evolution reaction catalyst and a dielectric layer to prevent electron doping from SiO₂ substrate in MoS₂ transistor. Our results suggest that few-layer single-crystal hBN allows wide applications for 2D devices and catalytic-transparent protection layer of (electro)catalysts.

2.2 Introduction

Insulating hBN layers can be used for a protection layer (preventing oxidation of metal like Cu)^{3, 6}, a dielectric in 2D devices (screening charge trap sites of the substrate to prevent the charge scattering)², and an interface layer for future 2D heterostructures (electronics and photonics). While single-crystal hBN is desirable for such applications, a key challenge is the growth of single-crystal hBN in large area. Recent studies have demonstrated the growth of wafer-scale single-crystal hBN monolayer on liquid

Au and single-crystal Cu surfaces by chemical vapor deposition (CVD) method³⁻⁵. However, the monolayer hBN is not enough to efficiently reduce the influences from underlying substrates or disturbances from surroundings due to its single-atom thickness^{7, 8}. Accordingly, few- or multi-layer hBN is highly required. To date, several strategies to directly grow high-quality yet polycrystalline few-layer or multi-layer hBN by CVD methods have been developed using Fe, Ni, Pt, Cu, and Ni-Fe alloy as catalytic substrates⁶⁻¹⁴ as well as non-catalytic substrates¹⁵⁻¹⁷. However, growth of single-crystal few-layer hBN in large area is unknown. Here, we report a large-area single-crystal tri-layer hBN film on Ni₂₃B₆/Ni (111) and its usefulness.

2.3 Experimental Section

2.3.1 Preparation of single-crystal Ni (111) foil

Large-area Ni (111) foil (Figure 1) was prepared by contact-free annealing method²¹. A suspended commercial polycrystalline Ni foil (100 μm thick, 99.994%; Alfa Aesar) was heated to 1,350 $^{\circ}\text{C}$, and held at that temperature for 24 h under a mixed-gas flow (Ar, 30 sccm, H₂, 30 sccm; sccm, standard cubic centimeter per minutes) at a pressure of 760 torr.

2.3.2 Growth of single-crystal trilayer hBN on Ni (111)

The Ni (111) foil was placed inside the high-temperature and low-pressure CVD system (Figure 2a) at the centre of a furnace. A borazine (purchased from Gelest, Inc.) precursor flask was placed in a water bath at -15 $^{\circ}\text{C}$. The bath temperature before the growth of hBN was ramped up to 25 $^{\circ}\text{C}$. Before growth, the Ni (111) foil was heated to the growth temperature (1,220 $^{\circ}\text{C}$) under a mixed-gas flow (Ar, 10 sccm; H₂, 10 sccm). The flow of borazine gas at 0.1 sccm (controlled by a mass flow controller) was then introduced into the CVD chamber for 60 min in order to grow hBN. After hBN growth, the borazine flow was terminated and the furnace was cooled rapidly to room temperature under a mixed-gas flow (Ar, 10 sccm, H₂, 10 sccm). The control experiments were performed at various growth temperature from 1020 to 1320 $^{\circ}\text{C}$.

2.3.3 Transfer of hBN film onto arbitrary substrates

The as-grown hBN was transferred to SiO₂/Si wafer, quartz plate, and 5-nm-thick amorphous SiN windows (TEMwindows.com) by the polymer-mediated wet transfer process for further characterizations. A poly(methyl methacrylate) (PMMA) film was spin-coated on the as-grown hBN/Ni₂₃B₆/Ni as a protection layer. Then Ni₂₃B₆/Ni was etched away in the aqueous solution of iron chloride (FeCl₃). After thorough washing, the hBN film was transferred onto a target substrate, and finally PMMA was removed by dipping in acetone.

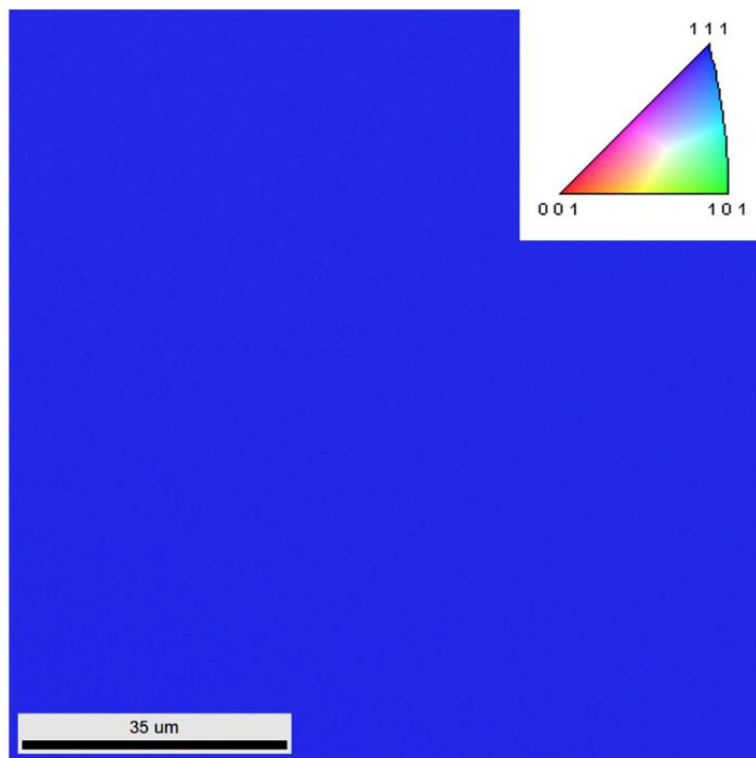


Figure 1. Electron backscatter diffraction (EBSD) IPF mapping of Ni (111) surface.

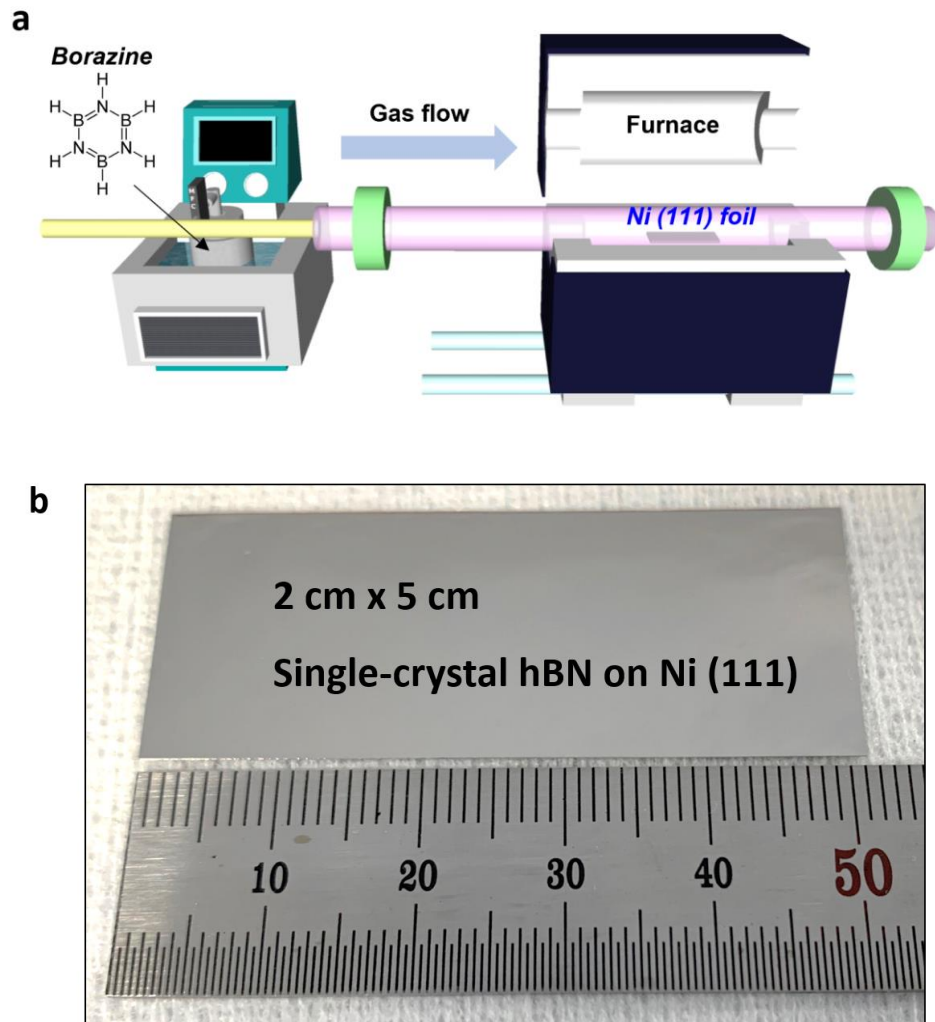


Figure 2. (a) Schematic diagrams of high-temperature and low-pressure CVD for the growth of hBN. (b) Photograph of a centimeter-sized as-grown single-crystal trilayer hBN film on Ni (111).

2.3.4 Characterizations

The prepared Ni (111) foil was characterized by SEM (Verios 460, FEI) and electron backscatter diffraction (Hikari from Ametek). The surface morphology of hBN was characterized by optical microscopy (Axio Scope. A1, Carl Zeiss), SEM (Verios 460, FEI), and AFM (Dimension Icon, Bruker). XPS (ESCALAB 250 Xi, Thermo Scientific) was performed to determine chemical compositions. Raman spectrum was obtained using a micro Raman spectrometer (alpha 300, WITec GmbH) with a laser excitation wavelength of 532 nm and about 2 mW power. The UV-vis adsorption spectrum (Cary 5000 UV-vis-NIR, Agilent) was measured to estimate the optical band gap of hBN on the quartz substrate. The optical band gap energy was determined by using the formula of a direct band gap semiconductor: $\alpha = C(E - E_g)^{1/2}/E$ (where α is the absorption coefficient, C is a constant, E is the photon energy, and E_g is the optical bandgap energy). The plot of $(\alpha E)^2$ vs. E should be a straight line. Therefore, when $(\alpha E)^2 = 0$, E should be equal to E_g . For atomic-resolution imaging and SAED measurements, low-voltage Cs aberration-corrected TEM (Titan Cube G2 60-300, FEI) was performed at 80 kV using a monochromatic electron beam. To evaluate the lattice orientations of hBN film, SAED patterns in TEM (JEM-2100F, JEOL) on 5-nm-thick amorphous SiN windows and POM (Eclipse LV100-POL equipped with a heating stage, Nikon) on SiO₂/Si wafer after LC (4-cyano-4'-pentylbiphenyl (5CB), Alfa Aesar) coating were employed.

2.3.5 H₂ plasma etching

To evaluate the electrocatalytic performance of Ni₁₂₃B₆ without hBN protecting layer, as-grown sample was exposure to 50 W of H₂ plasma using a 13.56 MHz radio frequency plasma generator (Diener Femto, Diener Electronic) for 5 min. The sample was kept 10 cm away from the discharge zone. The plasma treatment was performed at 25 °C with a H₂ gas flow (5 sccm). The operating pressure was maintained at 1 mbar during plasma exposure. It is also noted that no potential was applied to the aluminum stage on which the sample was placed.

2.3.6 Electrochemical measurements

Electrochemical measurements were performed in a three-electrode cell using a ZIVE SP2 (ZIVE LAB). The polarization curves were collected by linear sweep voltammetry with a scan rate of 5 mV s⁻¹ in 0.5 M H₂SO₄ electrolyte. A square shaped metal foil electrode of geometric area 1 x 1 cm² was used

as the working electrode. The working electrode was equipped in the customized holder for measurements. Ag/AgCl and graphite rod were used as the reference electrode and counter electrode, respectively. During the electrochemical measurements, high-purity N₂ gas was continually bubbled throughout the whole electrochemical measurement. Potentials versus RHE can be calculated compared with Ag/AgCl electrode by adding a value of 0.215 V after calibration. The electrochemical stabilities of the catalysts were evaluated by continuously cycling the catalyst for 2,000 times at a scan rate of 5 mV s⁻¹.

2.3.7 DFT calculation

All calculations are carried out by Vienna Ab Initio Simulation Package (VASP) with the projector augmented wave (PAW) method. The exchange–correlation functions are treated by the Perdew-Burke-Ernzerhof (PBE) generalized gradient approximation (GGA), and the long-range vdW interactions are included through DFT-D3 correction. In building the hBN/Ni(111) models, the original hBN lattice is remained whereas Ni lattice are changed within ~3%. Periodic boundary condition is adopted in the in-plane direction of substrate surface, and a ~15 Å vacuum layer is induced in the out-plane direction to avoid imaging coupling. A plan-wave *energy cutoff is set to be 400 eV*, and the force on each atom less than 0.01 eV Å⁻¹ and the energy convergence less than 10⁻⁴ eV are set as criteria for the self-consistent calculations. The definition of binding energy between hBN layer and the Ni (111) substrate:

$$E_B = \frac{E_{hBN} + E_{Sub} - E_{Total}}{N_{unit}}$$

where E_{hBN} and E_{Sub} are the energies of free-standing hBN layer and Ni (111) substrate, E_{Total} is total energy of a model of a hBN layer on the Ni (111) substrate, and N_{unit} is the number of hBN unit in the model.

2.4 Results and Discussion

2.4.1 Growth procedure and mechanism of trilayer hBN on Ni (111)

A single-crystal Ni (111) foil was prepared from polycrystalline Ni foil by annealing for a long time in a mixed hydrogen and argon atmosphere (Figure 1). We obtained large-scale single-crystal tri-layer hBN film on Ni (111) using a borazine flow rate of 0.1 sccm for 60 min at 1220 °C. (Figure 2 and 3,

and the experimental details are given in **Section 2.3.2**). The time evolution of tri-layer hBN growth is displayed in **Figure 4a**. At the initial growth stage (~30 min), the unidirectionally aligned tri-layer hBN grains are observed on the Ni (111) surface (**Figure 4a, step ii** and **Figure 5**). The high-magnification scanning electron microscopy (SEM) image of a hBN grain shows that one edge of the hBN grain is parallel to the surface steps (**inset of Figure 4a, step ii**). This phenomenon corresponds to the recently suggested the edge-docking of hBN grains at the vicinal step edges on the Cu (111) and (110) surface, leading the single-crystal hBN monolayer^{4, 5}. After the growth for 45 min (**Figure 4a, step iii**), hBN grains grow and merge to larger ones. When two hBN grains merge, they are stitched to continuous large grain along surface steps. It is noted that the thickness of hBN did not change during the coalescence of hBN grains at 45 min (**Figure 6**). The fully covered hBN is observed at the growth time of 60 min (**Figure 4a, step iv**). The as-transferred hBN exhibits a uniform contrast, indicating a macroscopic uniformity in their thickness (**Figure 4b**). Atomic force microscopy (AFM) exhibit the thickness of 1.2 nm and uniformity of tri-layer hBN film (**Figure 4c**). The Raman spectrum of a tri-layer hBN film transferred on SiO₂ (300 nm)/Si substrate exhibits the characteristic peak at 1368 cm⁻¹ and the full width at half maximum (FWHM) of 14.3 cm⁻¹ (**Figure 4d**) which is narrower than that (17 cm⁻¹) of the multilayer hBN grown on Ni-Fe alloy⁸. Ultraviolet-visible (UV-Vis) absorption spectroscopy shows the optical bandgap energy of 6.05 eV (**Figure 4e**), which is in agreement with previous report¹⁰. The X-ray photoelectron spectroscopy (XPS) data reveals sp²-bybridized B and N elements in the hBN film and the formation of a Ni-B bond (**Figure 7**). The B 1s spectrum is deconvoluted into two distinct peaks at 190.2 and 187.9 eV. The latter can be assigned to B-Ni bond of nickel boride alloys¹⁸⁻²⁰. The B/N atomic ratio in the hBN is 1:0.96, which is calculated from 190.2 eV and 397.9 eV in B 1s and N 1s spectra, respectively.

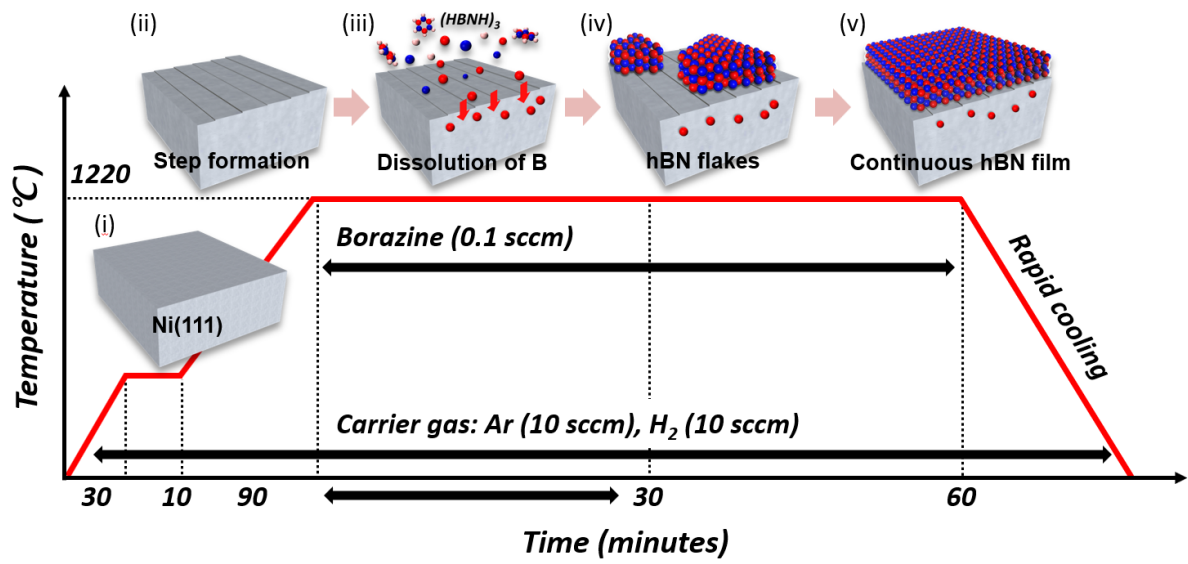


Figure 3. Schematic illustration of procedure of hBN growth on Ni(111).

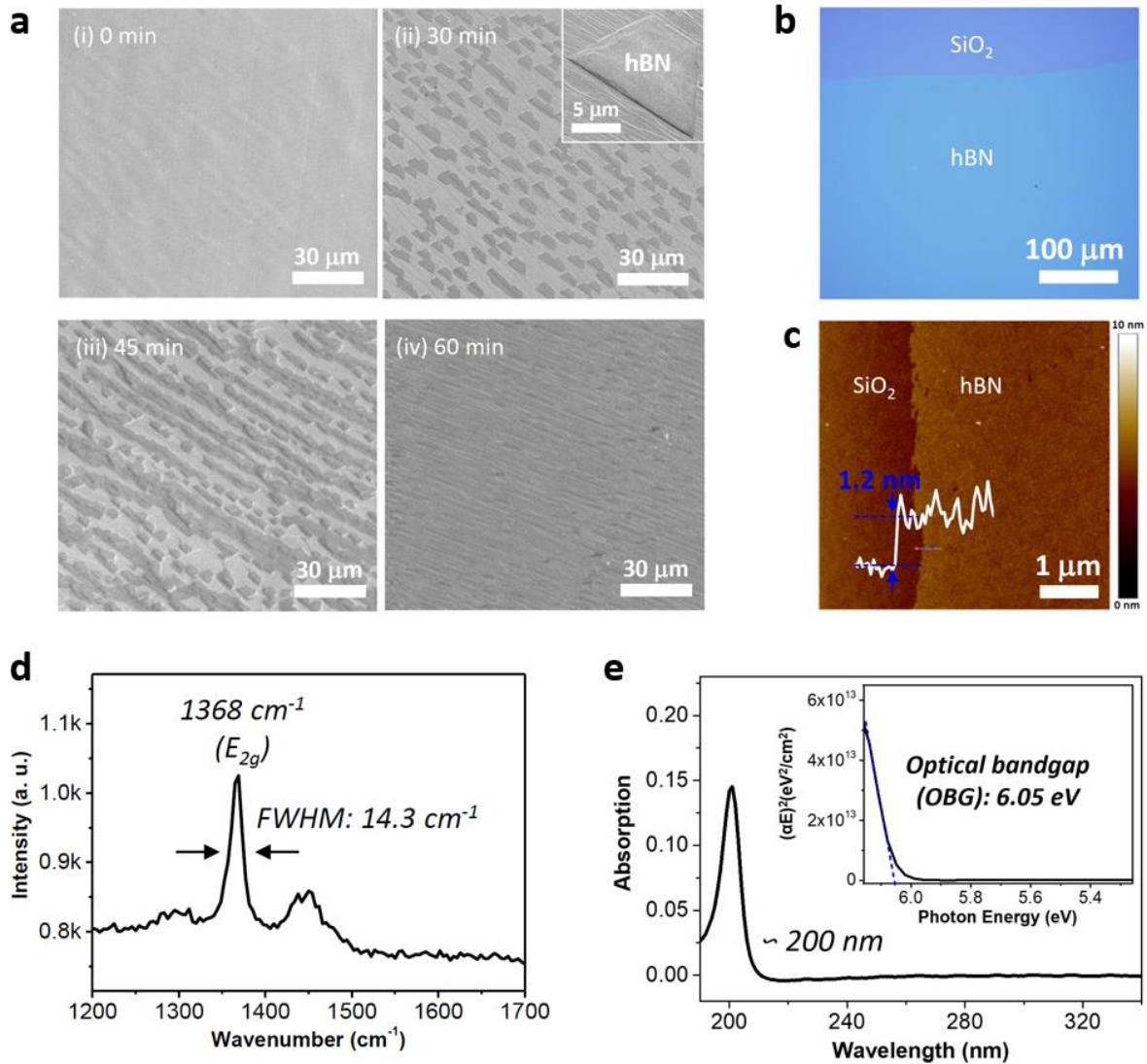


Figure 4. Growth of single-crystal trilayer hBN on Ni (111). (a) SEM images showing the time evolution of trilayer hBN on a Ni (111) at 1220 °C. (Inset of step ii) The high-magnification SEM image of a hBN grain, showing that one edge of the hBN grain is parallel to the surface steps. (b) OM and (c) AFM images of an edge hBN film transferred on the SiO₂/Si. The inset of (c) shows the corresponding AFM height profile of a trilayer hBN film. (d) Raman spectrum of a trilayer hBN film on SiO₂/Si, showing the characteristic hBN signal at 1370 cm⁻¹. (e) UV-Vis absorption spectrum of trilayer hBN transferred to quartz substrate. The inset is optical bandgap analysis of (e).

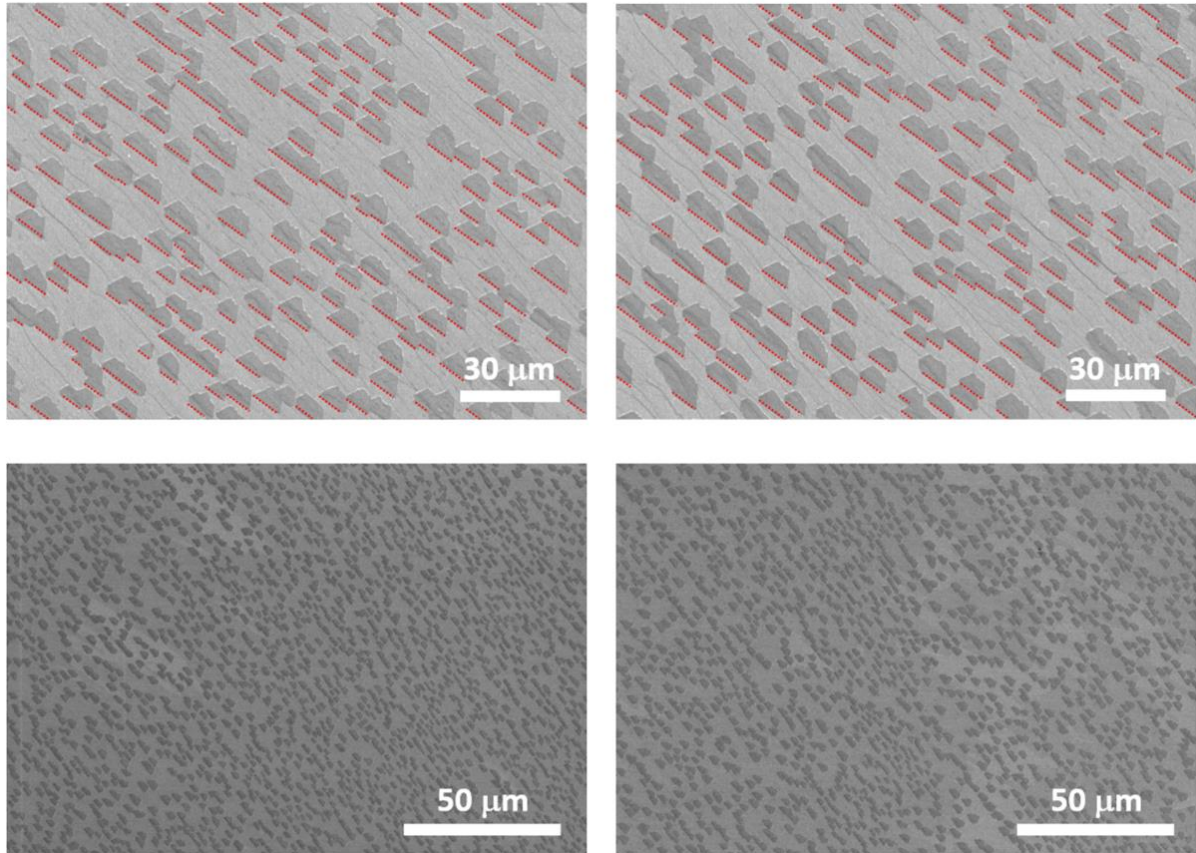


Figure 5. Large-area SEM images of as-grown unidirectionally aligned hBN grains on Ni (111) substrate after growth for 30 min.

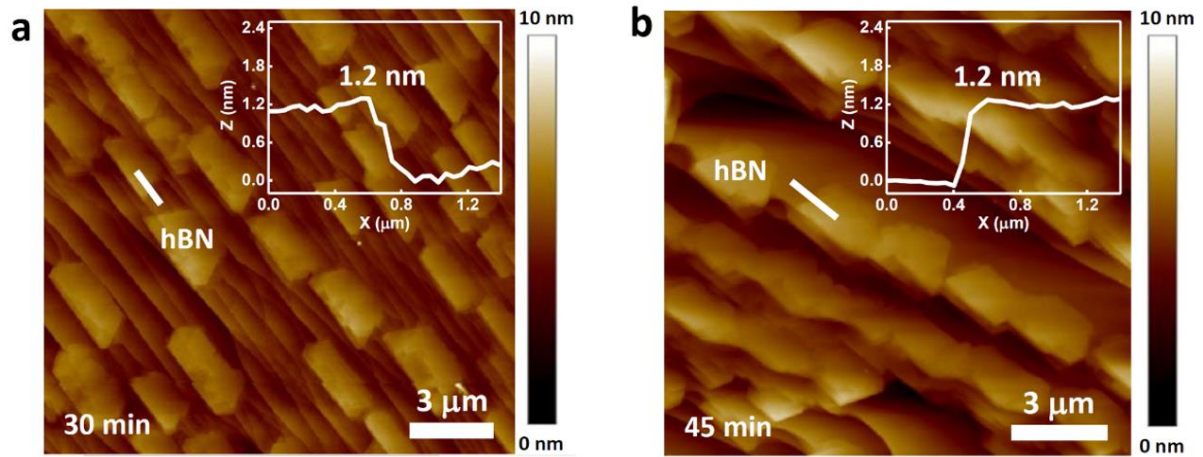


Figure 6. AFM images at the growth time for (a) 30 and (b) 45 min. The insets in (a) and (b) show height measurements taken at the position of the white lines.

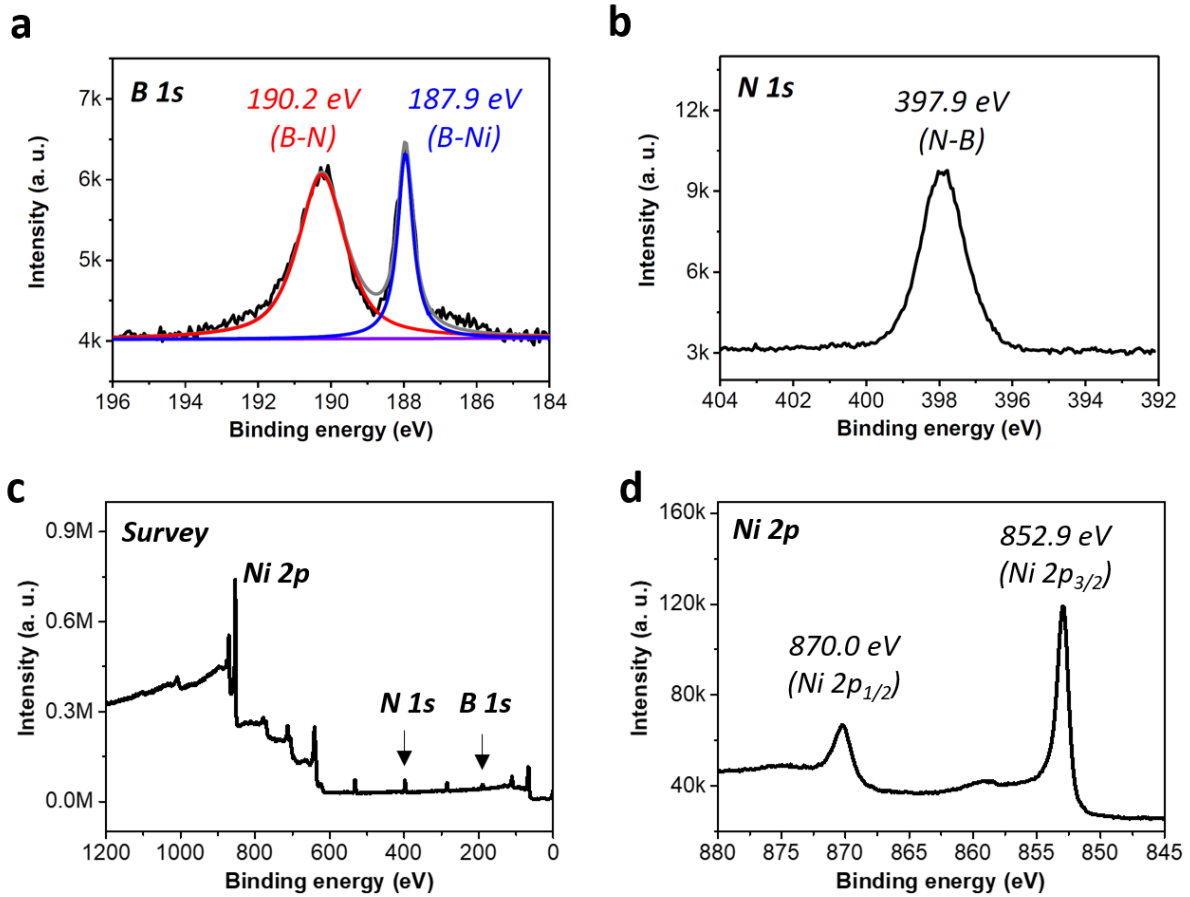


Figure 7. (a-d) XPS spectra measured from an as-grown trilayer hBN film on Ni (111). The binding energies of the B 1s orbital at 190.2 eV and 189.9 eV confirm the formations of hBN (with N 1s at 379.9 eV) and Ni-B.

Figure 8 exhibits schematic illustration for proposed growth mechanism comprising five steps. The dissociation of borazine as a precursor supplies B and N species to the Ni surface at high temperature (Figure 8, step i). Based on the ternary Ni-B-N phase diagram, the incorporation of B into the Ni catalyst as a solid solution is expected due to the high solubility (~0.3 at % at 1085 °C)²¹ (Figure 8, step ii). However, N shows the extremely low solubility in the Ni catalyst (~0.004 at % at 1550 °C)²². Thus, neither formation of Ni-nitride nor dissolution of N are considered. The hBN grains grow along the surface step edges (Figure 8, step iii). The growth mechanism of hBN is supposed to be surface-mediated growth because the hBN thickness did not change at different cooling rates of -60, -30, and -5 °C/min (Figure 4c for -60 °C/min and AFM images in Figure 9 for -30 and -5 °C/min). It is noted that the precipitation-based growth shows increase in thickness as the cooling rate decreases⁷. The hBN grains coalesces into the continuous hBN film after 60 min (Figure 8, step iv and v). After cooling down, energy-filtered transmission electron microscopic (EF-TEM) analysis displays the uptake of B atoms into the Ni catalyst underneath hBN (Figure 10). Actually, the formation of Ni₂₃B₆ alloy (structure information will be discussed later) is observed between hBN and Ni substrate (Figure 8, step vi and Figure 11). The thickness of the Ni₂₃B₆ layer decreases as the cooling rates decreases (Figure 11a-c). This indicates that the Ni₂₃B₆ alloy is formed during the cooling step after the growth of hBN at high temperature, which is in good agreement with the previous studies demonstrating that the Ni₂₃B₆ alloy can be formed by undercooling process^{23, 24}. Simultaneously, we suggest that while the incubated B atoms beneath hBN layer convert to the Ni₂₃B₆ alloy during cooling process, the B atoms uncovered by hBN are escaped to the gas phase in the form of BH_x (Figure 11d). The cross-section TEM measurements show the formation of Ni₂₃B₆ alloy only beneath hBN layer at every stage, indicating that any Ni₂₃B₆ is not found without the hBN film cover (Figure 12).

To understand the effects of the growth temperature and the formation of Ni₂₃B₆ alloy, we carried out the growth at 1020 to 1320 °C for same growth time, 30 min (Figure 13). At 1020 °C, the relatively thick hBN film (~3.5 nm) is grown, indicating the typical precipitation mechanism on Ni, which is consistent with previous report¹⁰. The growth of tri-layer hBN by surface-mediated reaction started from 1120 °C. The average sizes of hBN grains grown at 1120 and 1170 °C are 700 nm and 2 μm, respectively, while the size at 1220 °C is 10 μm (Figure 13b-d). These results imply that the growth temperature play a crucial role for initial grain size of hBN. However, the surface morphologies of hBN are no longer smooth and uniform at 1270 °C. Moreover, the local melting and aggregation of Ni surface are shown at 1320 °C close to melting temperature of Ni (Figure 13e-f). Thus, we suppose that the surface-mediated growth on Ni (111) requires higher temperature than conventional growth temperature (approximately 1000 °C) using Ni catalyst^{6, 10, 11}.

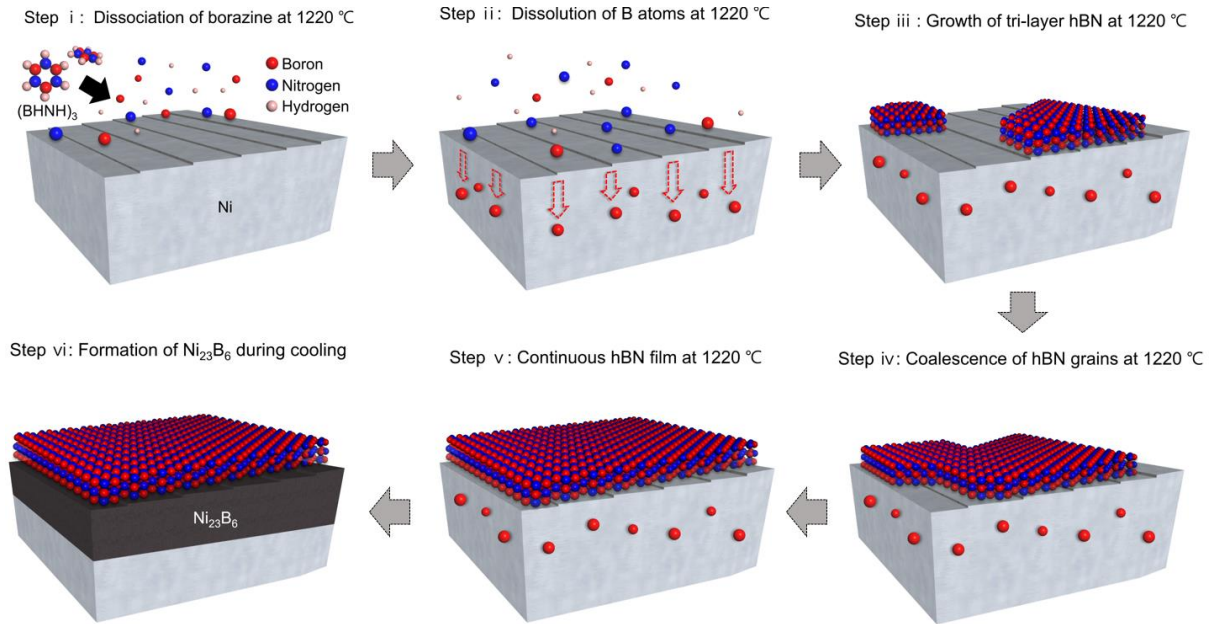


Figure 8. Schematic illustration of the growth procedure for hBN growth on Ni (111).

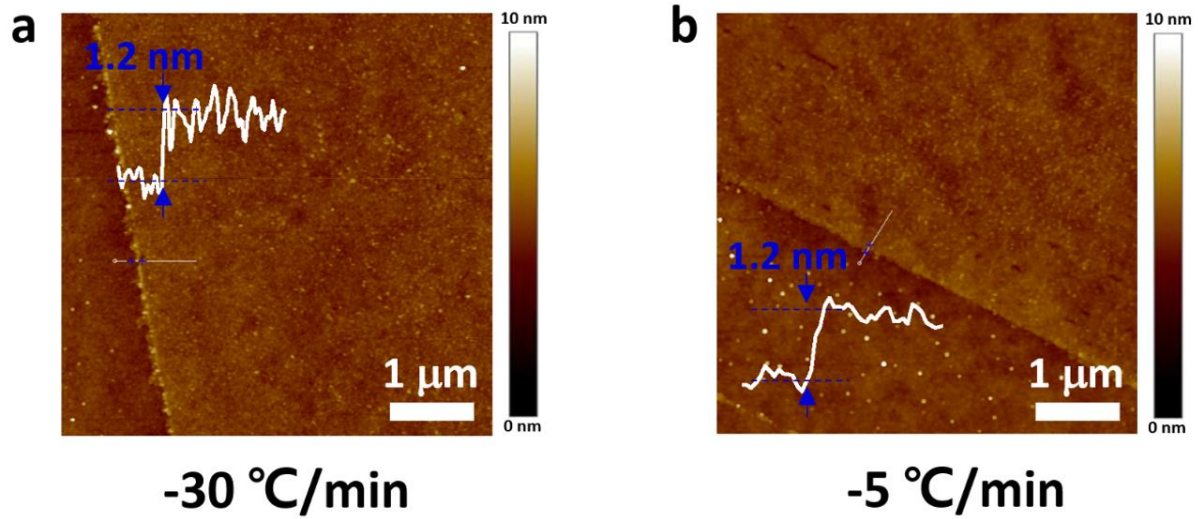


Figure. 9 AFM images of cooling rates of (a) -30 and (b) -5 °C /min from 1220 to 620 °C hBN cooling rates of, respectively.

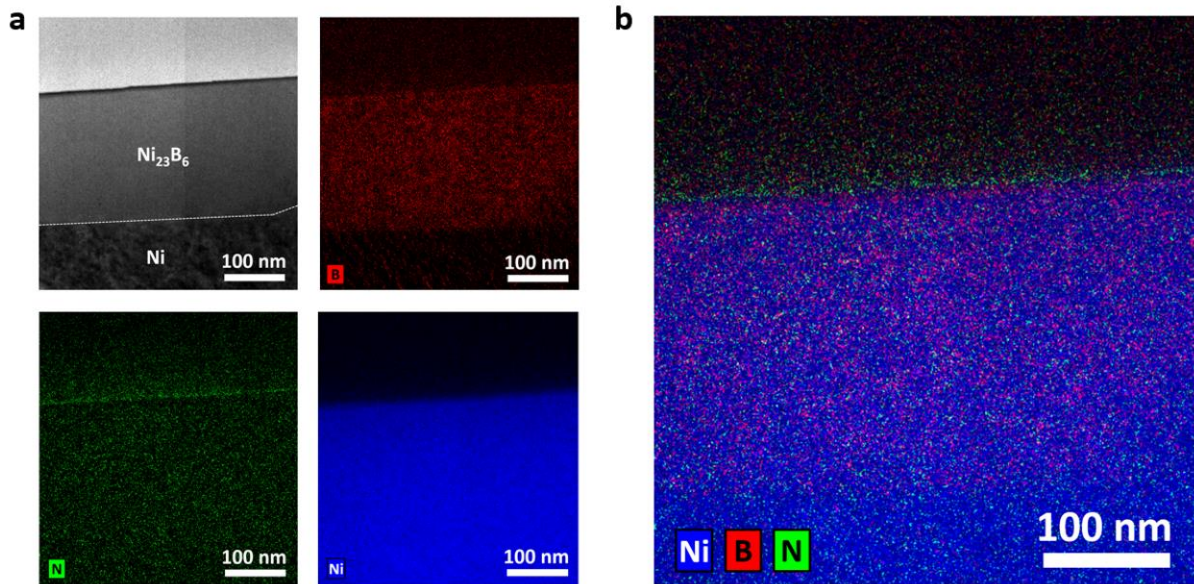


Figure 10. Energy filtered TEM (EF-TEM) mapping of hBN/ Ni_{23}B_6 /Ni. (a) Cross-sectional HR-TEM image (left upper) and EF-TEM maps of boron (red), nitrogen (green), and nickel (blue). (b) An image of overlaid EF-TEM maps for all elements.

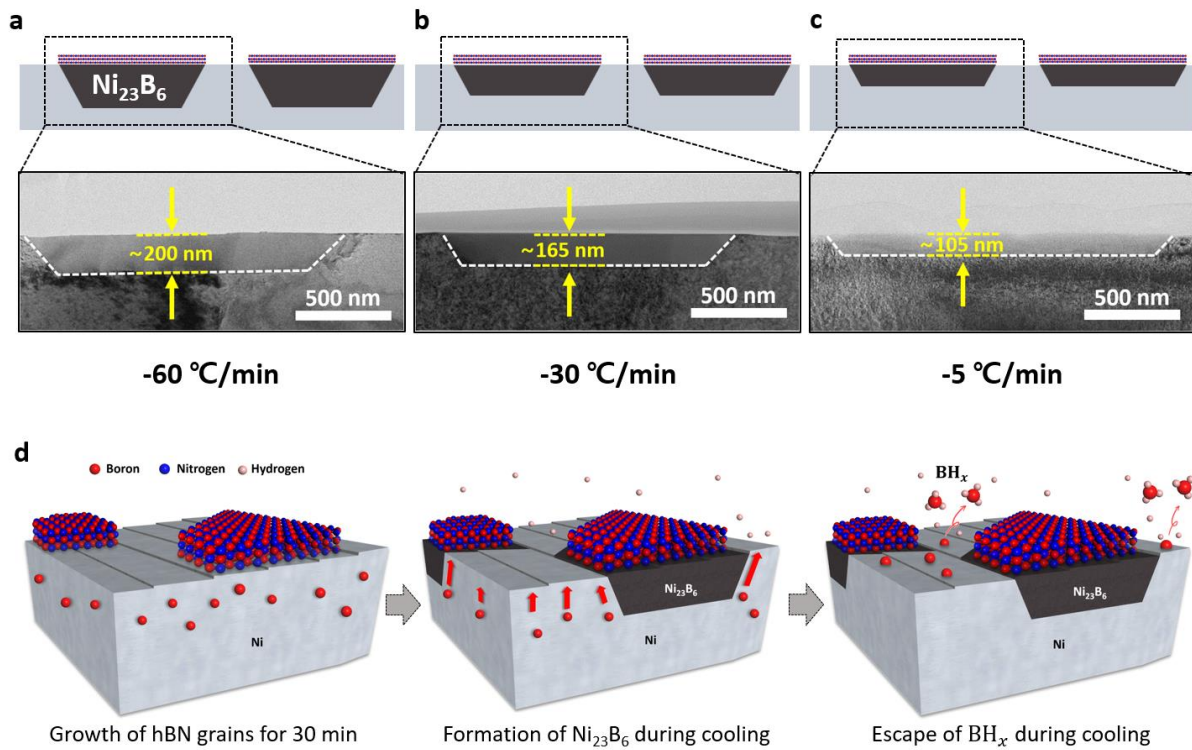


Figure 11. The effect of cooling rate. Cross-sectional TEM images of as-formed Ni_{23}B_6 alloy for the cooling rates of (a) -60 , (b) -30 , and (c) $-5\text{ }^\circ\text{C}/\text{min}$ from 1220 to $620\text{ }^\circ\text{C}$, respectively. (d) Proposed mechanism for escape of B atoms during cooling.

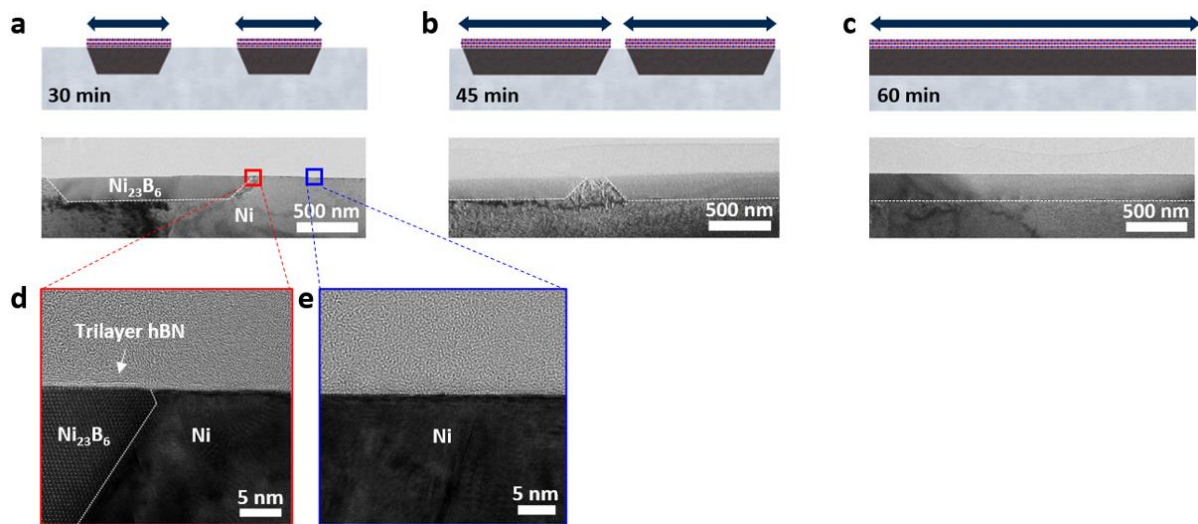


Figure 12. Initial stage of hBN/ Ni_{23}B_6 on Ni(111). (a-c) schematic diagrams (upper panels) and cross-sectional TEM images (lower panels) at the different growth time for (a) 30, (b) 45, and (c) 60 min at 1220 °C. (d) Cross-section TEM image of Ni surface after growth for 30 min. (e-f) AFM images at the growth time for (e) 30 and (f) 45 min. The insets in (e and f) show height measurements taken at the position of the white lines.

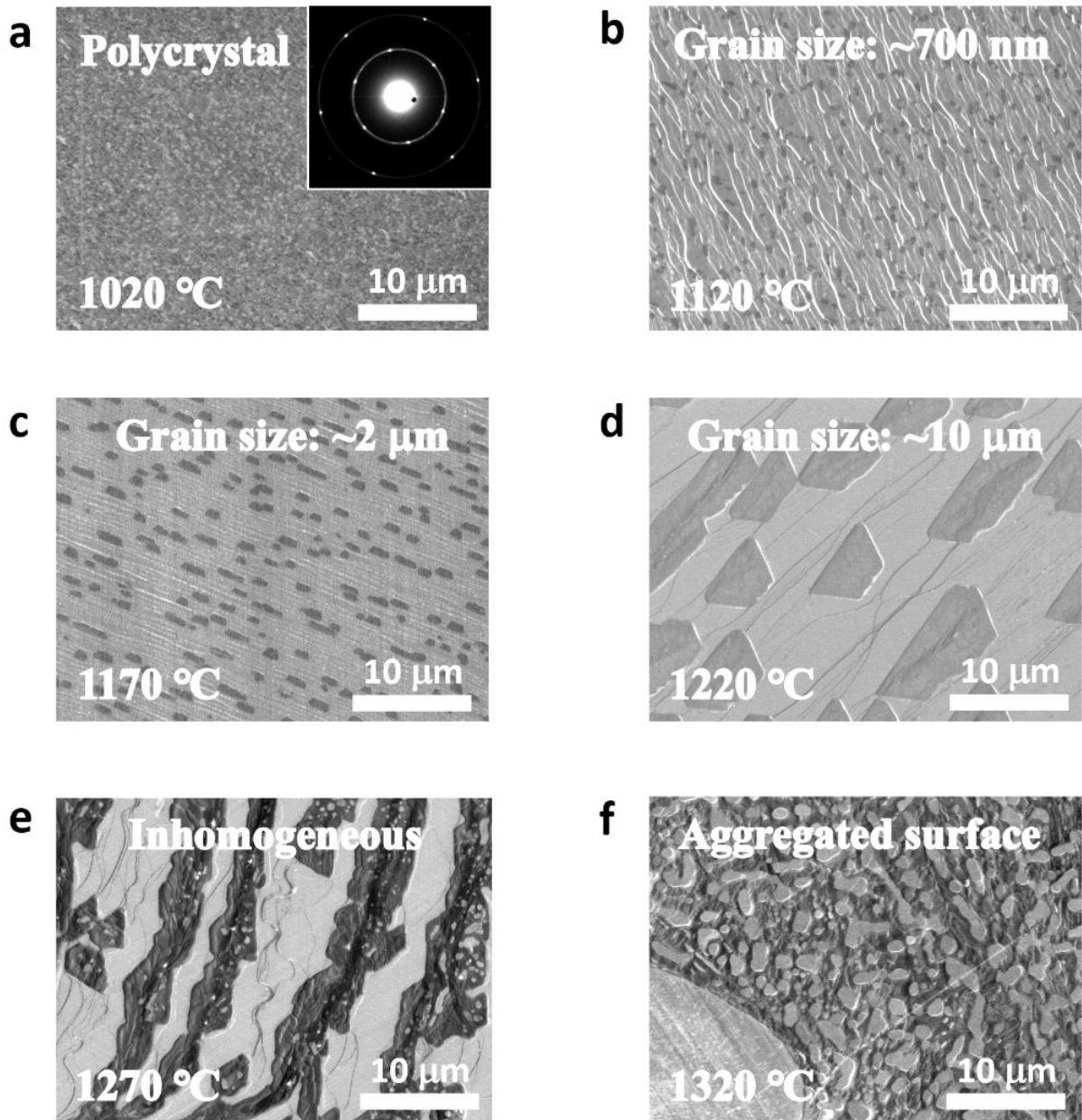


Figure 13. SEM images of hBN grown on Ni (111) for 30 min at (a) 1020 °C, (b) 1120°C, (c) 1170 °C, (d) 1220 °C, (e) 1270, and (f) 1320 °C. The inset of (a) reveals SAED pattern of hBN film grown at 1020 °C.

2.4.2 Structure characterizations of hBN/Ni₂₃B₆/Ni(111)

In order to confirm the crystal structure and epitaxial relationship between the tri-layer hBN, Ni₂₃B₆, and Ni (111), we performed the cross-sectional high-resolution TEM measurements. The cross-sectional sample was prepared by the focused ion beam (FIB) technique. Figure 14a and b show the low- and high-magnification TEM image of the 200 nm-thickness Ni₂₃B₆ on the Ni (111) surface over a large area and a distinct interface between Ni₂₃B₆ and Ni regions. It is clearly confirmed that the atomic structure of Ni₂₃B₆, which is face-centered cubic (FCC) structure (space group $Fm\bar{3}m$) with a lattice constant of $a = 10.76 \text{ \AA}$ (Figure 14c) corresponds to the simulation result (Figure 14d). The selected-area electron diffraction (SAED) pattern indicates identical hexagonal dots of Ni₂₃B₆ and Ni (Figure 14e), ensuring that the alignment of the Ni₂₃B₆ on Ni is $[111] \text{ Ni}_{23}\text{B}_6 \parallel [111] \text{ Ni}$ and $[002] \text{ Ni}_{23}\text{B}_6 \parallel [002] \text{ Ni}$ in a selected area of $\sim 500 \text{ nm}$ by 500 nm . Figure 14f and g display uniformity of tri-layer hBN film, which is consistent with the AFM height profile (Figure 4c) and well-defined layered structure with an interlayer distance of 0.33 nm (yellow dashes). According to the corresponding the fast Fourier transform patterns of the as-grown hBN (Figure 14h) and Ni₂₃B₆ (Figure 14i), it is calculated that the $[11\bar{2}0]$ direction in the hBN is well aligned to the $[110]$ direction in the Ni₂₃B₆. Thus, the TEM analysis implies that the epitaxial relationship between hBN, Ni₂₃B₆, and Ni. To examine the single crystallinity, we carried out SAED measurements of transferred tri-layer hBN film onto 5-nm-thick amorphous SiN window (Figure 15), to prevent distortion by folding. The collected SAED patterns at nine frames from area i to ix in Figure 16 displays the one set of hexagonal dots, implying that the hBN film is single crystal across $\sim 1 \text{ mm}$ scale. Furthermore, the liquid crystal (LC)-assisted polarized optical microscopy (POM) study on hBN film reveals the absence of grain boundaries in spite of rotation of polarized angles from 0 to 180° C (Figure 17), indicating the single crystal hBN on a large scale^{3, 25}. This is compared with LC-assisted POM results of polycrystalline hBN grown at 1020° C as shown in Supplementary Fig. 11(a) (Figure 18).

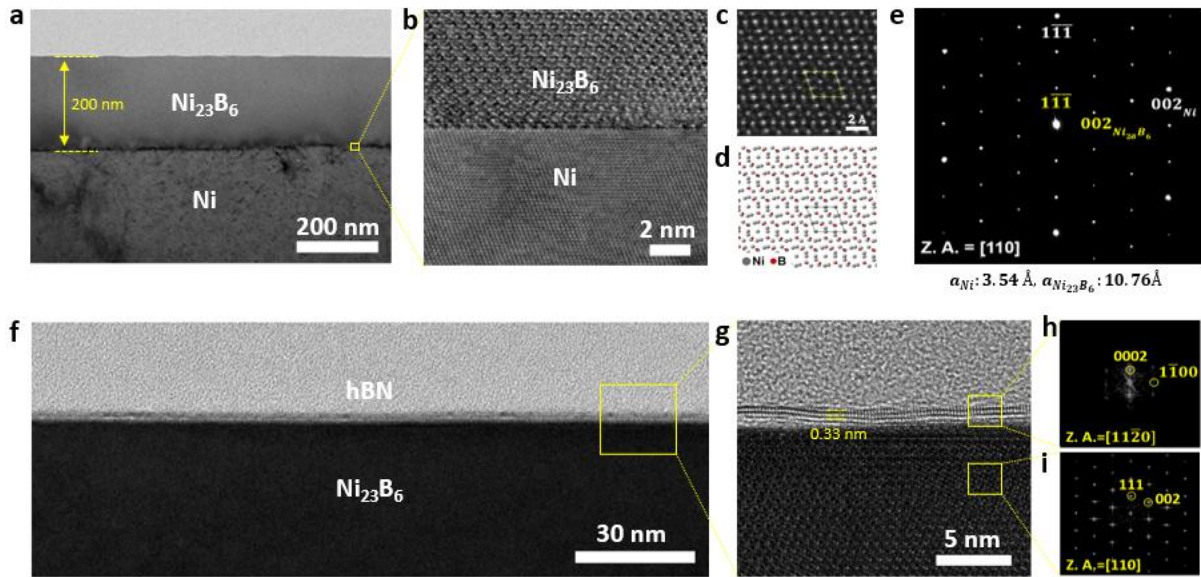


Figure 14. Epitaxial growth of hBN/Ni₂₃B₆ on Ni(111). (a-b) TEM images of Ni₂₃B₆/Ni interfaces and (c) STEM image of Ni₂₃B₆ at [110] zone axis. (d) simulated atomic structure of Ni₂₃B₆. (e) SAED pattern of Ni₂₃B₆ and Ni. (f) Low- and (g) High-magnification TEM image of trilayer hBN on Ni₂₃B₆. The corresponding FFT patterns of (h) hBN and (i) Ni₂₃B₆ from yellow squares in (g).

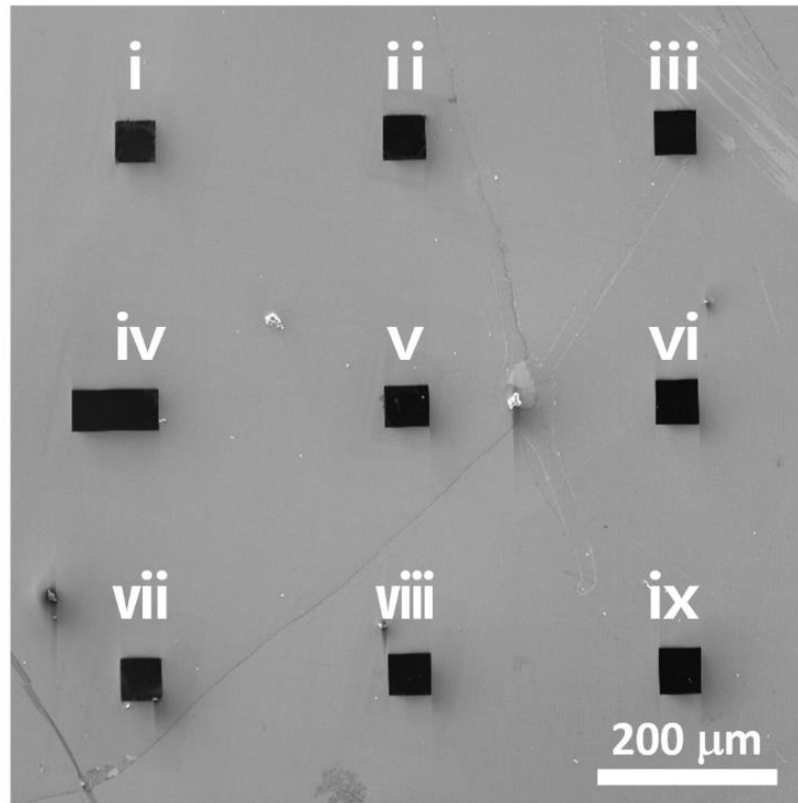


Figure 15. SEM image of trilayer hBN film on 5-nm-thick amorphous SiN windows.

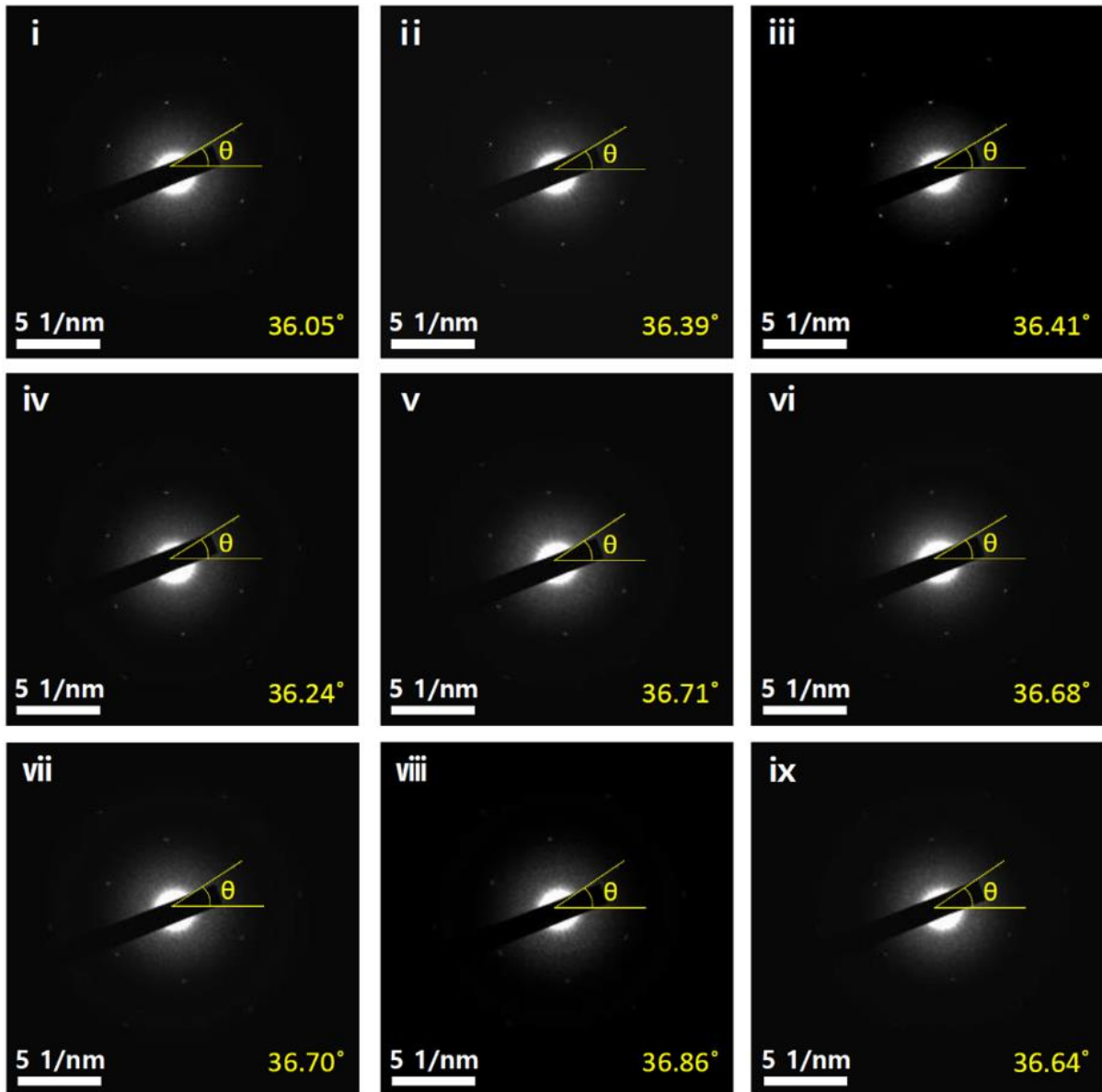


Figure 16. SAED pattern images from nine regions (i—ix) in Figure 15. The relative orientation angle (θ) of six-symmetrical hexagonal dots is $36.52^\circ \pm 0.24^\circ$, indicating that all the hexagonal lattices are aligned along one specific direction.

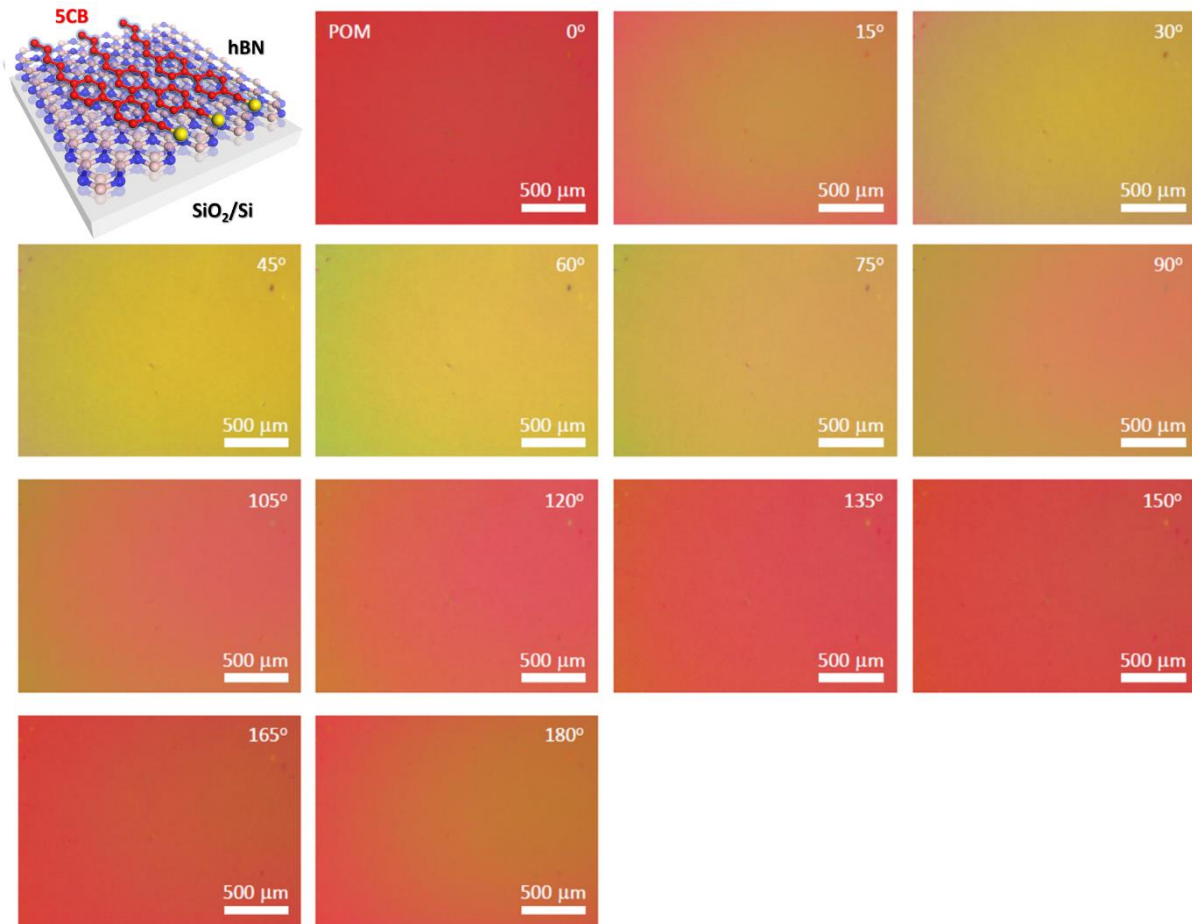


Figure 17. Schematic of LC (5CB) alignment on hBN and POM images of LC-coated hBN film as a function of the polarized light angles: 0, 30, 60, 90, and 180°.

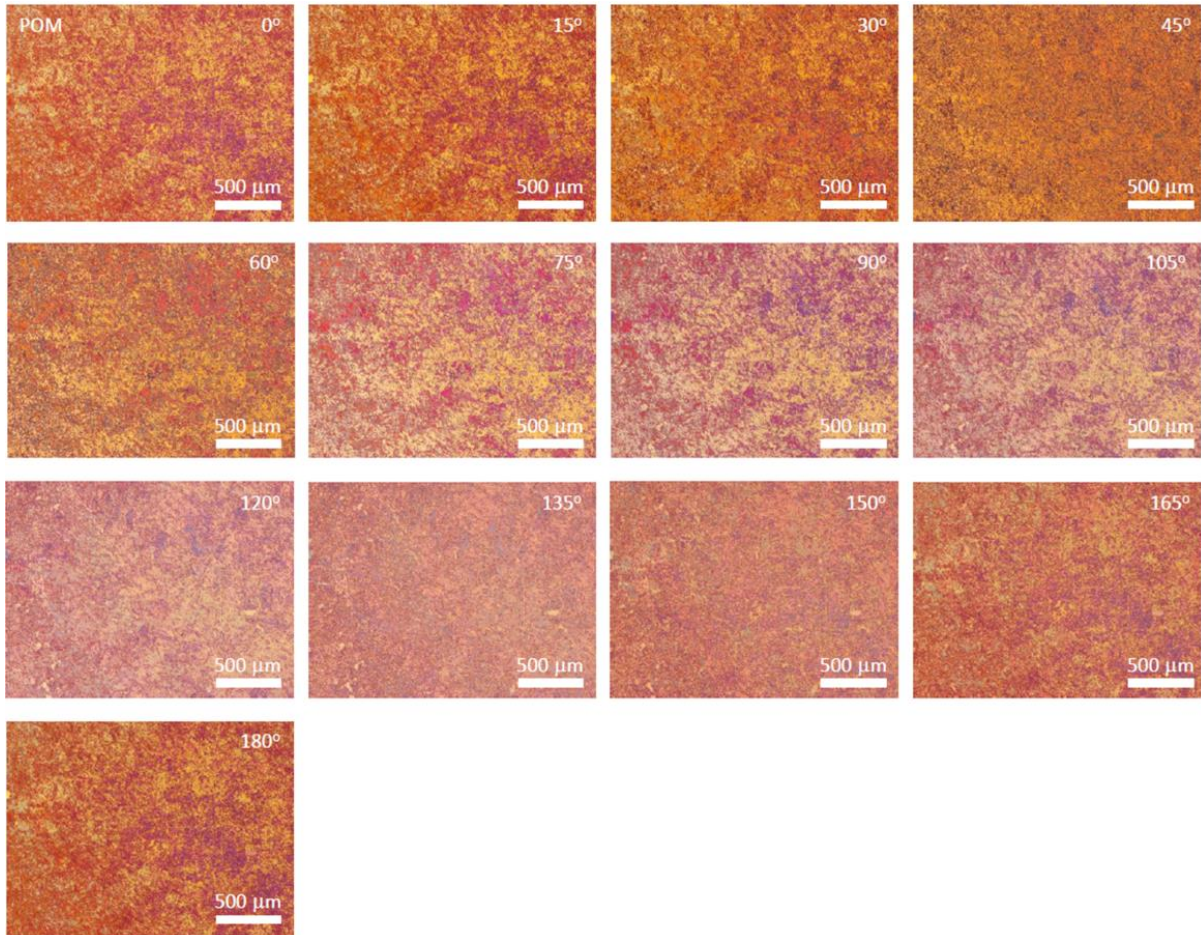


Figure 18. POM images of LC-coated polycrystal hBN film as a function of the polarized light angles: 0, 30, 60, 90, and 180°.

2.4.3 DFT calculation for the binding energies of hBN with Ni (111)

Based on the structural information of the lattice alignment between trilayer hBN and Ni (111), preference of a crystal orientation can be defined by density functional theory (DFT) calculations. We considered continuous trilayer hBN with N-terminated zigzag edge on Ni (111) surface (Figure 19a). The binding energy for trilayer hBN growing on Ni (111) was calculated as a function of γ , where γ is the rotation angle between the zigzag direction of the hBN and the Ni $\langle 110 \rangle$ direction (Figure 19b). There is only one maximum of binding energy at $\gamma = 0^\circ$, indicating the unique orientation of hBN islands on the Ni (111) surface, and it is worth noting that the binding differences between $\gamma = 0^\circ$ and other rotation angles increase slightly with the layer number of hBN increases.

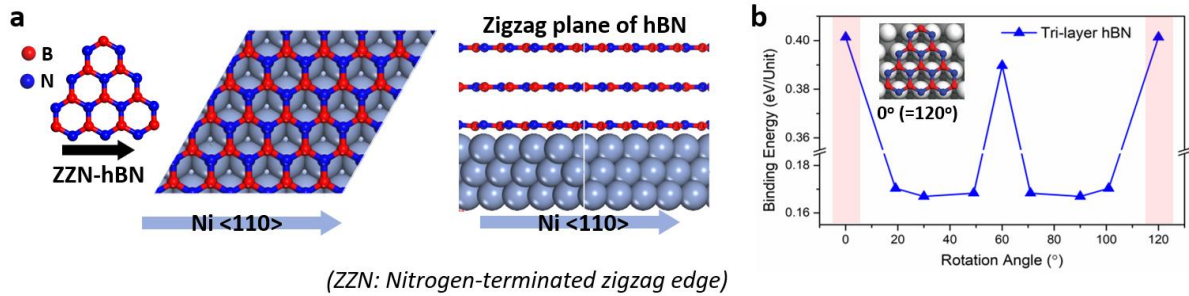


Figure 19. DFT calculations of the formation energies. (a) Schematic diagrams of the configuration of the hBN lattice and the surface of Ni (111) at top and side views, obtained from the TEM results in Figure 14g-i. (b) Binding energy calculation at various rotation angles between zigzag direction of N-terminated hBN and the Ni <110> direction. Black-, red-, and blue curves indicate mono-, bi-, and trilayer hBN.

2.4.4 Applications of CVD-grown single-crystal trilayer hBN

To demonstrate the feasibility of our tri-layer hBN film as a protecting layer for electrocatalyst of hydrogen evolution reaction (HER) to improve long-term stability, we evaluated the HER performance of Ni_{23}B_6 catalyst covered by the tri-layer hBN film (Figure 20). It is known that the transition metal borides demonstrated promising HER activities^{18, 26, 27}. The hBN layer does not contribute to the catalytic activity. To show the effect of hBN as a protection layer, we carried out a H_2 plasma treatment to eliminate the hBN layer on Ni_{23}B_6 (Figure 21). The HER was done in 0.5 M H_2SO_4 electrolyte (see Methods for a detailed description of the measurements). The current density as a function of potential (versus a reversible hydrogen electrode (RHE)) for hBN-covered Ni_{23}B_6 (hBN/ Ni_{23}B_6) and Ni_{23}B_6 along with Ni and Pt foils for comparison are shown in Figure 20b and Table 1. From the polarization curves, HER starts at less than 30 mV for the Ni_{23}B_6 catalyst and the overpotential at -10 mA cm^{-2} is 52 mV, which is comparable to amorphous Ni-B_x nanoparticles and porous Ni_3B catalysts^{18, 28}. It is noted that HER of Ni_{23}B_6 is not unknown. The Tafel slopes shown in Figure 20c provide additional information about the rate limiting step in the catalytic performance. The Tafel slopes for hBN/ Ni_{23}B_6 and Ni_{23}B_6 are 42 and 43 mV dec^{-1} at 30-60 mV of overpotential range, which is the best among known various nickel boride structures (Table 2). We point out that there are no differences of current densities ($\sim 20 \text{ mV}$) at 100 mA cm^{-2} and Tafel slopes (2 mV dec^{-1}) between hBN/ Ni_{23}B_6 and Ni_{23}B_6 . This indicates that the tri-layer hBN as a protecting layer does not obstruct the HER activation. Finally, we measured the electrochemical stability of the hBN/ Ni_{23}B_6 and Ni_{23}B_6 electrodes upto 2,000 cycles. The current density shows remarkable long-term stability with negligible difference in polarization curves and overpotential values after 2,000 cycles (Figure 20d-e). In contrast, we observed the degradation of HER performance for Ni_{23}B_6 after 650 cycles (Figure. 20f).

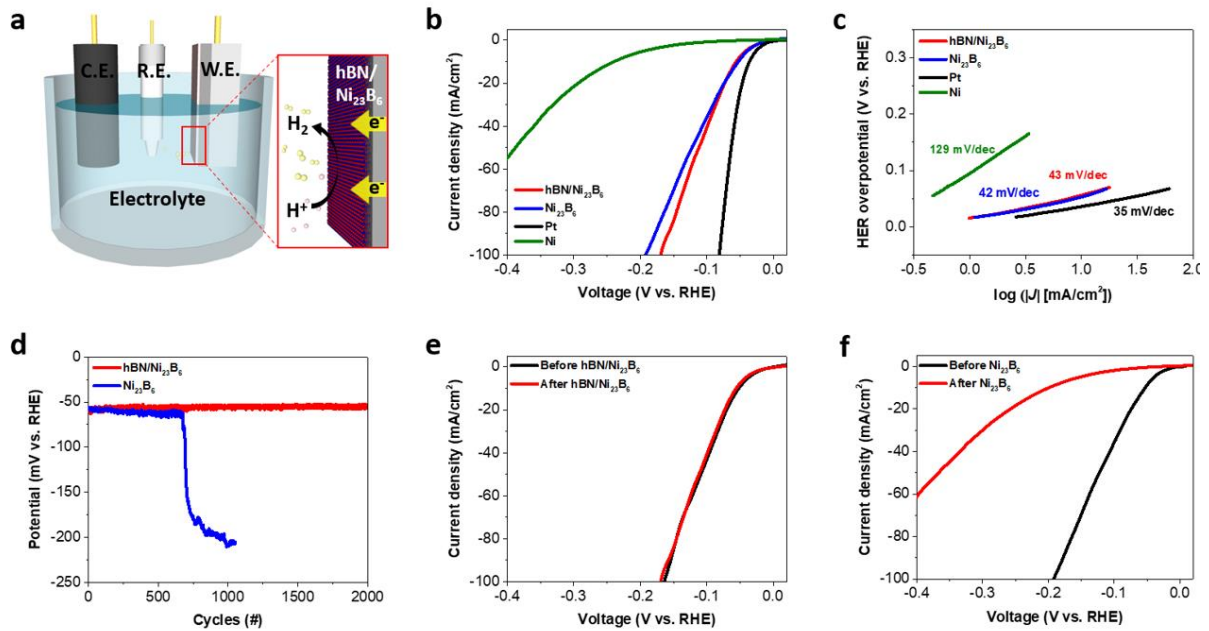


Figure 20. Comparison for HER catalytic performances between $\text{Ni}_{23}\text{B}_6/\text{Ni}$ and $\text{hBN}/\text{Ni}_{23}\text{B}_6/\text{Ni}$ electrodes (a) Schematic illustration of HER on $\text{hBN}/\text{Ni}_{23}\text{B}_6$ electrode. (b) Polarization curves and (c) Tafel slopes for $\text{hBN}/\text{Ni}_{23}\text{B}_6$, Ni_{23}B_6 , Ni and Pt foil measured in 0.5 M H_2SO_4 with a scan rate of 5 mV s^{-1} . (d) The electrochemical stability test of Ni_{23}B_6 with and without hBN. Polarization curves of (e) $\text{hBN}/\text{Ni}_{23}\text{B}_6$ (f) Ni_{23}B_6 before (black curve) and after (red) 2,000 cycles, respectively. .

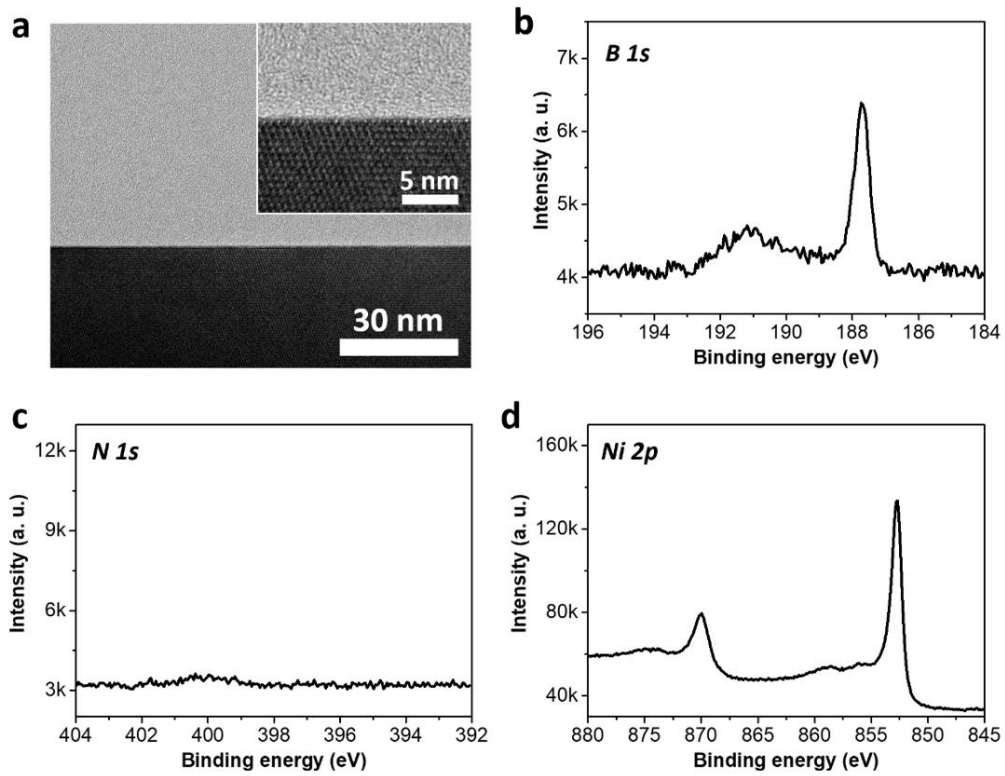


Figure 21. (a) Cross-sectional TEM image and XPS spectra of Ni_{23}B_6 without hBN protecting layer, after exposure to 50 W of H_2 plasma treatment for 5 min. (b) B 1s, (c) N 1s, and (d) Ni 2p spectra. The broad peak at 191.1 eV is estimated to be residual BN in B 1s spectrum.

Table 1 | Comparison of HER activity of hBN/Ni₂₃B₆ catalysts

	Potential at 10 mA/cm ² (mV vs RHE)	Tafel slope (mV dec ⁻¹)	Onset potential (V)
hBN/Ni ₂₃ B ₆	52	43	0.025
Ni ₂₃ B ₆	52	42	0.025
Pt	36	35	0.005
Ni	240	129	0.103

Table 2 | Comparison of HER activity of nickel boride catalysts in acidic electrolytes

	Electrolyte	Potential at 10 mA/cm ² (mV vs RHE)	Tafel slope (mV dec ⁻¹)	References
Ni ₂₃ B ₆ @hBN	0.5 M H ₂ SO ₄	52	42	This work
Ni ₂₃ B ₆	0.5 M H ₂ SO ₄	52	43	This work
Amorphous Ni-B _{0.54} @Ni NPs	0.5 M H ₂ SO ₄	45	43	Nano Energy 2016, 19, 98
Porous Ni ₃ B	0.5 M H ₂ SO ₄	79	85.32	Appl. Surf. Sci. 2019, 470, 591
Ni ₄ B ₃	0.5 M H ₂ SO ₄	182	114.7	Appl. Surf. Sci. 2019, 470, 591
Ni ₂ B	0.5 M H ₂ SO ₄	252	121.3	Appl. Surf. Sci. 2019, 470, 591
Amorphous Ni-B _{2.7} NPs on GCE	0.1 M HClO ₄	≈170	-	ChemCatChem 2016, 8, 708

* NPs: Nanoparticles

The hBN dielectric is an important component to reduce influence of underlying substrate SiO₂ in a field effect transistor (FET) using 2D active material such as MoS₂ or graphene. Actually, the SiO₂ substrate affect MoS₂ in terms of doping or charge trap. We measured the kelvin probe force microscopy (KPFM) images for MoS₂/SiO₂ and MoS₂/hBN/SiO₂ to investigate electron doping effects from underlying substrates (Figure 22a). The work function (4.3 eV) of MoS₂ in MoS₂/SiO₂ is lower than that (4.5 eV) of intrinsic MoS₂ due to electron doping effect from the SiO₂ substrate (Figure 22b). However, the work function (4.6 eV) of MoS₂ in MoS₂/hBN is close to the middle of the bandgap of MoS₂. This indicates our single-crystal tri-layer hBN effectively preserves intrinsic electrical property of MoS₂. The electrical properties were shown in the FET devices with hBN and without hBN (Figure 22c). While the drain current versus gate voltage curve of typical MoS₂ FET on SiO₂ shows mobility value of 56 cm²/Vs, that value of MoS₂ FET with hBN is 90 cm²/Vs. The threshold voltage in MoS₂ FET with hBN shifted to positive gate voltage, indicating that single-crystal tri-layer hBN prevents electron doping from the SiO₂ substrate.

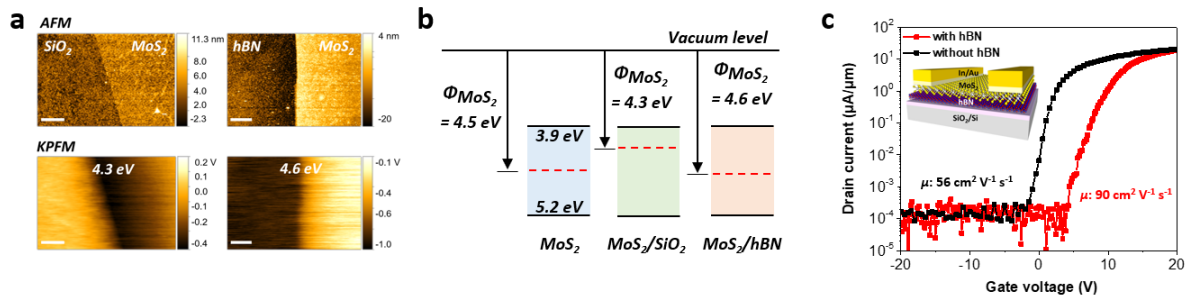


Figure 22. FET built with hBN as a dielectric. (a) AFM and KPFM results of MoS₂ on SiO₂ and hBN/SiO₂. The lower work function of MoS₂ on SiO₂ is due to strong electron doping from substrate (fermi level more close to conduction band). The fermi level position of MoS₂ on hBN/SiO₂ is close to the middle of the bandgap of MoS₂, indicates hBN preserves the intrinsic electrical property of MoS₂. (b) Energy band diagram of intrinsic MoS₂, MoS₂/SiO₂, and MoS₂/hBN/SiO₂. (c) Drain current versus gate voltage curve of typical MoS₂ FET on SiO₂ and hBN/SiO₂. The extracted mobility at room temperature is 56 cm²/Vs for SiO₂ and 90 cm²/Vs for hBN/SiO₂, respectively. The threshold voltage right shifted with hBN covering the SiO₂, preventing strong electron doping from the substrates. The inset shows FET device structure with hBN.

2.5 Conclusion

In summary, single-crystal trilayer hBN films were grown on a large-scale single-crystal Ni (111) foil with areas of $2 \times 5 \text{ cm}^2$ using the high-temperature and low-pressure CVD. The observed trilayer hBN grains are unidirectionally aligned on the single-crystal Ni_{23}B_6 alloy, produced by cooling of Ni containing B atoms. For the longer growth time, continuous single-crystal trilayer hBN film is formed by seamless stitching. The outstanding barrier effects without performance degradations of few-layer single-crystal hBN films are implying a potential for wide applications demanding few-layer-scale hBN film.

2.6 References

1. Li, M. Y.; Su, S. K.; Wong, H. S. P.; Li, L. J., How 2D semiconductors could extend Moore's law. *Nature* **2019**, *567* (7747), 169-170.
2. Dean, C. R.; Young, A. F.; Meric, I.; Lee, C.; Wang, L.; Sorgenfrei, S.; Watanabe, K.; Taniguchi, T.; Kim, P.; Shepard, K. L.; Hone, J., Boron nitride substrates for high-quality graphene electronics. *Nat Nanotechnol* **2010**, *5* (10), 722-726.
3. Lee, J. S.; Choi, S. H.; Yun, S. J.; Kim, Y. I.; Boandoh, S.; Park, J. H.; Shin, B. G.; Ko, H.; Lee, S. H.; Kim, Y. M.; Lee, Y. H.; Kim, K. K.; Kim, S. M., Wafer-scale single-crystal hexagonal boron nitride film via self-collimated grain formation. *Science* **2018**, *362* (6416), 817-821.
4. Wang, L.; Xu, X. Z.; Zhang, L. N.; Qiao, R. X.; Wu, M. H.; Wang, Z. C.; Zhang, S.; Liang, J.; Zhang, Z. H.; Zhang, Z. B.; Chen, W.; Xie, X. D.; Zong, J. Y.; Shan, Y. W.; Guo, Y.; Willinger, M.; Wu, H.; Li, Q. Y.; Wang, W. L.; Gao, P.; Wu, S. W.; Zhang, Y.; Jiang, Y.; Yu, D. P.; Wang, E. G.; Bai, X. D.; Wang, Z. J.; Ding, F.; Liu, K. H., Epitaxial growth of a 100-square-centimetre single-crystal hexagonal boron nitride monolayer on copper. *Nature* **2019**, *570* (7759), 91-95.
5. Chen, T. A.; Chuu, C. P.; Tseng, C. C.; Wen, C. K.; Wong, H. S. P.; Pan, S. Y.; Li, R. T.; Chao, T. A.; Chueh, W. C.; Zhang, Y. F.; Fu, Q.; Yakobson, B. I.; Chang, W. H.; Li, L. J., Wafer-scale single-crystal hexagonal boron nitride monolayers on Cu (111). *Nature* **2020**, *579* (7798), 219-223.
6. Liu, Z.; Gong, Y.; Zhou, W.; Ma, L.; Yu, J.; Idrobo, J. C.; Jung, J.; MacDonald, A. H.; Vajtai, R.; Lou, J.; Ajayan, P. M., Ultrathin high-temperature oxidation-resistant coatings of hexagonal boron nitride. *Nat. Commun.* **2013**, *4*, 2541.
7. Kim, S. M.; Hsu, A.; Park, M. H.; Chae, S. H.; Yun, S. J.; Lee, J. S.; Cho, D. H.; Fang, W. J.; Lee, C.; Palacios, T.; Dresselhaus, M.; Kim, K. K.; Lee, Y. H.; Kong, J., Synthesis of large-area multilayer hexagonal boron nitride for high material performance. *Nat. Commun.* **2015**, *6*, 8662.
8. Uchida, Y.; Nakandakari, S.; Kawahara, K.; Yamasaki, S.; Mitsuhara, M.; Ago, H., Controlled Growth of Large-Area Uniform Multilayer Hexagonal Boron Nitride as an Effective 2D Substrate. *ACS Nano* **2018**, *12* (6), 6236-6244.

9. Caneva, S.; Weatherup, R. S.; Bayer, B. C.; Blume, R.; Cabrero-Vilatela, A.; Braeuninger-Weirner, P.; Martin, M. B.; Wang, R. Z.; Baetz, C.; Schloegl, R.; Meyer, J. C.; Hofmann, S., Controlling Catalyst Bulk Reservoir Effects for Monolayer Hexagonal Boron Nitride CVD. *Nano Lett.* **2016**, *16* (2), 1250-1261.
10. Shi, Y. M.; Hamsen, C.; Jia, X. T.; Kim, K. K.; Reina, A.; Hofmann, M.; Hsu, A. L.; Zhang, K.; Li, H. N.; Juang, Z. Y.; Dresselhaus, M. S.; Li, L. J.; Kong, J., Synthesis of Few-Layer Hexagonal Boron Nitride Thin Film by Chemical Vapor Deposition. *Nano Lett.* **2010**, *10* (10), 4134-4139.
11. Ismach, A.; Chou, H.; Ferrer, D. A.; Wu, Y. P.; McDonnell, S.; Floresca, H. C.; Covacevich, A.; Pope, C.; Piner, R.; Kim, M. J.; Wallace, R. M.; Colombo, L.; Ruoff, R. S., Toward the Controlled Synthesis of Hexagonal Boron Nitride Films. *ACS Nano* **2012**, *6* (7), 6378-6385.
12. Gao, Y.; Ren, W. C.; Ma, T.; Liu, Z. B.; Zhang, Y.; Liu, W. B.; Ma, L. P.; Ma, X. L.; Cheng, H. M., Repeated and Controlled Growth of Monolayer, Bilayer and Few-Layer Hexagonal Boron Nitride on Pt Foils. *ACS Nano* **2013**, *7* (6), 5199-5206.
13. Song, L.; Ci, L. J.; Lu, H.; Sorokin, P. B.; Jin, C. H.; Ni, J.; Kvashnin, A. G.; Kvashnin, D. G.; Lou, J.; Yakobson, B. I.; Ajayan, P. M., Large Scale Growth and Characterization of Atomic Hexagonal Boron Nitride Layers. *Nano Lett.* **2010**, *10* (8), 3209-3215.
14. Kim, K. K.; Hsu, A.; Jia, X. T.; Kim, S. M.; Shi, Y. M.; Dresselhaus, M.; Palacios, T.; Kong, J., Synthesis and Characterization of Hexagonal Boron Nitride Film as a Dielectric Layer for Graphene Devices. *ACS Nano* **2012**, *6* (10), 8583-8590.
15. Jang, A. R.; Hong, S.; Hyun, C.; Yoon, S. I.; Kim, G.; Jeong, H. Y.; Shin, T. J.; Park, S. O.; Wong, K.; Kwak, S. K.; Park, N.; Yu, K.; Choi, E.; Mishchenko, A.; Withers, F.; Novoselov, K. S.; Lim, H.; Shin, H. S., Wafer-Scale and Wrinkle-Free Epitaxial Growth of Single-Orientated Multilayer Hexagonal Boron Nitride on Sapphire. *Nano Lett.* **2016**, *16* (5), 3360-3366.
16. Liu, D. H.; Chen, X. S.; Yan, Y. P.; Zhang, Z. W.; Jin, Z. P.; Yi, K. Y.; Zhang, C.; Zheng, Y. J.; Wang, Y.; Yang, J.; Xu, X. F.; Chen, J.; Lu, Y. H.; Wei, D. P.; Wee, A. T. S.; Wei, D. C., Conformal hexagonal-boron nitride dielectric interface for tungsten diselenide devices with improved mobility and thermal dissipation. *Nat. Commun.* **2019**, *10*, 1188.

17. Shi, Z. Y.; Wang, X. J.; Li, Q. T.; Yang, P.; Lu, G. Y.; Jiang, R.; Wang, H. S.; Zhang, C.; Cong, C. X.; Liu, Z.; Wu, T. R.; Wang, H. M.; Yu, Q. K.; Xie, X. M., Vapor-liquid-solid growth of large-area multilayer hexagonal boron nitride on dielectric substrates. *Nat. Commun.* **2020**, *11*, 849.
18. Zhang, P.; Wang, M.; Yang, Y.; Yao, T.; Han, H.; Sun, L., Electroless plated Ni-B_x films as highly active electrocatalysts for hydrogen production from water over a wide pH range. *Nano Energy* **2016**, *19*, 98-107.
19. Masa, J.; Sinev, I.; Mistry, H.; Ventosa, E.; de la Mata, M.; Arbiol, J.; Muhler, M.; Roldan Cuenya, B.; Schuhmann, W., Ultrathin High Surface Area Nickel Boride (Ni₃B) Nanosheets as Highly Efficient Electrocatalyst for Oxygen Evolution. *Adv. Energy. Mater.* **2017**, *7* (17), 1700381.
20. Jiang, W. J.; Niu, S.; Tang, T.; Zhang, Q. H.; Liu, X. Z.; Zhang, Y.; Chen, Y. Y.; Li, J. H.; Gu, L.; Wan, L. J.; Hu, J. S., Crystallinity-Modulated Electrocatalytic Activity of a Nickel(II) Borate Thin Layer on Ni₃B for Efficient Water Oxidation. *Angew. Chem. Int. Ed.* **2017**, *56* (23), 6572-6577.
21. Rogl, P.; Schuster, J., Boron Nitride and Silicon Nitride Systems. *Inst. Phys. Chem. Univ. Vienna Austria* **1991**, 79-86.
22. Kowanda, C.; Speidel, M. O., Solubility nitrogen in liquid nickel and binary Ni-X alloys (X = Cr, Mo, W, Mn, Fe, Co) under elevated pressure. *Scripta Mater.* **2003**, *48* (8), 1073-1078.
23. Battezzati, L.; Antonione, C.; Baricco, M., Undercooling of Ni-B and Fe-B alloys and their metastable phase diagrams. *J. Alloy. Compd.* **1997**, *247*, 164-171.
24. Liu, F.; Xu, J. F.; Zhang, D.; Jian, Z. Y., Solidification of Highly Undercooled Hypereutectic Ni-Ni₃B Alloy Melt. *Metall. Mater. Trans. A* **2014**, *45a* (11), 4810-4819.
25. Park, J. H.; Park, J. C.; Yun, S. J.; Kim, H.; Luong, D. H.; Kim, S. M.; Choi, S. H.; Yang, W.; Kong, J.; Kim, K. K.; Lee, Y. H., Large-Area Monolayer Hexagonal Boron Nitride on Pt Foil. *ACS Nano* **2014**, *8* (8), 8520-8528.
26. Liang, Y. H.; Sun, X. P.; Asiri, A. M.; He, Y. Q., Amorphous Ni-B alloy nanoparticle film on Ni foam: rapid alternately dipping deposition for efficient overall water splitting. *Nanotechnology* **2016**, *27* (12).

27. Chen, X. C.; Yu, Z. X.; Wei, L.; Zhou, Z.; Zhai, S. L.; Chen, J. S.; Wang, Y. Q.; Huang, Q. W.; Karahan, H. E.; Liao, X. Z.; Chen, Y., Ultrathin nickel boride nanosheets anchored on functionalized carbon nanotubes as bifunctional electrocatalysts for overall water splitting. *J. Mater. Chem. A* **2019**, 7 (2), 764-774.
28. Xu, X. S.; Deng, Y. X.; Gu, M. H.; Sun, B. T.; Liang, Z. Q.; Xue, Y. J.; Guo, Y. C.; Tian, J.; Cui, H. Z., Large-scale synthesis of porous nickel boride for robust hydrogen evolution reaction electrocatalyst. *Appl. Surf. Sci.* **2019**, 470, 591-595.
29. Jin, S.; Huang, M.; Kwon, Y.; Zhang, L. N.; Li, B. W.; Oh, S.; Dong, J. C.; Luo, D.; Biswal, M.; Cuning, B. V.; Bakharev, P. V.; Moon, I.; Yoo, W. J.; Camacho-Mojica, D. C.; Kim, Y. J.; Lee, S. H.; Wang, B.; Seong, W. K.; Saxena, M.; Ding, F.; Shin, H. J.; Ruoff, R. S., Colossal grain growth yields single-crystal metal foils by contact-free annealing. *Science* **2018**, 362 (6418), 1021-1025.

Chapter 3: Layer-Controlled Single-Crystal Hexagonal Boron Nitride Film with AA'-Stacking Order by Buffer Layer Formation

3.1 Abstract

Thickness controlled growth of hexagonal boron nitride (hBN) single crystal film is highly desirable for fabrication of two-dimensional (2D) material based various barrier applications. Several approaches to control the thickness have been demonstrated using chemical vapor deposition (CVD). However, a route of precisely controlling the number of layers with single-crystallinity is still challenging. Here, we demonstrate a method for controlling the number of layers of single-crystalline multilayer hBN films at the 2-inch sapphire scale by temperature-depended growth using remote inductively coupled plasma CVD. The introduction of N atoms in plasma generated environment leads to form Al-N bonding between the surface of sapphire and monolayer hBN film during the growth. As formed monolayer hBN with Al-N bond acts as buffer layer for growth of bilayer and trilayer hBN, as well as leads to increase of interlayer spacing of bilayer and trilayer hBN. We also demonstrated that the wet etching process enables separation of monolayer hBN from the sapphire by breaking chemical bonds of Al-N. Furthermore, we utilized multilayer hBN films as a potential membrane adjusting molecular blocking and separation.

3.2 Introduction

Hexagonal boron nitride (hBN), a honeycomb lattice consisting of alternating B and N atoms, is a representative wide band gap (~ 6 eV) two-dimensional (2D) insulator¹⁻³. Because hBN has natures of atomically flat surface without dangling bonds at the surface⁴ and thermal stability⁵, it has been demonstrated as ideal substrate for 2D material-based transistor⁶⁻⁸, encapsulation layers⁹, oxidation-resistant coatings¹⁰, deep ultraviolet light emitters^{1, 11}, and tunneling barrier in electronics^{12, 13}. In addition, impermeability of hBN layers, even a few atomic thicknesses, shows great potential for use membrane applications such as gas barrier and proton exchange membrane^{14, 15}. To achieve such desired applications using hBN layers, lots of efforts have been made to fulfill the requirements such as a development of high-quality and large-scale film, controllability of number of layers, and reproducibility¹⁶. In particular, in the tunneling transistor with hBN barrier, tunneling current exponentially depends exponentially on the number of hBN layers¹⁷, as well as in the various

membranes, the number of layers is an important factor to decide the mechanical strength¹⁸⁻²⁰.

Chemical vapor deposition (CVD) method has been widely adopted for the direct growth of a high-quality and a large-scale hBN films with controllable number of layers on various metal substrates such as Cu²¹⁻²⁵, Ni²⁶⁻²⁸, Pt²⁹, and Fe³⁰. Because each metal substrates show different solubilities of B and N, layer-controlled growth of hBN films has been demonstrated that by solubility-controlled substrates, designed sandwich structure composed of different metal substrates²⁶ or pretreated metal surface with NH₃³⁰. In addition, it has been demonstrated that the number of hBN layers on metal surface is greatly influenced by the growth time^{23, 27, 28, 31}, pressure^{21, 22, 32}, and precursor feeding rate^{24, 25, 29, 30, 33}. However, layer-controlled hBN films have been shown high density of wrinkles and roughness, and randomly oriented hBN grains. These kinds of defects degrade the performance of practical applications. Furthermore, CVD grown hBN layers on metal surface are inevitable to transfer to target substrate for fabricating practical applications. This process also would degrade the quality of hBN film due to the formation of folded area and the adsorption of polymeric impurities from supporting polymer³³. Therefore, it is still a daunting task to achieve large-scale single crystal hBN films with controlled the number of layers on insulating substrate, and to apply for large-scale practical 2D membranes.

In this study, we obtained 2-inch-scale single-crystalline layer-controlled multilayer hBN film with AA' stacking sequence by temperature-depended growth in a remote ICP-CVD system. Single crystalline bilayer and trilayer hBN films can be grown on buffer layer (monolayer hBN) at higher temperature. The spectroscopic and microscopic measurements were revealed single-crystalline nature and influences from buffer layer. Furthermore, we also present a route to separate the buffer layer as a monolayer hBN using AlN etchant.

3.3 Experimental section

3.3.1 Layer-controllable growth of hBN on 2-inch sapphire

Multilayer hBN with an AA' stacking order was grown by remote ICP-CVD system (Figure 1). A 2-inch *c*-plane sapphire was used as a substrate for the hBN growth. The substrate was placed in the center of ~3-inch alumina tube furnace of ICP-CVD. A borazine (Gelest, Inc.) precursor flask was placed in a water bath at -15 °C. The bath temperature before the growth of hBN was increased up to 25 °C. Before ramping up the temperature, the base pressure of chamber is pumped down to the value of 1×10^{-4} torr, and 10 standard cubic centimeters (sccm) of Ar gas was introduced. The furnace temperature is ramped up to 1220 °C with keeping Ar flow. Plasma was generated at a power of 30 W under a flow of borazine

(0.1 sccm) and Ar (10 sccm) gases for 30 mins. After the growth of the hBN films, the sample was rapidly cooled down to room temperature (Figure 2). The growth temperatures employed to obtain mono-, bi-, and trilayer hBN were 1020, 1120, and 1220 °C, respectively. It is worth noting that the plasma powers of 10-50 W cause negligible affects in our optimized growth condition. We further confirmed absence of hBN grown at 1320 °C, implying the etching of hBN is more active than growth.

3.3.2 Transfer of hBN films onto other substrate.

The as-grown hBN films were transferred to arbitrary substrates by conventional wet etching process of thin film AlN. In brief, (i) poly(methyl methacrylate) (PMMA) is spin-coated on the hBN, (ii) and it is immersed into diluted HF (~10%) in H₂O as an AlN-etchant (for an hour). The HF etchant reacts with Al-N, and break (iii) Then, the floating PMMA/hBN film is transferred onto the target substrate, and (iv) PMMA is removed by acetone.

3.3.3 Porous support casting for gas transport measurements

Casting polymer solution was prepared by mixing ~16 wt% polyethersulfone (PES) resin, ~82 wt% N-methyl-2-pyrrolidone, and ~2 wt% isopropanol, and baked in an oven at 75 °C for ~24 hours and subsequently allowed to cool and degas for ~12 hours³⁴. The PES casting was performed by spin-coating method for uniform thickness (600 r.p.m.). In order to conduct the phase inversion reaction of PES forming porous support, the PES/hBN/sapphire was immersed in a deionized water bath for an hour. The delamination of porous PES/hBN from sapphire was performed by transfer method in **Section 3.3.2**. The porous PES/hBN stack was rinsed with deionized water followed by dried with N₂ blowing.

3.3.4 Characterization

The surface morphology of hBN was characterized by optical microscopy (Axio Scope. A1, Carl Zeiss), SEM (Verios 460, FEI), and AFM (Dimension Icon, Bruker). XPS (ESCALAB 250 Xi, Thermo Scientific) was performed to determine chemical compositions. Raman spectrum was obtained using a micro Raman spectrometer (alpha 300, WITec GmbH) with a laser excitation wavelength of 532 nm and about 2 mW power. The UV-vis adsorption spectrum (Cary 5000 UV-vis-NIR, Agilent) was measured to estimate the optical band gap of hBN on the quartz substrate. The optical band gap energy

was determined by using the formula of a direct band gap semiconductor: $\alpha = C(E - E_g)^{1/2}/E$ (where α is the absorption coefficient, C is a constant, E is the photon energy, and E_g is the optical bandgap energy). The plot of $(\alpha E)^2$ vs. E should be a straight line. Therefore, when $(\alpha E)^2 = 0$, E should be equal to E_g . For atomic-resolution imaging and SAED measurements, low-voltage Cs aberration-corrected transmission electron microscopy (TEM) (Titan Cube G2 60-300, FEI) was performed at 80 kV using a monochromatic electron beam. To evaluate the lattice orientations of hBN film, SAED patterns in TEM (JEM-2100F, JEOL) on 5-nm-thick amorphous SiN windows and POM (Eclipse LV100-POL equipped with a heating stage, Nikon) on SiO₂/Si wafer after LC (4-cyano-4'-pentylbiphenyl (5CB), Alfa Aesar) coating were employed. The trilayer hBN films transferred onto PET substrate were used for water vapor transmission rate (WVTR, Aquatran model2, MOCON) measurement. The gas permeation tests of single- and mixture gas were carried out in a homemade permeation cell. The mass flow controller (MFC) and MS were used for estimation of permeation rates.

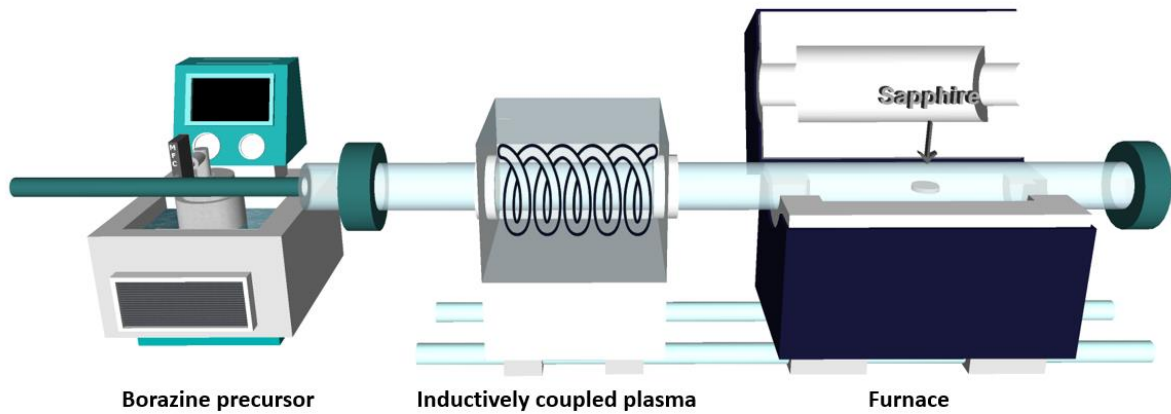


Figure 1. (a) Schematic illustrations of remote ICP-CVD with liquid borazine precursor.

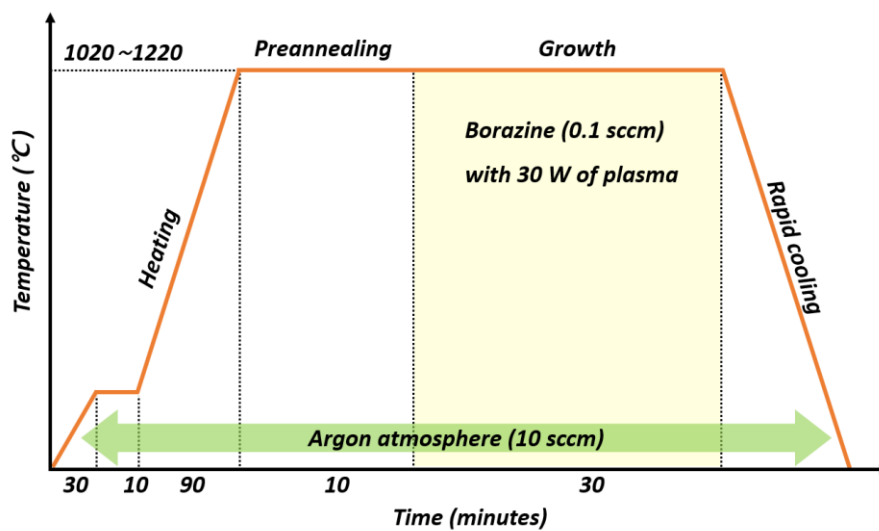


Figure 2. Annealing protocol for the growth of hBN. The growth temperatures employed to obtain mono-, bi-, and trilayer hBN were 1020, 1120, and 1220 °C, respectively.

3.4 Results and discussions

3.4.1 Layer-controllable multilayer hBN on sapphire

We obtained a uniform 2-inch wafer-scale trilayer hBN film on commercial *c*-plane sapphire using a remote ICP-CVD method with borazine (BHNH_3) as the precursor (details in Methods). Under plasma discharge, the borazine precursors are pre-dissociated into radicals. This leads to the temperature compensation for the hBN formation on non-catalytic substrate³⁵. The summary of temperature-dependent mono-, bi-, and trilayer hBN growth route at 1020, 1120, and 1220 °C, respectively, is indicated in [Figure 3a](#). The AFM images showed a striking result of high-uniform mono-, bi-, and trilayer hBN films without surface wrinkle ([Figure 3b-e and 4](#)). The RMS values in AFM images were estimated to be ranges of 0.095~0.131 nm on the surface of as-grown hBN/sapphire, which are comparable value to bare sapphire surface (RMS: 0.112 nm) ([Figure 5](#)). However, tetralayer hBN film was not observed at growth temperature of 1320 °C in our growth condition using plasma environment ([Figure 6](#)). A sapphire substrate was damaged by the high-temperature plasma environment rather hBN growth on surface, which indicates etching reaction is more active than growth. The representative photographs of highly transparent and uniform trilayer hBN films were shown on a growth substrate of 2-inch sapphire wafer ([Figure 3f](#)) and on SiO_2/Si substrate in its entirety after wet-etching transfer process ([Figure 3g](#)). Moreover, the ultraviolet-visible (UV-vis) absorption spectra indicate not only specific absorption wavelength of hBN ~ 200 nm but also increase as a function of the number of layers ([Figure 7a](#)) corresponding with previous study²⁶. The Raman spectra of the as-grown and transferred hBN clearly indicated a characteristic E_{2g} phonon mode at 1370 cm^{-1} using 532 laser excitation ([Figure 7b and c](#)). The Raman intensity of the E_{2g} phonon mode increased linearly with growth temperature on both substrates. Furthermore, the full width at half maximum (FWHM) of transferred hBN films were measured to be $\sim 17 \text{ cm}^{-1}$, indicating high-quality hBN crystal³⁶. A longer growth time up to ~ 90 min shows the maintaining thickness of trilayer hBN, but further growth time to ~ 120 min alter the thickness and surface morphology of the film. This indicates that the growth process is influenced by the layer-by-layer (Frank van der Merwe) mechanism until growth time of ~ 90 min, whereas that is influenced by the island growth mechanism started between 90-120 min ([Figure 8](#)).

We characterized the single crystallinity of trilayer hBN film on a large area via two conventional route. First, we identified AA' stacking order of trilayer hBN film with hexagonal B and N atoms by high-resolution TEM measurement ([Figure 9a](#)). Fast Fourier transform (FFT) pattern from [Figure 9a](#) displays the one set of hexagonal spots, indicating the hexagonal structure. The d-spacing of the $(1\bar{1}00)$ plane is 0.217 nm, implying single-crystalline hBN film corresponding with previous reports³⁷. We

carried out selected area electron diffraction measurements of transferred trilayer hBN film onto 5-nm-thick amorphous SiN windows (Figure 9b), to avoid distortion by folding of film. The collected SAED patterns at eight frames from area I to vii in Figure 9c displays the single set of hexagonal spots, assuring that the trilayer hBN film has single-crystal nature in a selected area of approximately ~ 1 μm by ~ 1 μm . We further confirmed single-crystalline nature by polarized optical microscopy (POM) of a liquid crystal (LC)-coated trilayer hBN film on SiO₂/Si substrate (Figure 10a). The POM patterns in the absence of rotated grain orientation are not altered, in spite of different polarized angles (Figure 10b-f), again showing single-crystalline nature of trilayer hBN on a large scale^{37, 38}.

To understand the effects of the plasma discharge on the homogeneous multilayer hBN, we applied different plasma powers at 1220 °C with borazine flow of 0.1 sccm (Figure 11). When the plasma power was 0 W, that is, for without plasma discharge, inhomogeneous multilayer hBN with relatively high surface roughness and broad UV absorption, indicating poor crystallinity (Figure 12a and d). With hBN growth on the sapphire substrate below 1400 °C³⁵, it was impossible to grow a uniform multilayer hBN film, regardless of the growth condition. Even at a low plasma power, 10 W, a uniform hBN film was grown with same thickness grown at 30 W (Figure 10a-c). At 50 W of the plasma power, the result of hBN is still the same as uniform trilayer hBN grown at 30 W (Figure 10d). At higher plasma power (80 W), however, the both reactions of growth and etching were observed on the surface, leading to exposed sapphire surface (Figure 10e). Furthermore, we observed that the etching reaction is dominant at 100 W (Figure 10f). The plasma power of approximately 80 W was the threshold for uniform multilayer hBN growth without plasma etching.

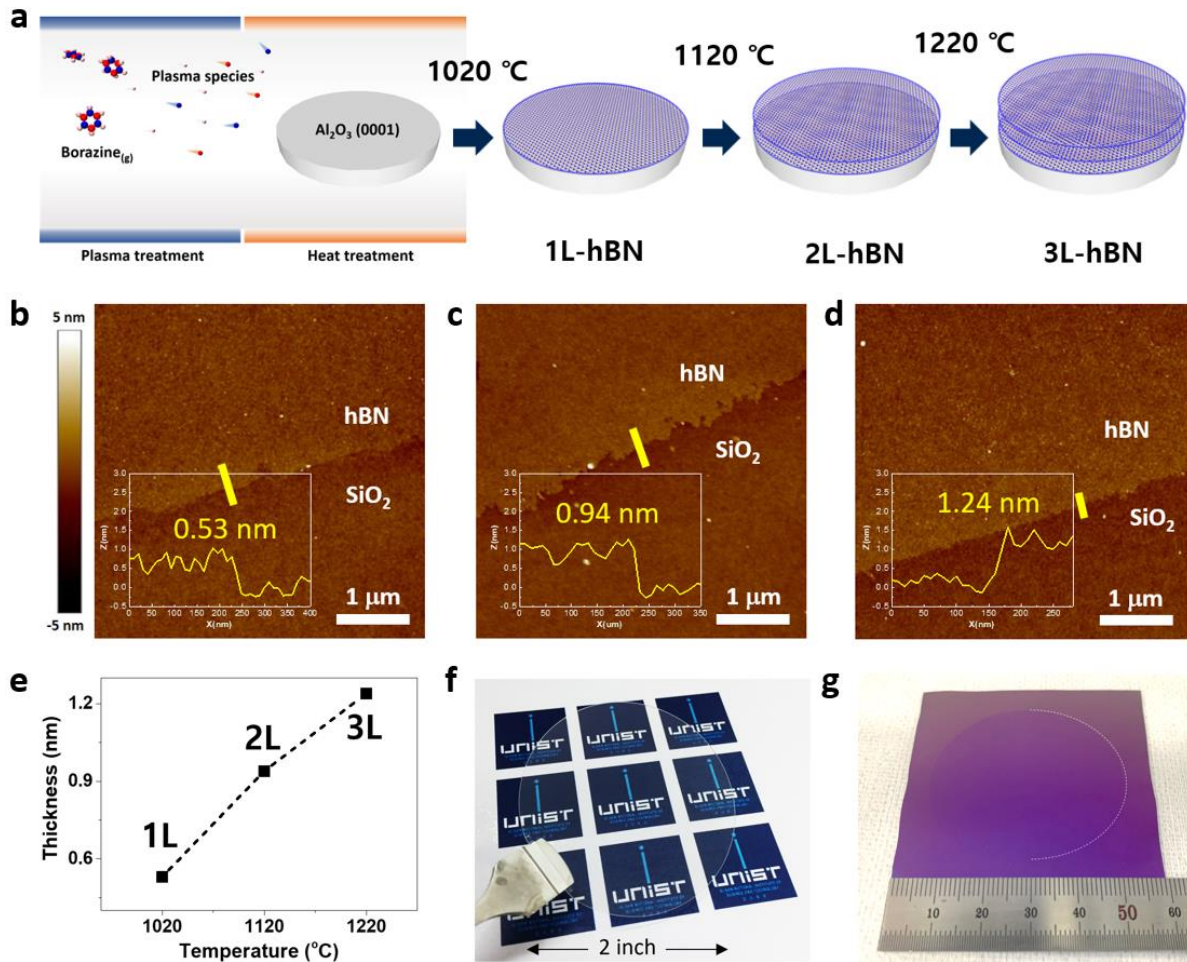


Figure 3. Wafer-scale growth of mono-, bi-, trilayer hBN films using remote ICP-CVD. (a) Schematic description of temperature-depended layer-controlled growth. AFM images of (b) mono-, (c) bi-, (d) trilayer hBN are indicating the uniform continuous film at the edge of film. The yellow solid lines show the (inset) height profile of each films. (e) Relationship between growth temperature and the number of hBN layers. (f) A representative photograph of as-grown uniform 2-inch trilayer hBN film on sapphire. (g) As transferred trilayer hBN onto SiO₂/Si substrate.

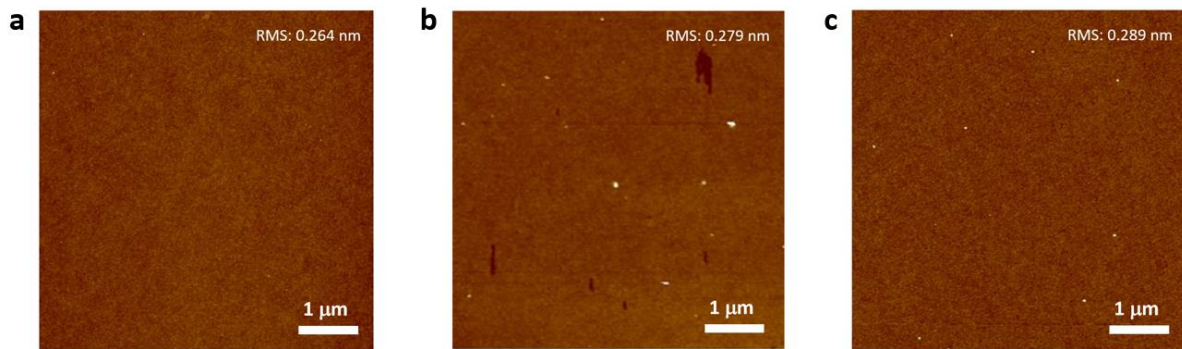


Figure 4. AFM images of as-transferred (a) mono-, (b) bi-, and (c) trilayer hBN films on SiO₂/Si.

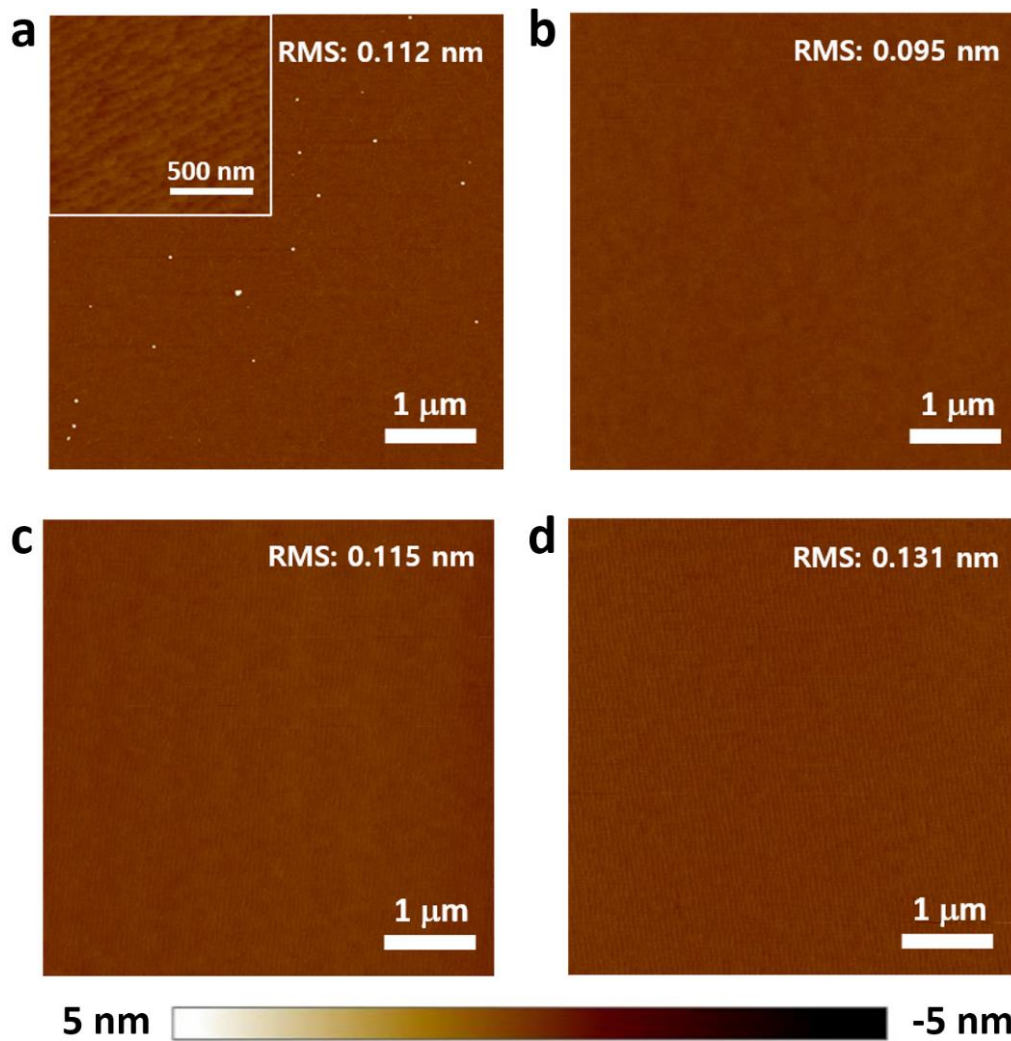


Figure 5. AFM images of as-grown hBN on sapphire. (a) A surface of sapphire wafer shows highly smooth with extremely low RMS value of 0.112 nm. Surfaces of (b) mono-, (c) bi-, and (d) trilayer hBN on sapphire are showing comparable surface roughness to bare sapphire.

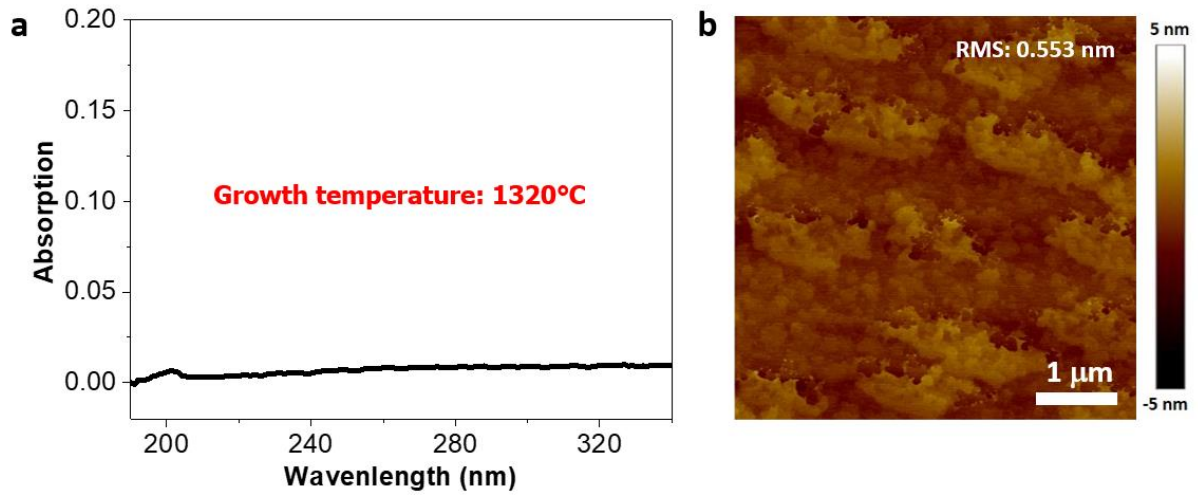


Figure 6. (a) UV absorption spectrum and corresponding (b) AFM image on sapphire after hBN growth at 1320 °C. Note that the considerable increase of RMS value is observed by comparison with a bare sapphire.

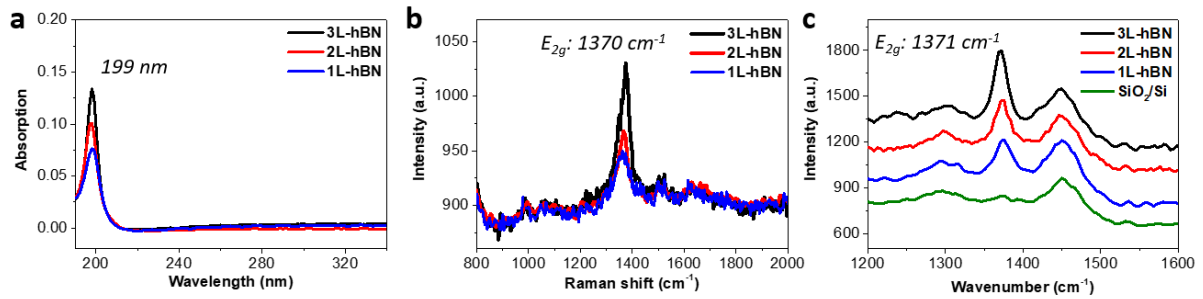


Figure 7. (a) UV absorption spectra of as-grown mono-, bi-, tri-layer hBN films on sapphire. (b) Corresponding Raman spectra of hBN films with different number of layers measured on (b) sapphire and (c) SiO_2/Si substrates.

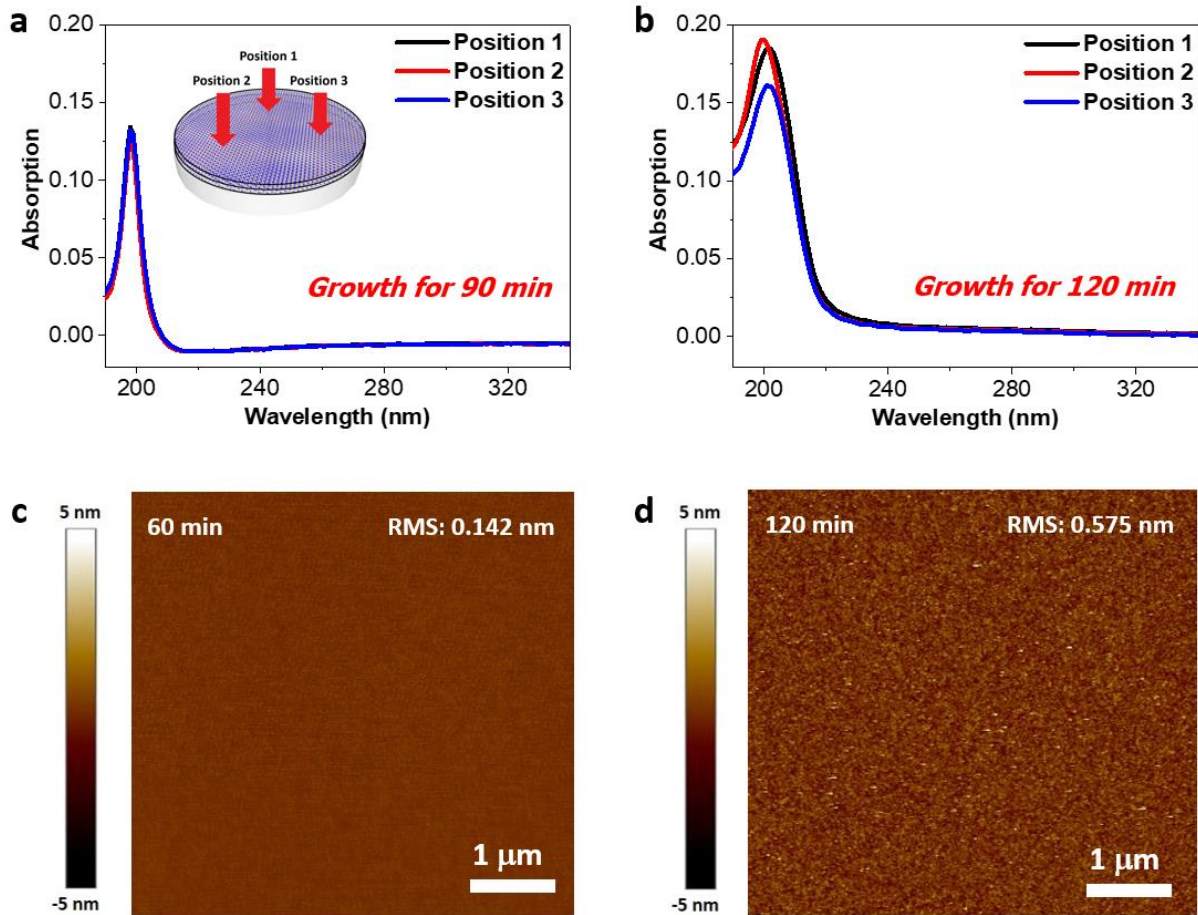


Figure 8. (a, b) UV absorption spectra of hBN/sapphire after growth for 90 and 120 min at 1220 °C, respectively. (c, d) Corresponding AFM images of (a) and (b).

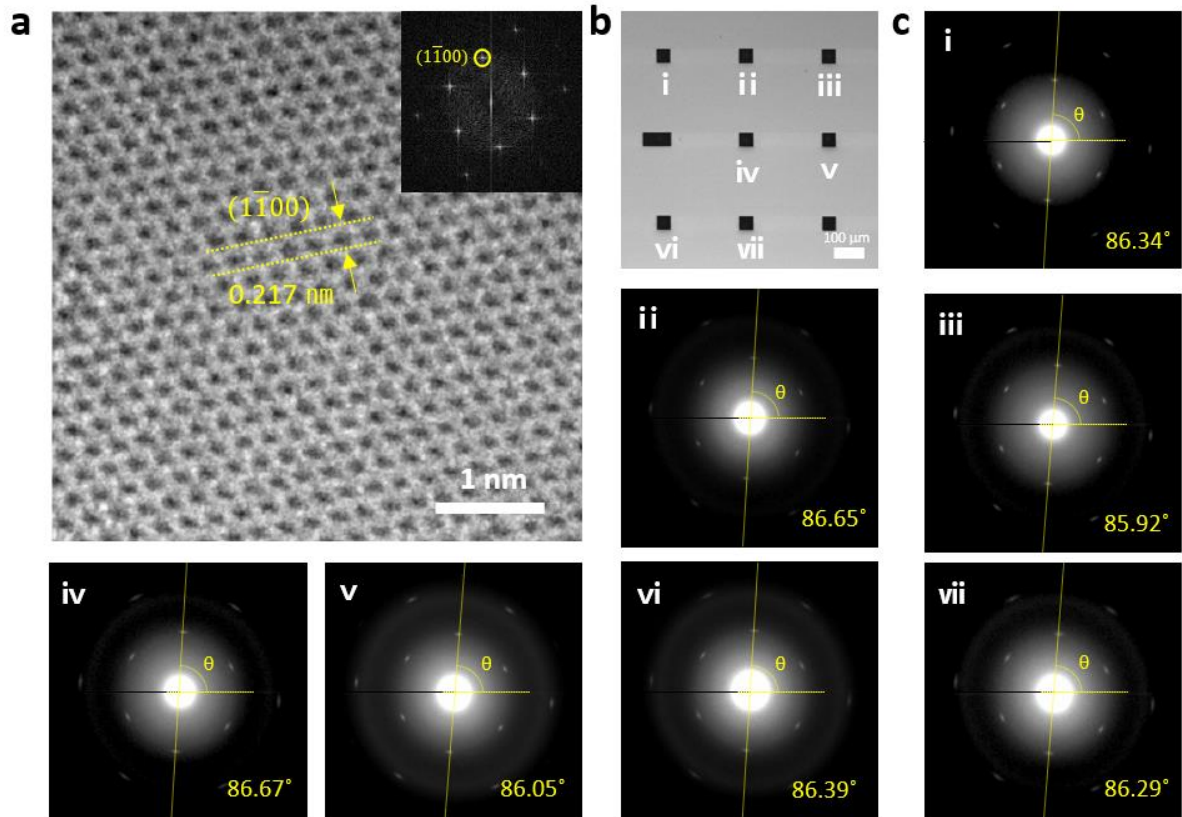


Figure 9. (a) High-resolution TEM image of trilayer hBN film on quantifoil TEM grid. The inset shows fast Fourier transform of the whole image. The d-spacing of $(1\bar{1}00)$ plane of hBN is 0.217 nm. (b) SEM image of trilayer hBN film transferred onto non-porous 5 nm-SiN thin film grid divided into nine regions. (c) SAED pattern images of seven segments from regions i to vii in (b). The relative rotation angle of hBN $(1\bar{1}00)$ plane to the horizontal direction is $86.33 \pm 0.27^\circ$ for region i to vii.

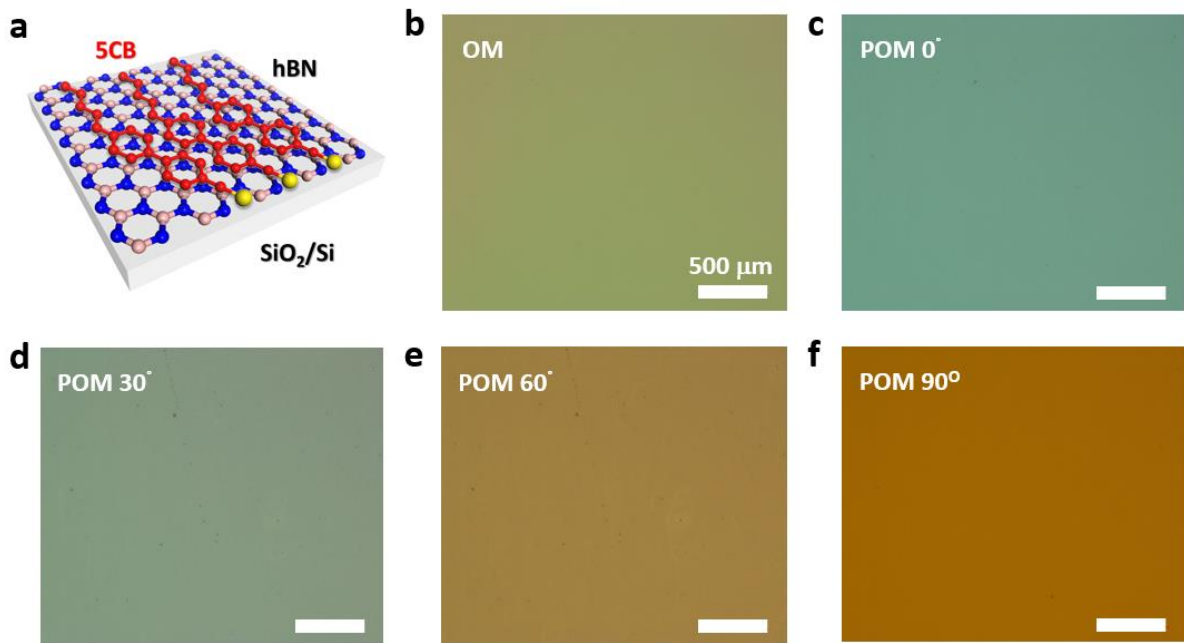


Figure 10. (a) Schematic illustration of liquid crystal (5CB) alignment on two types of hBN film transferred into SiO₂/Si. (b) Optical microscopic (OM) and (c-f) polarized optical microscopic (POM) images as a function of the polarized light angles: 0, 30, 60° of liquid crystal-coated trilayer hBN film.

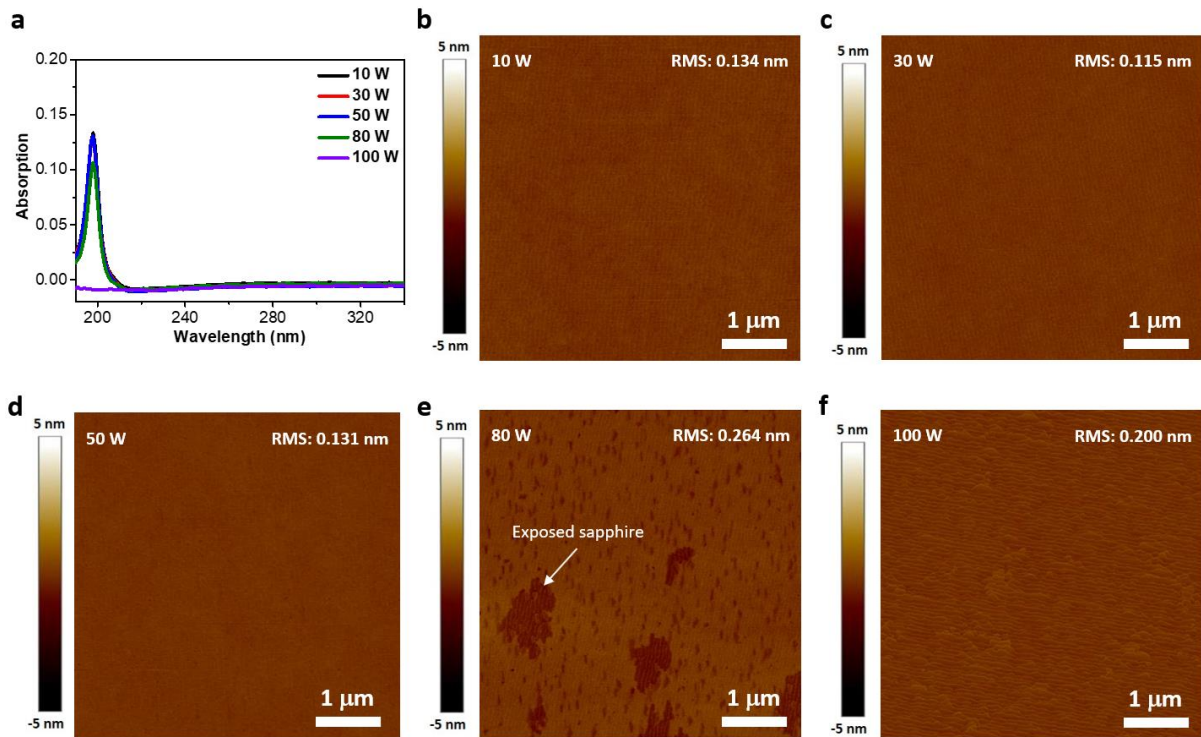


Figure 11. (a) UV absorption spectra of hBN/sapphire as a function of plasma power in the optimized growth condition for 30 min at 1220 °C. The corresponding AFM images of (b) 10, (c) 30, (d) 50, (e) 80, and (f) 100 W display the change of hBN surface with increasing plasma power.

3.4.2 Temperature-depended growth mechanism

We achieved the layer-controlled single-crystal hBN film by adjusting growth temperature. In previous **Section 3.4.1**, it was experimentally confirmed that the controlling the plasma power and growth time cannot increase the thickness of uniform hBN film. Therefore, we examined the effects of growth temperature with and without plasma-generated condition. When we fixed the borazine flow (0.1 sccm) and growth time (30 min) without plasma generation, the deposition thicknesses of hBN were varied by increasing growth temperatures from 1020 to 1220 °C (**Figure 12**). It denotes challenge of hBN growth on non-catalytic substrate near 1000 °C. While as grown hBN films without plasma generation show low crystallinity and large height distribution below 1220 °C, high-crystalline hBN film can be achieved at 1320 °C even if evolution of wrinkle (**Figure 13**). In addition, this high growth temperature leads to forming the crystalline AlN as a buffer layer, which is revealed by N 1s XPS spectrum and the line profile of electron energy loss spectra (EELS) at the surface region (**Figure 14a-c and 13c**). The cross-section scanning transmission electron microscopy (STEM) and FFT pattern along the $[1\bar{1}00]$ zone axis of sapphire display epitaxial growth of hBN (0002) on the AlN (0002) buffer layer (**Figure 14d and e**). The hBN and AlN planes are clearly distinguishable and allow an estimate of the *c*-axis lattice parameters for hBN and AlN which were measured to be ~ 3.4 and ~ 2.5 Å, respectively (**Figure 14f-h**). These interlayer spacing for hBN are corresponding to the previously reported values^{39, 40}. In addition, the gap (~ 1 Å) was formed between hBN and AlN layers, which can be generated buckling by wrinkle. We note that this wrinkled structure causes the distribution of rotation angles hBN film (**Figure 15**).

Figure 16 displays cross-sectional atomic-resolution TEM image of tri- and bilayer hBN films grown by plasma-assisted method at 1220 and 1120 °C, respectively. The lattice spacing values of two hBN films in the lateral direction show 0.13 nm, corresponding to lattice spacing in zigzag direction ($1\bar{1}00$) of hBN as shown in the inset of **Figure 16a**. That direction is parallel to sapphire ($11\bar{2}0$), thus indicating that the hBN film are rotated by 30° with respect to the sapphire substrate³⁵. Interestingly, the interlayer *d*-spacing of tri- and bilayer hBN film shows ~ 3.7 Å, which is larger than that of bulk hBN (3.3 Å) (bottom panels in **Figure 16a and b**). This large interlayer *d*-spacing is also presented by the grazing-incidence wide-angle X-ray diffraction (GI-WAXD) pattern, which provides information on the surface-sensitive crystal information (**Figure 17**). To elucidate this unprecedented phenomenon, it is especially worth noting that the distance of 3.0 Å between the hBN layer and sapphire. In the XPS spectra of mono-, bi-, and trilayer hBN samples, we observed Al-N chemical bonds, which are presented shoulder peak in N 1s and Al 2p spectra (**Figure 18**). The number of Al-N bonds is provided by the N-Al/N-B ratio of 0.58 (**Figure 18b**), which implies that ~ 37 % of the N atoms in monolayer hBN are

bonded to underlying Al atoms of the substrate (Table 1). Even though the generation of Al-N bonds were presented by XPS measurements, crystalline AlN structure was not observed in our TEM images. However, the shorter *d*-spacing between the first hBN layer and sapphire than that between second and third layers implies the Al-N bond formed at the interface (Figure 19). Owing to this covalent bonded N atoms, the interlayer *d*-spacing of bi- and trilayer hBN is relaxed towards the sapphire surface than bulk hBN composed of van der Waals force.

According to the wet etching chemistry, the Al-N bonds between hBN and sapphire can be broken by AlN etchant (diluted HF in H₂O)^{41,42}. We adopted conventional wet transfer method using PMMA (see Section 3.3.2) to transfer monolayer hBN from sapphire to SiO₂/Si substrate. After transfer, we confirmed both of monolayer hBN chemical state without any bonds to substrate and absence of Al-N bond on sapphire growth substrate by XPS characterizations (Figure 20). The interlayer distance of trilayer hBN was changed after the wet-etching transfer process. The TEM result reveals interlayer distance of ~3.45 Å, which closes to bulk hBN (Figure 21a). The GI-WAXD measurement also indicates reduced interlayer spacing to ~3.45 Å (Figure 21b) These imply that the structural stress from Al-N chemical bond can be released by wet-etching process by AlN etchant

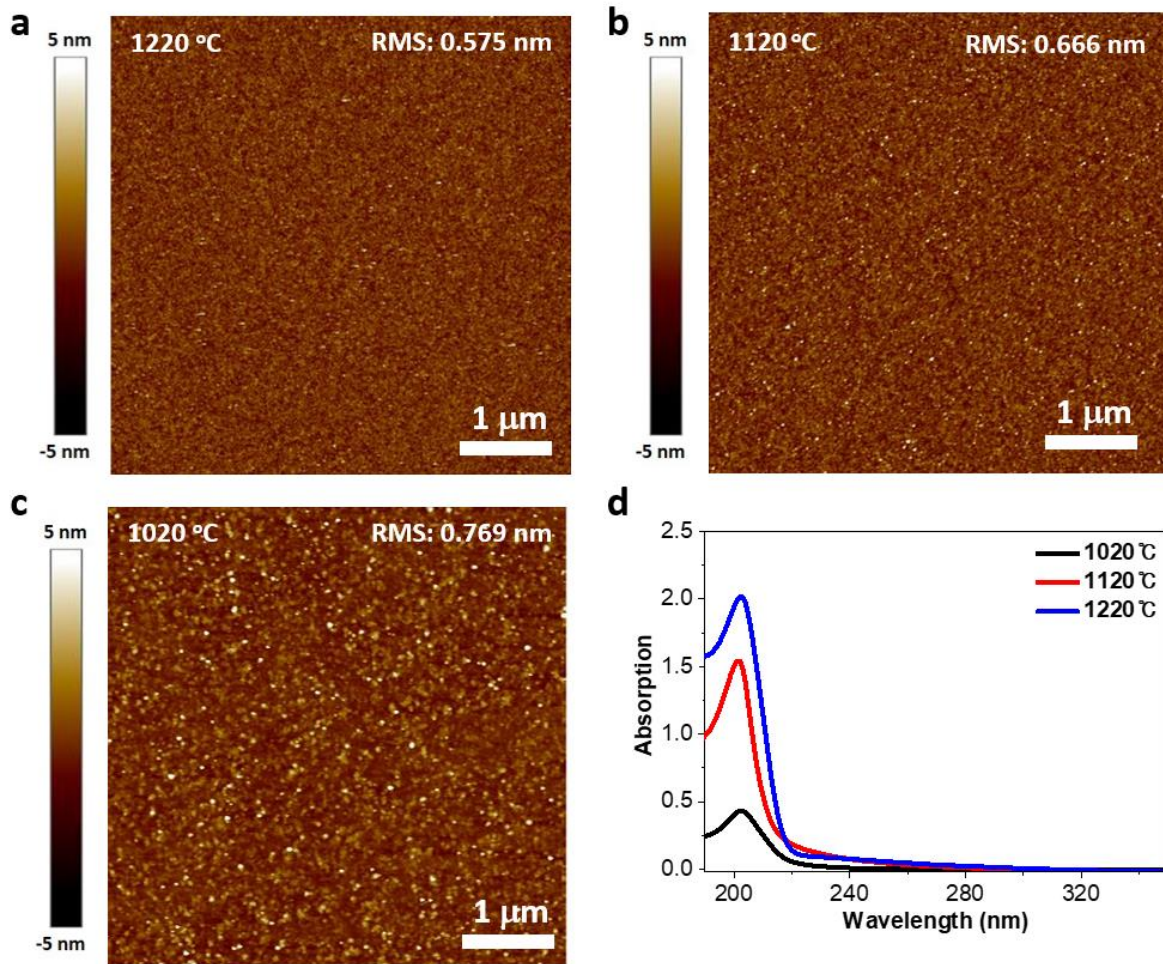


Figure 12. (a-c) AFM images of the surface on sapphire of hBN of sapphire at 1020, 1120, and 1220°C. (d) Corresponding UV absorption spectra.

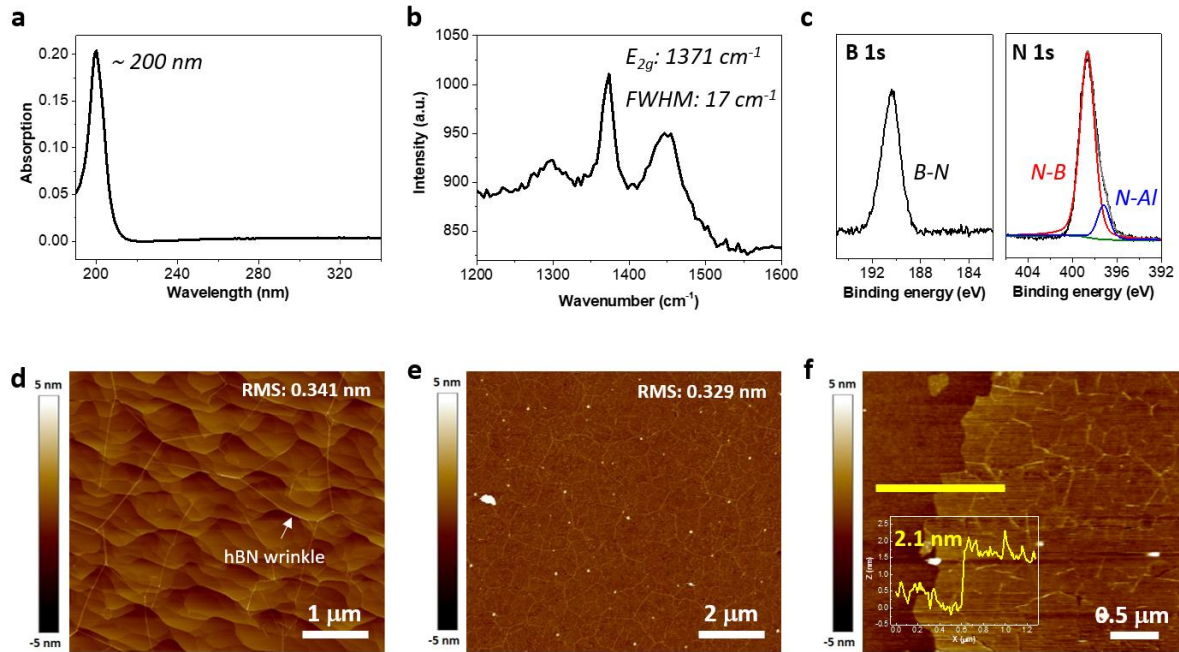


Figure 13. (a) UV absorption and (b) Raman spectra of multilayer hBN grown at 1320 °C without plasma generation. (c) Corresponding XPS spectra of multilayer hBN on sapphire. AFM images display surface of (d) before and (e and f) after transfer multilayer hBN film. Inset of (f) presents height profile of yellow line near the edge of multilayer hBN film.

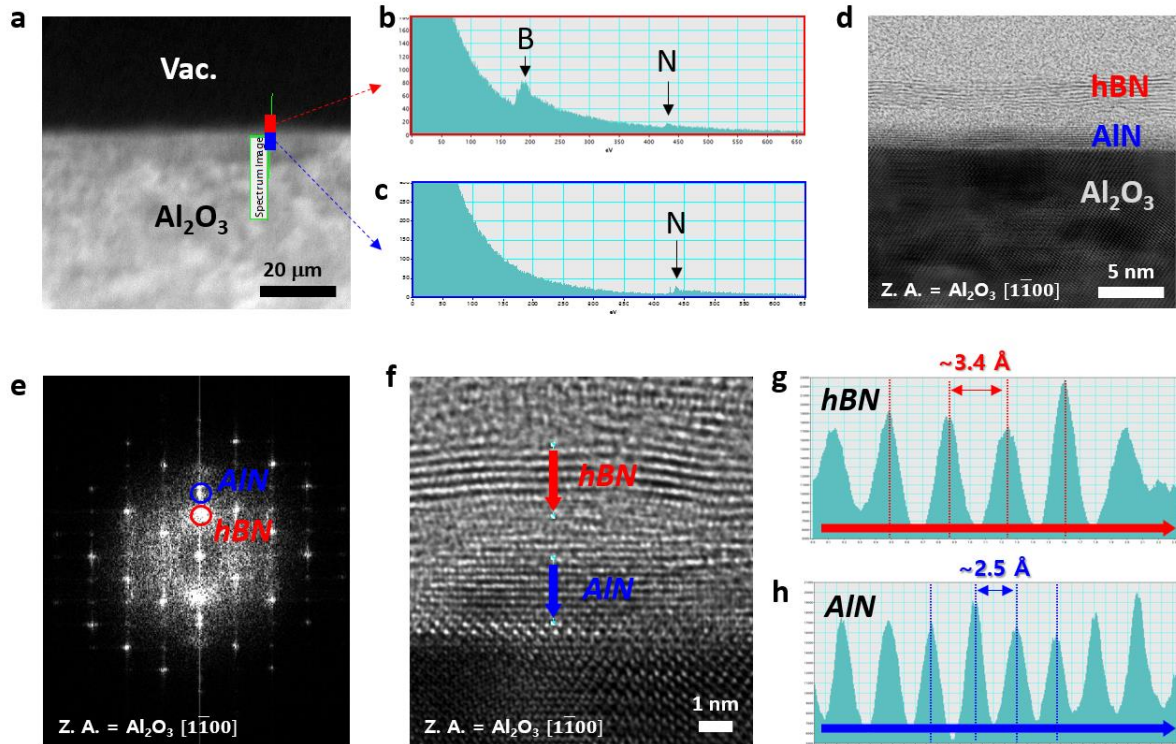


Figure 14. TEM analysis of multilayer hBN grown at 1320 °C without plasma generation. (a) low-magnified cross-section view for EELS line profile near the surface region of sapphire. (b and c) Corresponding EELS spectra of (a). (d) A STEM image of multilayer hBN/AlN buffer layer on sapphire. (e) A FFT pattern of multilayer hBN on AlN buffer layer, indicating epitaxial relationship. (f) Atomic-resolution TEM image of multilayer hBN and AlN buffer layer on sapphire. Intensity profile of the interlayer d -spacing of (g) hBN and (h) AlN along red and blue arrows in (f).

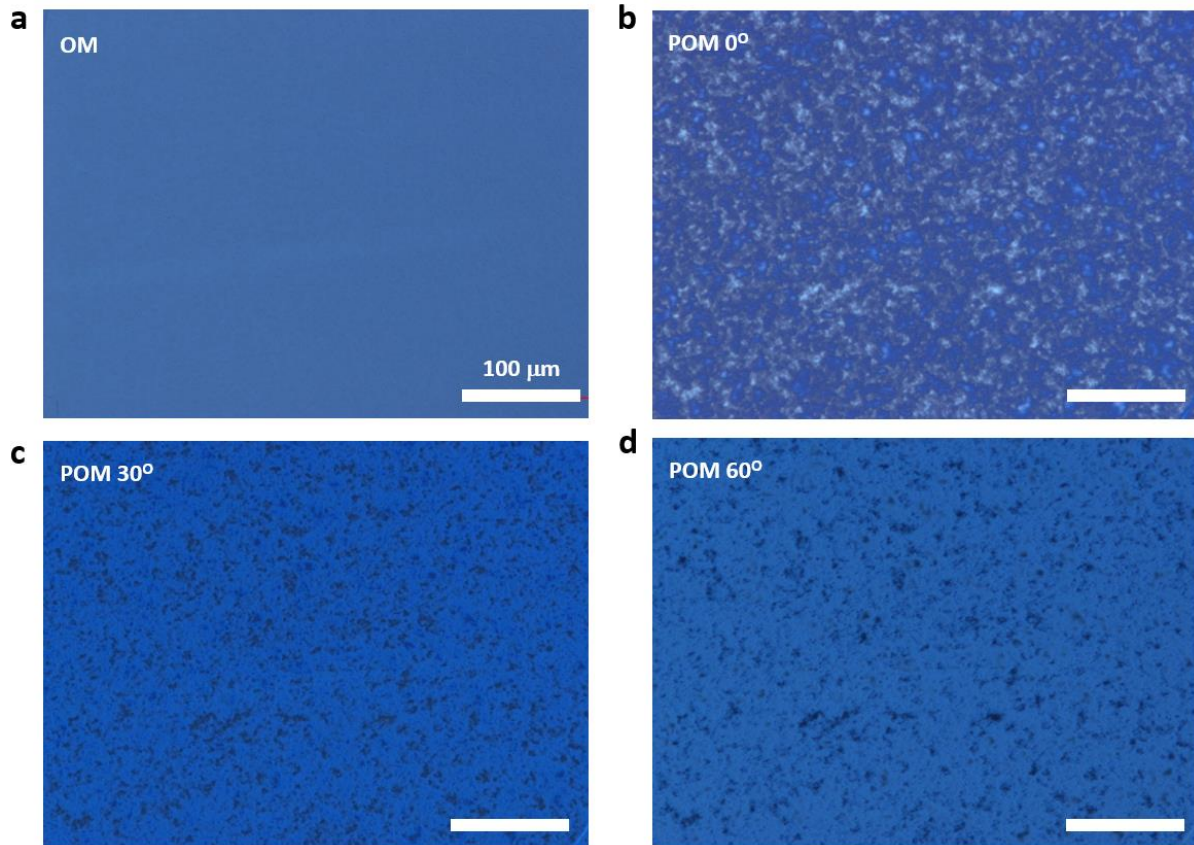


Figure 15. (a) Optical microscopic (OM) and (b-d) polarized optical microscopic (POM) images as a function of the polarized light angles: 0, 30, 60° of liquid crystal-coated multilayer hBN film grown at 1320 °C without plasma generation.

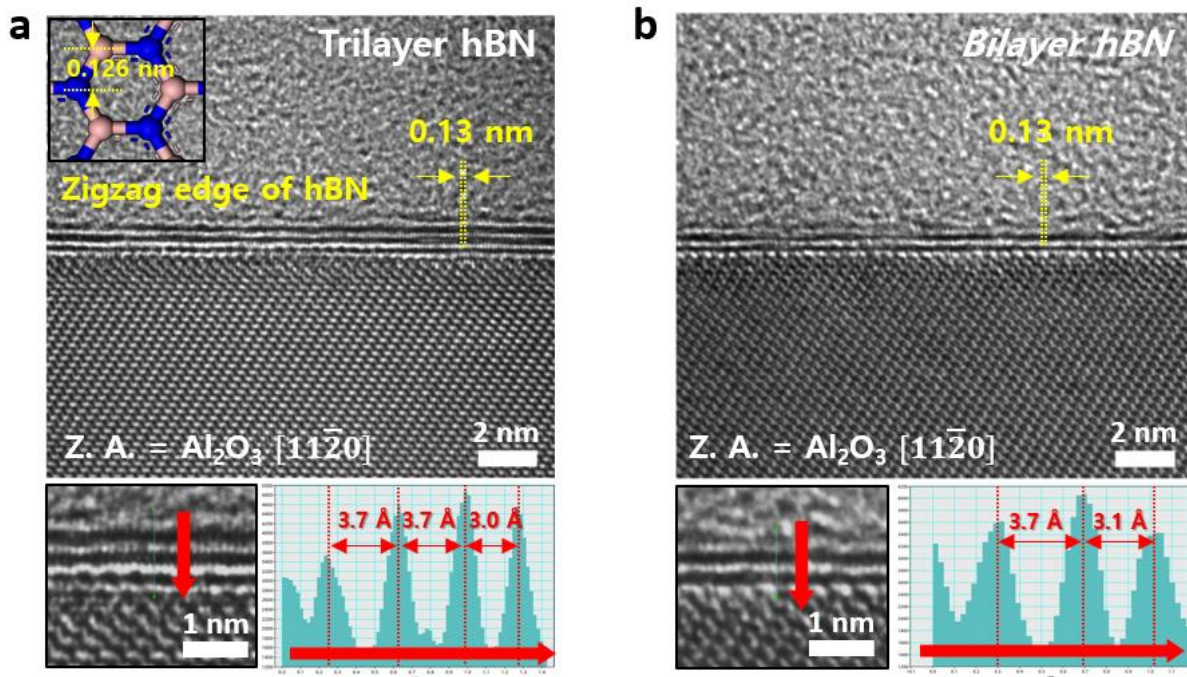


Figure 16. TEM analysis of tri- and bilayer hBN grown at 1220 and 1120 °C with plasma generation on sapphire, respectively. Atomic-resolution cross-sectional TEM images of (a) trilayer and (b) bilayer hBN display zigzag edge of hBN (inset of a) parallel to sapphire ($11\bar{2}0$). Left bottom panels in (a and b) show zoom-in images at the interface between hBN layers and sapphire. Right bottom panels in (a and b) are intensity profiles of red arrows in left bottom panels.

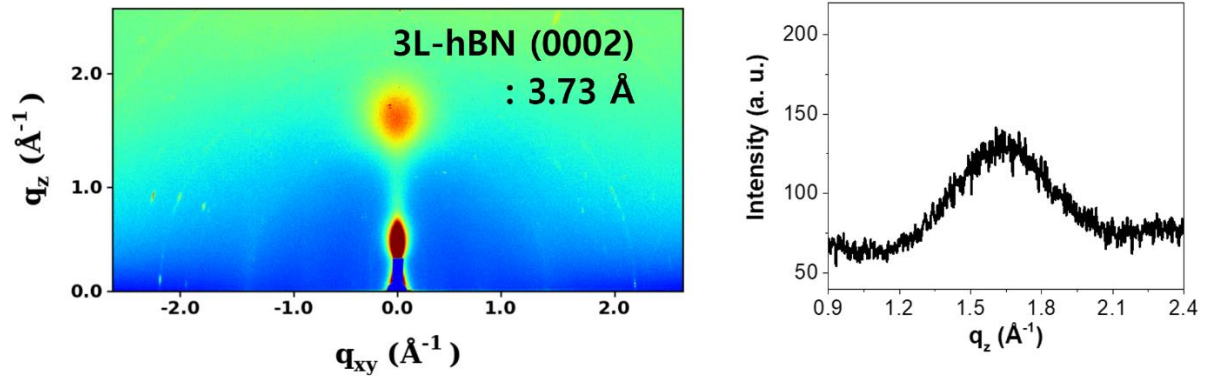


Figure 17. GI-WAXD result of trilayer hBN on sapphire substrate.

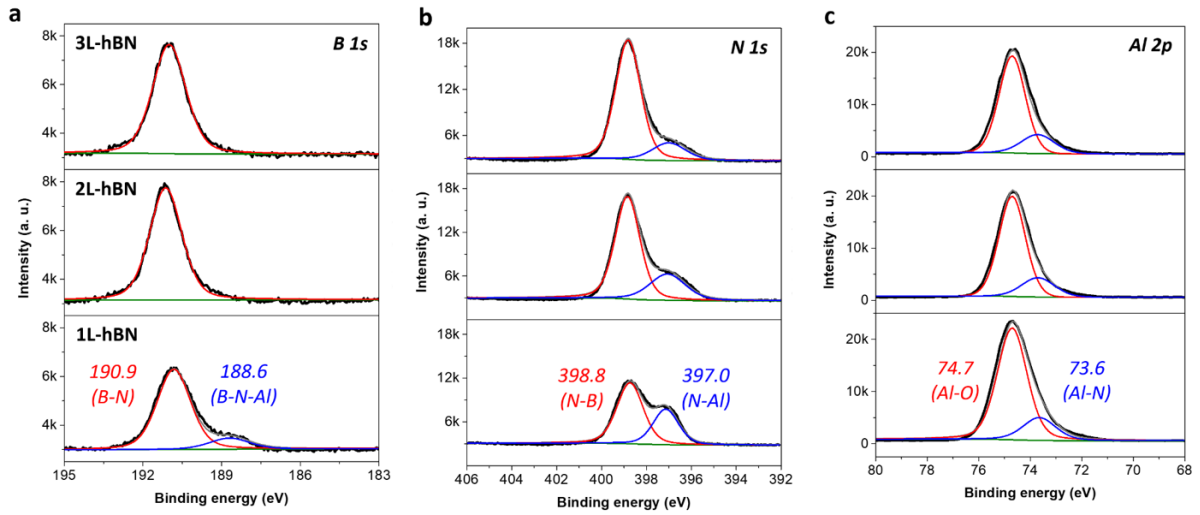


Figure 18. XPS spectra of (a) B 1s, (b) N 1s, and (c) Al 2p on tri-, bi-, and monolayer hBN, respectively. All samples are grown by plasma-assist CVD method.

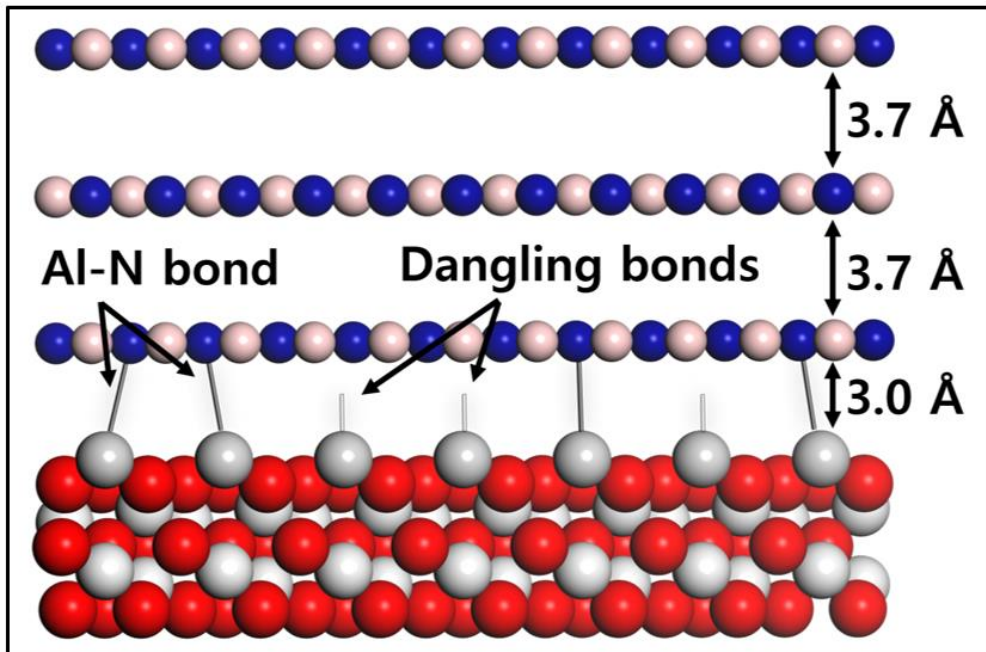


Figure 19. Schematic illustration of trilayer hBN on sapphire. Al-N bonds are formed between the bottom hBN and Al on the top of sapphire

Table 1 | Concentrations of Al-N bonding in mono-, bi-, and trilayer hBN films

N 1s of hBN	1L-hBN	2L-hBN	3L-hBN
Al-N areal ratio	36±3%	24±3%	16±3%
Estimated Al-N areal ratio	36±3%	18±1.5%	12±1%

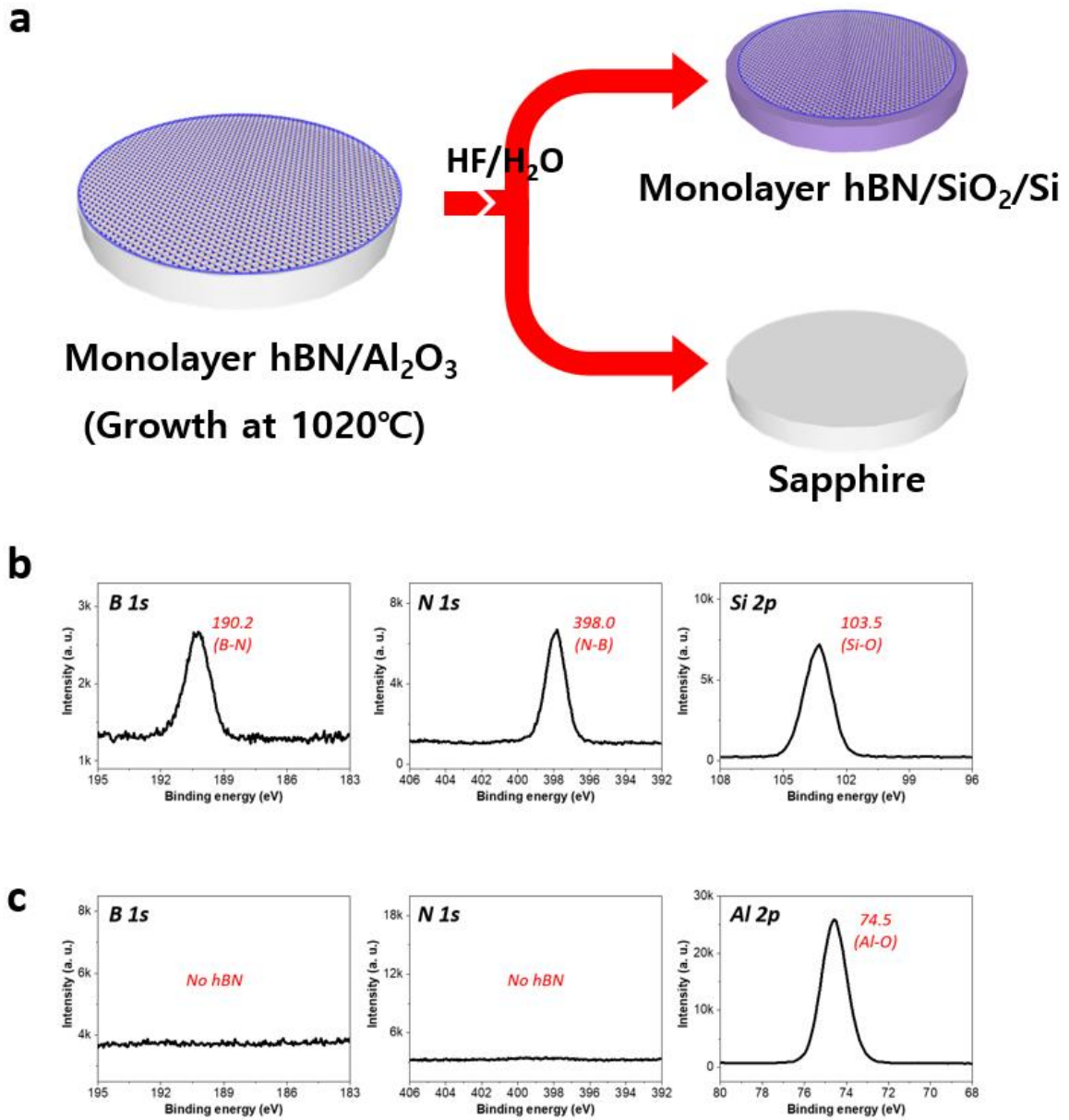


Figure 20. (a) Schematic illustration of separation of monolayer hBN from sapphire by wet-etching transfer method. (b) B 1s, N 1s, and Si 2p XPS spectra of as-transferred monolayer hBN on SiO₂/Si. (c) B 1s, N 1s, and Al 2p XPS spectra of sapphire after delamination of hBN.

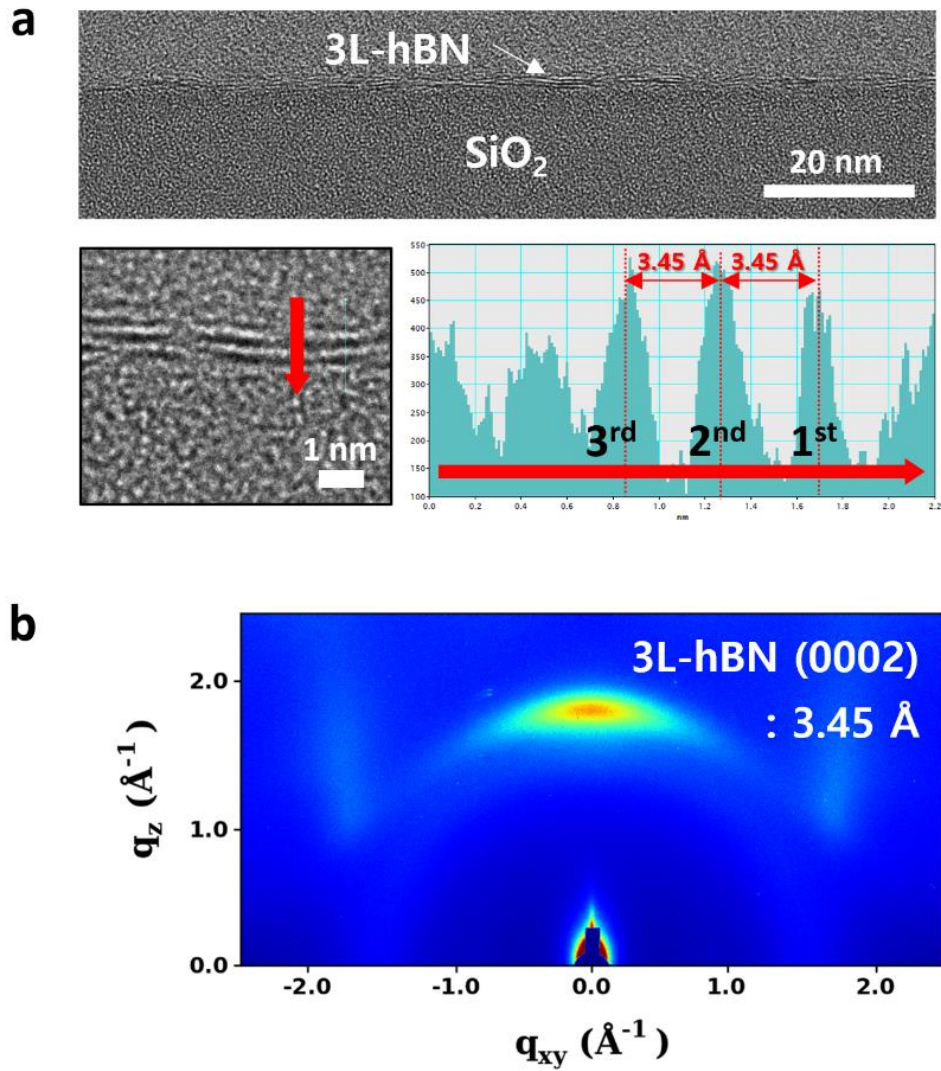


Figure 21. (a) TEM analysis of as-transferred trilayer hBN on SiO₂/Si. Left bottom panels in (a) show zoom-in images at the interface between hBN layers and SiO₂/Si. Right bottom panels in (a) are intensity profiles of red arrows in left bottom panels. (b) GI-WAXD result of trilayer hBN on SiO₂/Si substrate.

3.4.3 Membrane application for molecular transport

Ultrathin 2D film beyond graphene is the potential molecular barrier with desired pores⁴³. We performed water vapor transmission rate (WVTR) measurement for gas-diffusion barrier test (see **Section 3.3.4**). hBN films were transferred onto polyethylene terephthalate (PET) film. The WVTR of 1.2-nm hBN single crystal film and defective 2.1-nm hBN film (with wrinkles) were estimated to be 0.59 and 0.63 g/m²·day, respectively, which indicates improvement of 59% and 55% against bare PET film (1.44 g/m²·day) (**Figure 22**). The single-crystalline 1.2-nm-thick hBN film shows higher performance than the defective 2.1-nm-thick hBN film even it has lower thickness. This result directly shows importance of defect density of hBN film during molecular permeation.

We further estimated gas transport properties of 1.2-nm-thick single-crystalline hBN. A gas transport membrane utilizing a hBN film was fabricated by polymer casting method (**Figure 23a**, see **Section 3.3.3**). A large-scale hBN film on PES supports is presented in **Figure 23b**. While the vast majority of PES pores are covered with hBN film (dark contrast), the hBN film on local PES pore shows small tears from wet transfer process (yellow arrow in **Figure 23b**). The cross-sectional SEM image displays a 30- μ m-thickness hierarchical pore structure with \sim 500 nm pores located underneath hBN film (**Figure 23c**). These nano-scale pores connected to much larger pores approximately a few micron-scale further below. Such a hierarchical pore membrane leads to reduce the resistance and promote the diffusion-driven transport while simultaneously supporting hBN film. Single-component gas transport measurements from three separate membranes revealed H₂ permeance in the range of 8.8×10^3 - 1.8×10^4 GPU with H₂/N₂, H₂/CO₂, and H₂/C₃H₈ ideal selectivity ranging between 11.5-20.0, 11.5-22.5, and 6.6-10.0, respectively at room temperature (**Figure 24a-c**). The H₂ permeance and ideal selectivity of hBN/PES support membrane outperform recently reported graphene membrane, which revealed H₂ permeance in the range of 15-215 GPU and H₂/CO₂, H₂/CH₄, and He/H₂ ideal selectivity ranging between 3.1-7.2, 4.8-13.0, and 0.7-2.0, respectively (**Table 2**)⁴⁴. These results indicate that our trilayer hBN shows extremely low intrinsic defect density including atomic size nanopores, which is permeation channel in 2D membrane. The estimation of separating a gas mixture enables the contribution of competitive adsorption on the overall separation performance from the hBN membrane. To achieve this, we performed separation experiment using mixture gas environment. However, the separation factor in H₂/CO₂ gas mixture (\sim 5.5) was lower than ideal selectivity (\sim 22.5) with low H₂ permeation rate (4.6×10^3 versus 1.8×10^4 GPU) (**Figure 24d**). This result elucidates that the competitive adsorption between H₂ and CO₂ on the basal plane of hBN plays significant barrier effect in overall gas transport. Based on estimated H₂ permeance and ideal selectivity, it can be suggested that single-crystal hBN ensures a great potential for molecular sieving membrane.

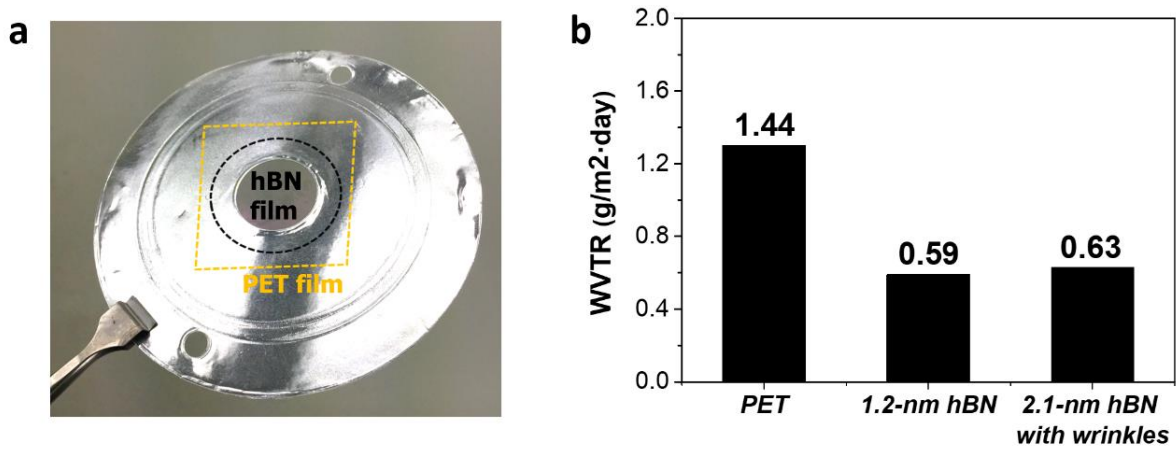


Figure 22. (a) A photograph for the WVTR measurement. (b) WVTR results of PET, 1.2-nm-thick single-crystalline hBN, and 2.1-nm-thick polycrystal hBN films.

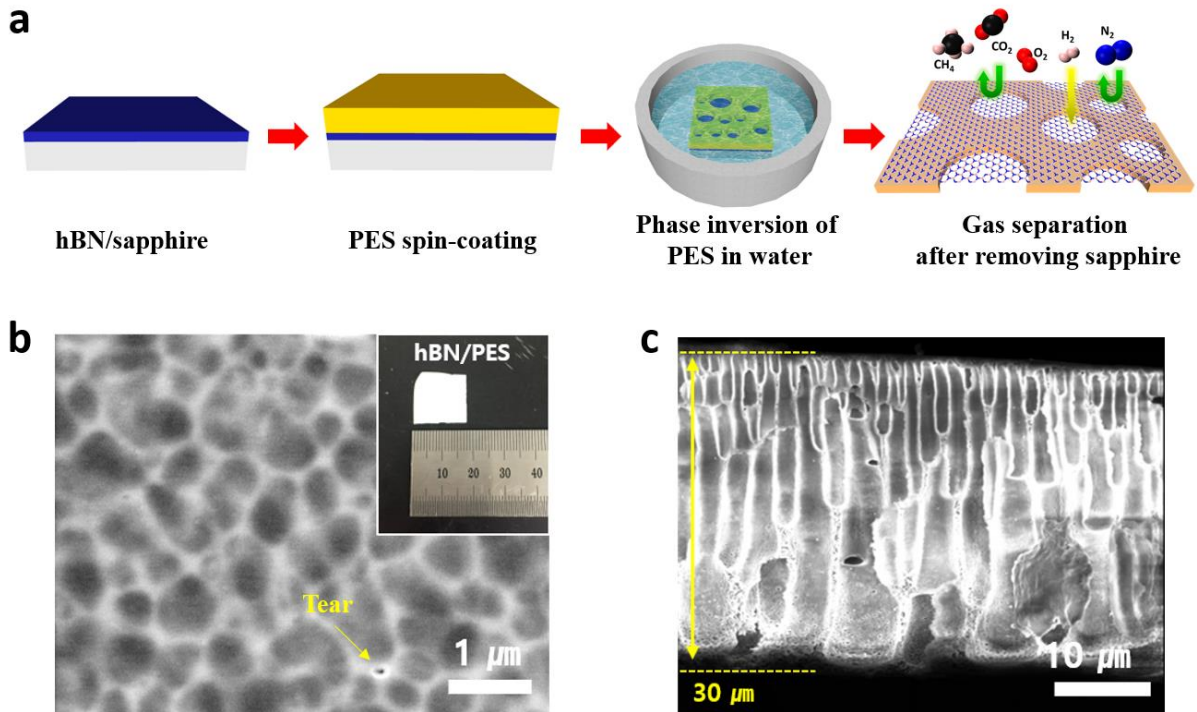


Figure 23. (a) Schematically drawn polymer casting method on hBN film grown on sapphire. (b) SEM image of hBN film on porous PES support. Inset of (a) is a photograph of as fabricated large-scale gas transport membrane. (c) Cross-section SEM image of PES support indicates a hierarchical pore structure with ~500 nm pores located underneath hBN film. The thickness of entire membrane is ~ 30 μm.

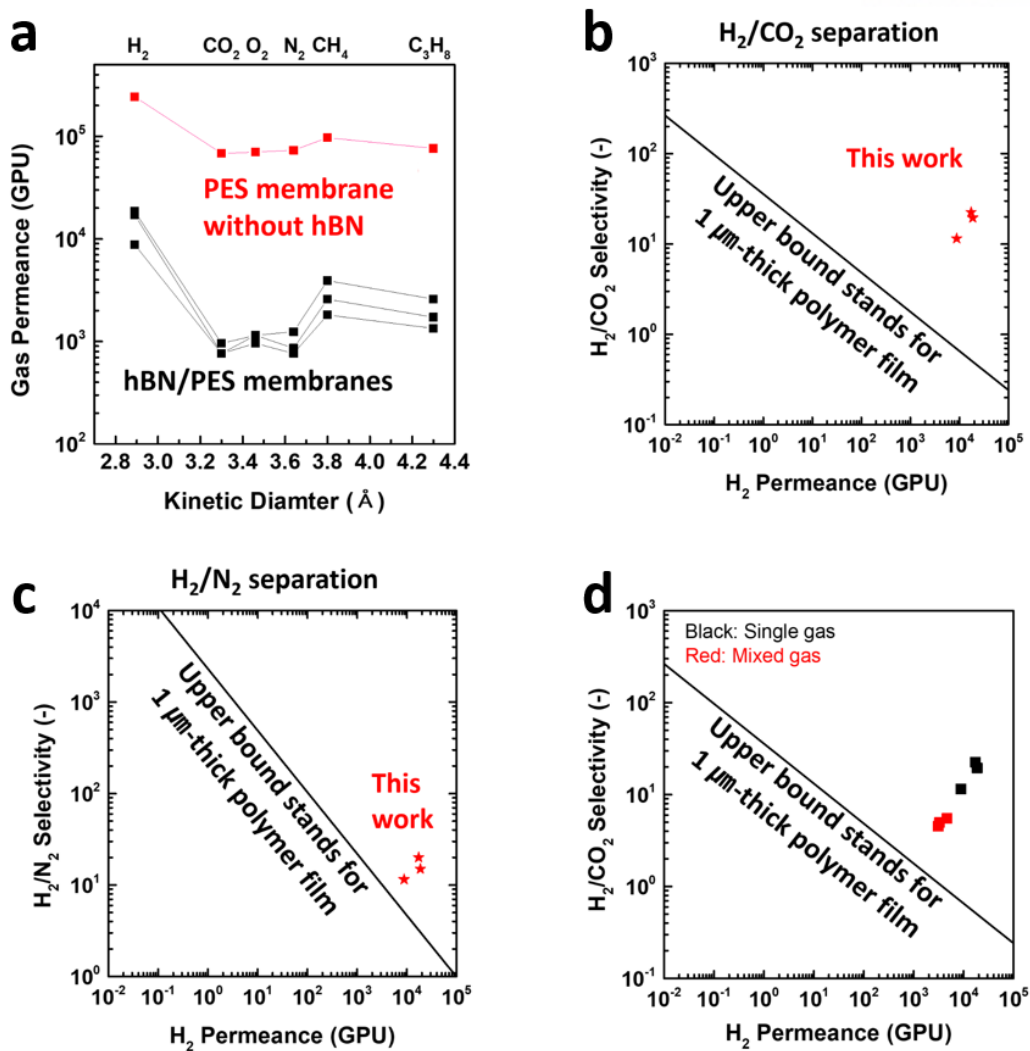


Figure 24. Gas permeation and separation performance through hBN/PES supporting membrane at room temperature. (a) Permeances of six molecules through a trilayer hBN film. (b and c) Ideal selectivity for H₂/CO₂ and H₂/N₂ gas pairs from three membranes. (d) The gas mixture (H₂/CO₂) separation performance of trilayer hBN film/PES support.

Table 2 | Ideal selectivity of trilayer hBN/PES support membrane compare to Knudsen selectivity and monolayer graphene.

Ideal selectivity at 25°C					
Membrane	H ₂ /N ₂	H ₂ /CO ₂	H ₂ /CH ₄	H ₂ /C ₃ H ₈	References
Knudsen	3.7	4.7	2.8	4.7	<i>Standard</i>
Graphene	-	7.4	13	-	<i>Nat. Commun.</i> 2018 , 9, 2632
Trilayer hBN	20.0	22.5	6.7	10.0	This work

3.5 Conclusion

In summary, uniform single-crystalline multilayer hBN films with a controlled number of layers were obtained on 2-inch-sapphire wafer by the temperature-depended growth method using remote ICP-CVD. The formation of buffer layer between hBN film and sapphire enabled epitaxial growth of bilayer and trilayer hBN film. The spectroscopic and microscopic measurements were presented single-crystalline nature and influences from buffer layer. In addition, we also found a route to separate the buffer layer as a monolayer hBN using AlN etchant. This method demonstrated a promising route for the growth of precisely controlled single-crystal hBN film in wafer scale.

3.6 References

1. Watanabe, K.; Taniguchi, T.; Kanda, H., Direct-bandgap properties and evidence for ultraviolet lasing of hexagonal boron nitride single crystal. *Nat. Mater.* **2004**, *3* (6), 404-409.
2. Elias, C.; Valvin, P.; Pelini, T.; Summerfield, A.; Mellor, C. J.; Cheng, T. S.; Eaves, L.; Foxon, C. T.; Beton, P. H.; Novikov, S. V.; Gil, B.; Cassabois, G., Direct band-gap crossover in epitaxial monolayer boron nitride. *Nat. Commun.* **2019**, *10*, 2639.
3. Cassabois, G.; Valvin, P.; Gil, B., Hexagonal boron nitride is an indirect bandgap semiconductor. *Nat. Photonics* **2016**, *10* (4), 262-266.
4. Lee, C.; Li, Q. Y.; Kalb, W.; Liu, X. Z.; Berger, H.; Carpick, R. W.; Hone, J., Frictional Characteristics of Atomically Thin Sheets. *Science* **2010**, *328* (5974), 76-80.
5. Li, L. H.; Cervenka, J.; Watanabe, K.; Taniguchi, T.; Chen, Y., Strong Oxidation Resistance of Atomically Thin Boron Nitride Nanosheets. *ACS Nano* **2014**, *8* (2), 1457-1462.
6. Dean, C. R.; Young, A. F.; Meric, I.; Lee, C.; Wang, L.; Sorgenfrei, S.; Watanabe, K.; Taniguchi, T.; Kim, P.; Shepard, K. L.; Hone, J., Boron nitride substrates for high-quality graphene electronics. *Nat. Nanotechnol.* **2010**, *5* (10), 722-726.
7. Mak, K. F.; He, K. L.; Shan, J.; Heinz, T. F., Control of valley polarization in monolayer MoS₂ by optical helicity. *Nat Nanotechnol* **2012**, *7* (8), 494-498.
8. Yang, W.; Chen, G. R.; Shi, Z. W.; Liu, C. C.; Zhang, L. C.; Xie, G. B.; Cheng, M.; Wang, D. M.; Yang, R.; Shi, D. X.; Watanabe, K.; Taniguchi, T.; Yao, Y. G.; Zhang, Y. B.; Zhang, G. Y., Epitaxial growth of single-domain graphene on hexagonal boron nitride. *Nat. Mater.* **2013**, *12* (9), 792-797.
9. Ahn, S.; Kim, G.; Nayak, P. K.; Yoon, S. I.; Lim, H.; Shin, H. J.; Shin, H. S., Prevention of Transition Metal Dichalcogenide Photodegradation by Encapsulation with h-BN Layers. *ACS Nano* **2016**, *10* (9), 8973-8979.
10. Liu, Z.; Gong, Y.; Zhou, W.; Ma, L.; Yu, J.; Idrobo, J. C.; Jung, J.; MacDonald, A. H.; Vajtai, R.; Lou, J.; Ajayan, P. M., Ultrathin high-temperature oxidation-resistant coatings of hexagonal boron nitride. *Nat. Commun.* **2013**, *4*, 2541.

11. Watanabe, K.; Taniguchi, T.; Niiyama, T.; Miya, K.; Taniguchi, M., Far-ultraviolet plane-emission handheld device based on hexagonal boron nitride. *Nat. Photonics* **2009**, *3* (10), 591-594.
12. Britnell, L.; Gorbachev, R. V.; Jalil, R.; Belle, B. D.; Schedin, F.; Mishchenko, A.; Georgiou, T.; Katsnelson, M. I.; Eaves, L.; Morozov, S. V.; Peres, N. M. R.; Leist, J.; Geim, A. K.; Novoselov, K. S.; Ponomarenko, L. A., Field-Effect Tunneling Transistor Based on Vertical Graphene Heterostructures. *Science* **2012**, *335* (6071), 947-950.
13. Britnell, L.; Gorbachev, R. V.; Geim, A. K.; Ponomarenko, L. A.; Mishchenko, A.; Greenaway, M. T.; Fromhold, T. M.; Novoselov, K. S.; Eaves, L., Resonant tunnelling and negative differential conductance in graphene transistors. *Nat. Commun.* **2013**, *4*, 1794.
14. Hu, S.; Lozada-Hidalgo, M.; Wang, F. C.; Mishchenko, A.; Schedin, F.; Nair, R. R.; Hill, E. W.; Boukhvalov, D. W.; Katsnelson, M. I.; Dryfe, R. A. W.; Grigorieva, I. V.; Wu, H. A.; Geim, A. K., Proton transport through one-atom-thick crystals. *Nature* **2014**, *516* (7530), 227-230.
15. Yoon, S. I.; Seo, D. J.; Kim, G.; Kim, M.; Jung, C. Y.; Yoon, Y. G.; Joo, S. H.; Kim, T. Y.; Shin, H. S., AA'-Stacked Trilayer Hexagonal Boron Nitride Membrane for Proton Exchange Membrane Fuel Cells. *ACS Nano* **2018**, *12* (11), 10764-10771.
16. Khan, M. H.; Liu, H. K.; Sun, X. D.; Yamauchi, Y.; Bando, Y.; Golberg, D.; Huang, Z., Few-atomic-layered hexagonal boron nitride: CVD growth, characterization, and applications. *Mater. Today* **2017**, *20* (10), 611-628.
17. Britnell, L.; Gorbachev, R. V.; Jalil, R.; Belle, B. D.; Schedin, F.; Katsnelson, M. I.; Eaves, L.; Morozov, S. V.; Mayorov, A. S.; Peres, N. M. R.; Neto, A. H. C.; Leist, J.; Geim, A. K.; Ponomarenko, L. A.; Novoselov, K. S., Electron Tunneling through Ultrathin Boron Nitride Crystalline Barriers. *Nano Lett.* **2012**, *12* (3), 1707-1710.
18. Song, L.; Ci, L. J.; Lu, H.; Sorokin, P. B.; Jin, C. H.; Ni, J.; Kvashnin, A. G.; Kvashnin, D. G.; Lou, J.; Yakobson, B. I.; Ajayan, P. M., Large Scale Growth and Characterization of Atomic Hexagonal Boron Nitride Layers. *Nano Lett.* **2010**, *10* (8), 3209-3215.
19. Kim, S. M.; Hsu, A.; Park, M. H.; Chae, S. H.; Yun, S. J.; Lee, J. S.; Cho, D. H.; Fang, W. J.; Lee, C.; Palacios, T.; Dresselhaus, M.; Kim, K. K.; Lee, Y. H.; Kong, J., Synthesis of large-area multilayer hexagonal boron nitride for high material performance. *Nat. Commun.*

2015, 6, 8662.

20. Li, C.; Bando, Y.; Zhi, C. Y.; Huang, Y.; Golberg, D., Thickness-dependent bending modulus of hexagonal boron nitride nanosheets. *Nanotechnology* **2009**, *20* (38).
21. Lin, W. H.; Brar, V. W.; Jariwala, D.; Sherrott, M. C.; Tseng, W. S.; Wu, C. I.; Yeh, N. C.; Atwater, H. A., Atomic-Scale Structural and Chemical Characterization of Hexagonal Boron Nitride Layers Synthesized at the Wafer-Scale with Monolayer Thickness Control. *Chem. Mater.* **2017**, *29* (11), 4700-4707.
22. Koepke, J. C.; Wood, J. D.; Chen, Y. F.; Schmucker, S. W.; Liu, X. M.; Chang, N. N.; Nienhaus, L.; Do, J. W.; Carrion, E. A.; Hewaparakrama, J.; Ranaarajan, A.; Datye, I.; Mehta, R.; Haasch, R. T.; Gruebele, M.; Girolami, G. S.; Pop, E.; Lyding, J. W., Role of Pressure in the Growth of Hexagonal Boron Nitride Thin Films from Ammonia-Borane. *Chem. Mater.* **2016**, *28* (12), 4169-4179.
23. Kim, K. K.; Hsu, A.; Jia, X. T.; Kim, S. M.; Shi, Y. M.; Dresselhaus, M.; Palacios, T.; Kong, J., Synthesis and Characterization of Hexagonal Boron Nitride Film as a Dielectric Layer for Graphene Devices. *Acs Nano* **2012**, *6* (10), 8583-8590.
24. Tay, R. Y.; Wang, X. L.; Tsang, S. H.; Loh, G. C.; Singh, R. S.; Li, H.; Mallick, G.; Teo, E. H. T., A systematic study of the atmospheric pressure growth of large-area hexagonal crystalline boron nitride film. *J. Mater. Chem. C* **2014**, *2* (9), 1650-1657.
25. Zhang, D. J.; Wu, F. H.; Ying, Q.; Gao, X. Y.; Li, N.; Wang, K. J.; Yin, Z. Y.; Cheng, Y. H.; Meng, G. D., Thickness-tunable growth of ultra-large, continuous and high-dielectric h-BN thin films. *J. Mater. Chem. C* **2019**, *7* (7), 1871-1879.
26. Zhang, C. H.; Fu, L.; Zhao, S. L.; Zhou, Y.; Peng, H. L.; Liu, Z. F., Controllable Co-segregation Synthesis of Wafer-Scale Hexagonal Boron Nitride Thin Films. *Adv. Mater.* **2014**, *26* (11), 1776-1781.
27. Ismach, A.; Chou, H.; Ferrer, D. A.; Wu, Y. P.; McDonnell, S.; Floresca, H. C.; Covacevich, A.; Pope, C.; Piner, R.; Kim, M. J.; Wallace, R. M.; Colombo, L.; Ruoff, R. S., Toward the Controlled Synthesis of Hexagonal Boron Nitride Films. *ACS Nano* **2012**, *6* (7), 6378-6385.
28. Song, Y. X.; Zhang, C. R.; Li, B.; Jiang, D.; Ding, G. Q.; Wang, H. M.; Xie, X. M., Triggering the atomic layers control of hexagonal boron nitride films. *Appl. Surf. Sci.* **2014**, *313*, 647-

653.

29. Gao, Y.; Ren, W. C.; Ma, T.; Liu, Z. B.; Zhang, Y.; Liu, W. B.; Ma, L. P.; Ma, X. L.; Cheng, H. M., Repeated and Controlled Growth of Monolayer, Bilayer and Few-Layer Hexagonal Boron Nitride on Pt Foils. *ACS Nano* **2013**, *7* (6), 5199-5206.
30. Caneva, S.; Weatherup, R. S.; Bayer, B. C.; Blume, R.; Cabrero-Vilatela, A.; Braeuninger-Weirner, P.; Martin, M. B.; Wang, R. Z.; Baetz, C.; Schloegl, R.; Meyer, J. C.; Hofmann, S., Controlling Catalyst Bulk Reservoir Effects for Monolayer Hexagonal Boron Nitride CVD. *Nano Lett.* **2016**, *16* (2), 1250-1261.
31. Chugh, D.; Wong-Leung, J.; Li, L.; Lysevych, M.; Tan, H. H.; Jagadish, C., Flow modulation epitaxy of hexagonal boron nitride. *2D Mater.* **2018**, *5* (4), 045018.
32. Kim, D. Y.; Han, N.; Jeong, H. Y.; Kim, J. W.; Hwang, S. Y.; Song, K.; Choi, S. Y.; Kim, J. K., Pressure-Dependent Growth of Wafer-Scale Few-layer h-BN by Metal Organic Chemical Vapor Deposition. *Cryst. Growth Des.* **2017**, *17* (5), 2569-2575.
33. Li, Q. C.; Wu, Q. Q.; Gao, J.; Wei, T. B.; Sun, J. Y.; Hong, H.; Dou, Z. P.; Zhang, Z. P.; Rummeli, M. H.; Gao, P.; Yan, J. C.; Wang, J. X.; Li, J. M.; Zhang, Y. F.; Liu, Z. F., Direct Growth of 5 in. Uniform Hexagonal Boron Nitride on Glass for High-Performance Deep-Ultraviolet Light-Emitting Diodes. *Adv. Mater. Interfaces* **2018**, *5* (18), 1800662.
34. Kidambi, P. R.; Nguyen, G. D.; Zhang, S.; Chen, Q.; Kong, D.; Warner, J.; Li, A. P.; Karnik, R., Facile Fabrication of Large-Area Atomically Thin Membranes by Direct Synthesis of Graphene with Nanoscale Porosity. *Adv. Mater.* **2018**, *30* (49), 1804977.
35. Jang, A. R.; Hong, S.; Hyun, C.; Yoon, S. I.; Kim, G.; Jeong, H. Y.; Shin, T. J.; Park, S. O.; Wong, K.; Kwak, S. K.; Park, N.; Yu, K.; Choi, E.; Mishchenko, A.; Withers, F.; Novoselov, K. S.; Lim, H.; Shin, H. S., Wafer-Scale and Wrinkle-Free Epitaxial Growth of Single-Orientated Multilayer Hexagonal Boron Nitride on Sapphire. *Nano Lett.* **2016**, *16* (5), 3360-3366.
36. Uchida, Y.; Nakandakari, S.; Kawahara, K.; Yamasaki, S.; Mitsuhashi, M.; Ago, H., Controlled Growth of Large-Area Uniform Multilayer Hexagonal Boron Nitride as an Effective 2D Substrate. *ACS Nano* **2018**, *12* (6), 6236-6244.
37. Lee, J. S.; Choi, S. H.; Yun, S. J.; Kim, Y. I.; Boandoh, S.; Park, J. H.; Shin, B. G.;

Ko, H.; Lee, S. H.; Kim, Y. M.; Lee, Y. H.; Kim, K. K.; Kim, S. M., Wafer-scale single-crystal hexagonal boron nitride film via self-collimated grain formation. *Science* **2018**, *362* (6416), 817-821.

38. Park, J. H.; Park, J. C.; Yun, S. J.; Kim, H.; Luong, D. H.; Kim, S. M.; Choi, S. H.; Yang, W.; Kong, J.; Kim, K. K.; Lee, Y. H., Large-Area Monolayer Hexagonal Boron Nitride on Pt Foil. *ACS Nano* **2014**, *8* (8), 8520-8528.

39. Chubarov, M.; Pedersen, H.; Hogberg, H.; Darakchieva, V.; Jensen, J.; Persson, P. O. A.; Henry, A., Epitaxial CVD growth of sp²-hybridized boron nitride using aluminum nitride as buffer layer. *Phys. Status Solidi RRL* **2011**, *5*, 397-399.

40. Page, R.; Casamento, J.; Cho, Y. J.; Rouvimov, S.; Xing, H. G.; Jena, D., Rotationally aligned hexagonal boron nitride on sapphire by high-temperature molecular beam epitaxy. *Phys. Rev. Mater.* **2019**, *3* (6), 064001.

41. Barrett, N. J.; Grange, J. D.; Sealy, B. J.; Stephens, K. G., Annealing of Zinc-Implanted Gaas. *J. Appl. Phys.* **1985**, *57* (12), 5470-5476.

42. Taylor, K. M.; Lenie, C., Some Properties of Aluminum Nitride. *J. Electrochem Soc.* **1959**, *106* (3), C67-C67.

43. Vlassioug, I. V., WATER TREATMENT A scalable graphene-based membrane. *Nat. Nanotechnol.* **2017**, *12* (11), 1022-1023.

44. Huang, S. Q.; Dakhchoune, M.; Luo, W.; Oveisi, E.; He, G. W.; Rezaei, M.; Zhao, J.; Alexander, D. T. L.; Zuttel, A.; Strano, M. S.; Agrawal, K. V., Single-layer graphene membranes by crack-free transfer for gas mixture separation. *Nat. Commun.* **2018**, *9*, 2632.